Roles of Grain Boundaries in Cleavage Cracking and Thermal Crack Arrest Experiments in Iron-Silicon Alloy

by
Yu Qiao

B.S., Applied Mechanics, University of Science and Technology of China, 1994
M.S., Materials Science, Chinese Academy of Sciences, 1997

submitted to the Department of Mechanical Engineering
in partial fulfillment of the requirements for the degree of

Doctor of Philosophy in Mechanical Engineering

at the

MASSACHUSETTS INSTITUTE OF TECHNOLOGY

September 2002

Author.....
August 14, 2002

Certified by.....
Ali S. Argon
Professor of Mechanical Engineering
Thesis Supervisor

Accepted by.....
Ain A. Sonin
Professor of Mechanical Engineering
Chairman, Departmental Committee on Graduate Students

Roles of Grain Boundaries in Cleavage Cracking and Thermal Crack Arrest Experiments in Iron-Silicon Alloy

by
Yu Qiao

Submitted to the Department of Mechanical Engineering
on August 14, 2002 in Partial Fulfillment of the
Requirements for the Degree of Doctor of Philosophy in Materials Science

ABSTRACT

High-angle grain boundaries in steel offer an important resistance to the propagation of cleavage cracks that affects the fracture toughness and can modulate the ductile-to-brittle transition temperature of fracture downward. This behavior has been studied in this thesis in detail.

In grain-boundary toughness measurement experiments in bicrystals of Fe-3%Si alloy, specific measurements of the fracture resistance of a random selection of high angle grain boundaries and associated fractographic studies have led to quantitative models of the resistance that high-angle grain boundaries offer to cleavage cracks. The study has also revealed a transition from pure cleavage to mixed cleavage (PC/MC) around 0C for this alloy.

Experiments were also carried out on the modes of advance of cleavage cracks through a field of randomly oriented grains at -30C in the pure cleavage range (lower shelf) in very large grain-sized Fe-2%Si alloy, permitting detailed observations of the chronology of percolation of the cleavage crack front. Utilizing previously developed model-based information on the peak resistance to fracture of high angle grain boundaries, with a given tilt and twist misorientation across them, and detailed measurements of orientations of individual grains in the samples, it was possible to develop percolation maps of cleavage through the field of grains that for the initial phases of fracture through grains predicted the actual path with about 70% accuracy when compared with experimental observations. On the basis of these experiments and modeling a simple expression is projected for the effect of grain boundaries on the overall cleavage fracture resistance of low-carbon steel in the lower shelf region.

In addition to the study of behavior of grain boundaries, thermal crack arrest experiments were performed in single crystals of Fe-3%Si alloy. The brittle-to-ductile transition temperatures at various loading rates were measured, and dislocation activities associated with the brittle-to-ductile transition were discussed.

Thesis Supervisor: Ali S. Argon
Title: Professor of Mechanical Engineering

ACKNOWLEDGEMENTS

I would like to express my sincerest thanks to Professor Ali S. Argon for helping to supervise me, providing resources and subjects, offering direction and penetrating criticism. Without his aid and guidance throughout the course of this research my understanding of this program would have been superficial at best.

Grateful appreciation is acknowledged to my committee members, Professor F. A. McClintock, Professor D. M. Parks, and Professor S. M. Spearing, whose helpful advice greatly facilitated many aspects of this work.

Special thanks are extended to my wife, Hua, for her encouragement and unwavering support.

TABLE OF CONTENTS

TABLE OF SYMBOLS

α : the angle between the grain boundary line on the fracture plane and the z-axis; the ratio of the average grain diameter to the grain edge length in Eqn.7-12

α_{ij} : direction cosines

β : the angle between vector **d** and [100] direction shown in Fig.2-2; material constant describing relationship between δ_B and Δx in Chapter 6; material constant in Eqn.7-12

β_c : the universal constant for process zone theory

Γ : the constant of DCB specimen

Δ_c : process zone size

ΔA : the increment of cleavage surface in grain B

Δh : height difference of cleavage surfaces across a grain boundary

ΔK_{ICGB} : difference between K_{ICGB} and K_{ICA}

ΔG^* : activation energy

ΔU : the fracture work required to overcome boundary resistance

ΔW_p : the increment of work of separation of the grain boundary islands

Δx : penetration depth of the crack front across the grain boundary

Δx_c : the critical penetration depth of the crack front across the grain boundary

δ : crack opening displacement

δ_B : shearing distance along the grain boundary

δ_c : critical crack opening displacement

θ : angle between reflecting plane and incident x-ray beam

$\tilde{\theta}$: angle to crack propagation direction

τ_{nm} : resolved shear stress on slip system **n**/**m**

λ : wavelength of incident x-ray beam

μ : the parameter of log-normal distribution function

μ_i : complex roots of Eqn.4-10

ν : Poisson's ratio

ξ : the material constant defined by Eqn.7-9

$\tilde{\rho}$: analogue of $\tilde{r}$ in slip plane

σ : the parameter of log-normal distribution function

σ_B : the average cohesive strength in the process zone

σ_{ij} : stress tensor

σ_y : yield strength

φ : twist misorientation between cleavage surfaces in grain B and grain A

$\tilde{\varphi}$: analogue of $\tilde{\theta}$ in slip plane

φ_0 : twist angle of an individual grain

φ_0^j : twist angle of the j^{th} grain

ψ : tilt misorientation between cleavage surfaces in grain B and grain A

$\tilde{\psi}$: angle between plain strain plane and slip plane

ψ_0 : tilt angle of an individual grain

ψ_0^j : tilt angle of the j^{th} grain

$\tilde{A}$: a constant of the DCB specimen defined by Eqn.4-2

a: crack length; lattice parameter in Eqn.4-4

$a(z)$: local crack length along z-axis

a_1: initial crack length

a_2: the total crack length abutting on the grain boundary

B: material constant defined by Eqn.7-8

b: thickness of specimen

b_n: thickness of the specimen across the roots of side grooves

C: material constant defined by Eqn.6-8

C_m: compliance of the loading machine

C_{lc}: compliance of the load cell

C_s, $\tilde{C}_s$: compliance of specimen; constant of grain shape in Chapter 7

c: velocity of a shear wave

c_{ij}: stiffness constants

D: grain size

$\tilde{D}$: constant of DCB specimen

d: distance between reflecting plane

E: Yong's modulus of the specimen

f_{ij}: function of $\tilde{\theta}$

G_0: critical stress intensity factor in a single crystal

G_{IC}: critical energy release rate of single crystal

$\overline{G}_{IC}$: required energy release rate for ductile crack extension above BDT

$G_{IC}(z)$: local critical energy release rate along z-axis

G_{ICA}: critical energy release rate of grain A

G_{ICB}: critical energy release rate of grain B

G_{ICPC}: critical energy release rate of polycrystalline material

G_{ICSC}: critical energy release rate of single crystal

g_{nm}: normalized resolved shear stress of slip system **n**/**m**

h: height of the arm of double cantilever beam specimen

(h, k, l): indices of reflecting plane

J_C: critical J-integral

$K(z)$: local stress intensity along z-axis
K_0: local stress intensity factor with a virtual straight crack front
K_{appl}: applied stress intensity factor
K_I: mode-I stress intensity factor
K_{I3}: critical stress intensity factor to break through the grain boundary
K_{IC}: critical stress intensity factor
K_{ICA}: critical stress intensity factor of grain A
K_{ICGB}: critical stress intensity factor at bicrystal grain boundary
K_{ICa}: critical stress intensity factor for a crack jump
K_{ICb}: critical stress intensity factor for crack stop
$K_{IC}^{(i)}$: critical stress intensity factor of the i^{th} grain boundary
K_{ICPC}: critical stress intensity factor of polycrystalline material
K_{ICSC}: critical stress intensity factor of single crystal
K_i: local stress intensity factor of the i^{th} grain boundary
k: effective shear strength of grain boundary
$\tilde{k}$: material constant
k^*: "cleavage-like" shear fracture resistance of the boundary
k_B: Boltzmann's constant
n: the number of edges of a grain
P: crack opening load
P_1: the critical load to initiate crack advance
P_2: the critical load to resume crack jump
P_3: the critical load to break through the grain boundary
$p(x)$: log-normal distribution function
$\tilde{r}$: distance to crack tip
r_p: plastic zone size
S_c: stiffness of specimen
s_{ij}: compliance constants
s: standard deviation of log-normal distribution function
T: temperature
T_{BD}: brittle-to-ductile transition temperature
U: activation energy of dislocation movement
v: loading rate
v_0: normalization loading rate
W_1: fracture work across grain faces
W_2: fracture work associated with the break-through of a grain boundary
W_3: work of separation of the boundaries left behind the penetrating cleavage front
w: distance between break-through points
w_c: average strip width in the process zone

LIST OF FIGURES

Fig.4-16 Slip systems at crack tip in group A specimens with [010] direction parallel to the desired crack propagation direction: (a) slip systems; (b) expected dislocation structure exposed on the fracture surface ABCD.

Fig.4-17 Slip systems at crack tip in group B specimens with [110] direction parallel to the desired crack propagation direction: (a) slip systems; (b) expected dislocation structure exposed on the fracture surface ABCD.

Fig.4-18 Schematic diagram of (a) stress field at crack tip; and (b) resolved shear stress of a slip system with the normal of slip plane of **n** and the slip direction of **m**. The fracture surface is ABCD; the slip plane is EFGH; $\tilde{\psi}$ is the angle between EADH and EFGH; $\tilde{\varphi}$ is the angle between IJ and **m**.

Fig.4-19 Plot of absolute value of g_{nm} on the inclined slip plane in group A sample with <100> axis parallel to the crack propagation direction (see Fig.4-16).

Fig.4-20 Plot of absolute value of g_{nm} on the oblique slip plane in group A sample with <100> axis parallel to the crack propagation direction (see Fig.4-13).

Fig.4-21 Plot of absolute value of g_{nm} on the rotated vertical slip plane in group A sample with <100> axis parallel to the crack propagation direction (see Fig.4-13).

Fig.4-22 Plot of absolute value of g_{nm} on the inclined slip plane in group B sample with <110> axis parallel to the crack propagation direction (see Fig.4-14).

Fig.4-23 Plot of absolute value of g_{nm} on the oblique slip plane in group B sample with <110> axis parallel to the crack propagation direction (see Fig.4-14).

Fig.4-24 Plot of absolute value of g_{nm} on the vertical slip plane in group B sample with <110> axis parallel to the crack propagation direction (see Fig.4-14).

Fig.4-25 Berg-Barrett x-ray image of fracture surface immediately behind the thermally arrested crack front shown in Fig.4-12. The dislocation pattern is very unclear due to the patchy nature of the cleavage surface and large Si content.

Fig.4-26 Berg-Barrett x-ray image of dislocation structure in front of an arrested crack front in a group A specimen indicated by the white arrow in Fig.4-12a. The dislocation pattern is very unclear because of the patchy nature of the cleavage surface and the relatively large Si content.

Fig.4-27 SEM photo of grain A in one of bicrystal specimens studied in Chapter 2.

Fig.4-28 Berg-Barrett x-ray image of fracture surface of grain A shown in Fig.4-17.

Fig.4-29 Profile of fracture surface along line A-A in Fig.4-26.

Fig. 4-30 Slip lines on the fracture surface of sample 100g shown in Fig.4-12, imaged with a Nomarski light interference contrast microscope: (a) slip lines tilted from the crack propagation direction by 45°, corresponding to the rotated-vertical-plane slip sustem; (b) slip lines parallel to the crack propagation direction, corresponding to the oblique-plane slip system; and (c) slip lines normal to the crack propagation direction, corresponding to the inclined-plane slip system (see Fig.4-16b).

Fig.4-31 (a) Fractography of cleavage surface of a single crystal of pure iron; (b) corresponding Berg-Barrett image.

Fig.5-1 An idealized traction separation TS profile demonstrating dissipative action in the process zone as proposed in the Andersson-Bergkvist model.

Fig.7-1 Various modes of entry of a cleavage front into individual grains: a) penetration into an exposed grain; b) penetration into a grain through a particularly weak boundary; c) and d) cracks entering into grains with an exposed corner.

Fig.7-2 Macrograph of a fracture surface of a compact fracture specimen of very coarse grained Fe-2%Si alloy. The vertical thickness dimension is 26mm.

Fig.7-3 Orientation relationship of cleavage facets in individual grains, relative to external specimen axes.

Fig.7-4 The cleavage fracture percolation map through the grains of the sample shown in Fig.7-2, showing also two crack arrest fronts A-A and B-B.

Fig.7-5 The calculated distribution of local stress intensity factors K_I along the fracture fronts A-A and B-B.

Fig.7-6 Histogram showing the distribution of numbers of grain edges in the fracture field of Fig.7-4, not counting grain edges bounded by free surfaces.

Fig.7-7 Computed cleavage fracture percolation map using information on grain boundary resistance determined by Eqn.(7-2).

Fig.7-8 a) A schematic view of the types of boundaries overcome by the cleavage front. Boundaries with emanating arrows are those that govern the form of penetration of the fracture front from grain to grain. Boundaries between 1-2, 5-6, and 2-4, in various measure, require extensive fracture work to bridge primary cleavage facets; b) simplified field in a generic square grain: (1) cleavage work inside grain; (2) work of fracture for going through the principal boundary controlling the percolation process; (3) boundaries requiring large amount of bridging fracture work by plastic shear and cleavage-like separation.

LIST OF TABLES

CHAPTER 1

INTRODUCTION

1.1 Statement of Thesis Objective

The abrupt fracture transitions in steel from ductile to brittle (D-B) or from brittle to ductile (B-D) remain of prime technological importance. In engineering practice where reliable service performance in steel structures requires a certain level of fracture toughness under any adverse condition, any abrupt excursion into brittle behavior is unacceptable. Over many decades certain mechanism-inspired operational design strategies have evolved based on relatively simple tests of the fracture transition in quasi-static and impact experiments that aimed to prescribe safe ranges of service variables such as temperature, loading rate and of microstructure etc. In addition, a large number of experimental alloy development studies have explored processing conditions that aimed to lower the D-B transition temperature in steels. While these studies and processing developments have been of unquestionable utility and are widely adhered to, they have shed little light on the fundamental mechanisms or processes that govern the transition, necessary for eventual definitive control of the phenomenon.

The area in particular need of further study is the interaction of the cleavage cracking process with grain boundaries. In the established procedures of testing of material response in the B-D transition range there is often a lack of clarity whether the observations and the developed formalisms relate to smooth bar deformation behavior or to experiments involving either initiation of or

growth of macrocracks or their continued propagation in a fracture mechanics context. The nature of strain concentration or its absence is very different in these two different forms of deformation, evoking different grain boundary - crack interactions. In this thesis, we will concentrate on fracture resistance of high-angle grain boundaries probed by sharp crack tip.

The central thrust of this research is the experimental study of the grain boundary resistance to cleavage crack growth in Iron-Silicon alloy as a close analog to the behavior of low carbon ferritic steels, and the development of associated models for the cleavage crack propagation resistance for bi-crystal grain boundaries and polycrystalline materials.

1.2 Previous Experimental and Theoretical Developments Concerning the Role of Grain Boundary in Cleavage Cracking

1.2.1 Fracture Resistance of Grain Boundaries

It is now generally recognized that a grain boundary is a barrier for cleavage crack propagation. In engineering practice, grain boundaries are involved in many fracture phenomena, such as fatigue failure, crack arrest, crack nucleation, brittle-to-ductile (B-D) and ductile-to-brittle (D-B) transitions, and so on (Stroh, 1954, 1955; Smith, 1966; Low, 1963; Ortiz, 1996). Dislocation models were developed for tilt, twist, and high-angle grain boundaries. Migration, sliding, and fracture of grain boundaries were observed in experiments and simulated numerically (Chaudhari and Matthew, 1972; Mahajan and Williams, 1973; Murr, 1975; Zikry and Kao, 1994; Gemperlova, Pol-

carova, and Bradler, 1991; Schwartz, Bristowe, and Vitek, 1987). Usually, low-angle grain boundaries are modeled as networks of edge dislocations or screw dislocations, and a high-angle grain boundary is considered as a thin layer of highly displaced atoms, often with the thickness of only a few atom planes. Among all these, the subject of high-angle grain boundaries and their roles in affecting the plastic resistance and fracture behavior of polycrystals has been of continued interest. In either case, grain boundaries compartmentalize processes in individual grains and break up both slip operations and limit the propagation of cleavage cracks from grain to grain.

The well-known Hall-Petch relation describes the dependence of the yield strength on grain size. It is also known that the ductile-to-brittle transition temperature (DBTT) strongly depends on grain size and grain boundary inclusions (Owen and Hull, 1963). Since twinning is an important factor in the initiation of cleavage fracture, due to the dependence on grain size of nucleation of twins: the smaller the grain size, the lower the DBTT. On the other hand, larger grain boundary inclusions, which usually exist in larger grains, may provide an easier channel for the cleavage crack to propagate, thus increasing the DBTT. Many other fracture behaviors of materials were also attributed to grain boundary inclusions. Failure of a few inclusions may trigger a macroscale cleavage failure. Weakest link theories were developed to take account of this phenomenon (Rosenfield and Shetty, 1983; Lin, Evans, and Ritchie, 1987; Xia and Shih, 1996; Knott, 1997).

The intrinsic interaction between a cleavage crack and a "clean" grain boundary without inclusions should also be of importance in engineering practice and fundamental research. How a dislocation penetrates through a bi-crystal twist grain boundary and the resulting crack nucleation

was directly observed by Smirnov, et al, 1985, who considered a grain boundary to be a barrier to dislocation movement and formation of cleavage microcracks by dislocation pile-ups.

The roles of grain boundaries introduced earlier in affecting the plastic resistance and fracture resistance of polycrystals, starting from considerations of initial yielding behavior to introducing intercrystalline constraints that influence compatibility of deformation between grains, have been actively explored over the years, but are not of interest in this thesis. In many respects, the role of grain boundaries in fracture is far wider in terms of phenomena than their role in modulating plastic deformation. Among the many effects of grain boundaries on fracture briefly discussed above, including initiation of microcracks by arrest of slip bands or deformation twins, and triggering of cleavage fracture through the cracking of grain boundary carbides, here we are interested primarily in the role of grain boundaries in modulating cleavage cracking across them.

In an early fundamental experimental study of the processes that lead to transitions of fracture from ductile to brittle forms in polycrystalline steel, Hahn, et al. (1959) noted that with decreasing temperature and rapidly increasing plastic resistance, prior to the onset of full brittleness, slip-induced dormant grain-sized microcracks appear. This demonstrated clearly that in the initiation of brittle response, while microcrack nucleation by obstructed slip or twin bands is an important precursor, such microcracks have to break through grain boundaries to initiate global brittle behavior, indicating that grain boundaries offer an important resistance to propagation of cleavage cracking among grains in the nature of acting as "fire breaks". It is this particular role of high-angle grain boundaries in affecting cleavage cracking resistance which retards brittleness that is of primary interest here. While this behavior has been well appreciated,

definitive studies of the effect to ascertain the nature of this fracture resistance in intrinsically brittle materials are rare. The few definitive studies have been limited to the assessment of such resistance by individual grain boundaries with known lattice misorientation by Gell and Smith (1967). Based on observations in hydrogen-charged Fe-3%Si alloy, they noted that the resistance of grain boundaries to the transmission of cleavage cracks across them is governed more importantly by the twist misorientation than the tilt misorientation across the boundary. They attributed this to a difficulty in initiating new cleavage cracks in the neighboring grains that would indeed be more strongly influenced by the twist misorientation.

1.2.2 Cleavage Crack Propagation across a field of grains

high-angle grain boundaries in steel offer an important resistance to the propagation of cleavage cracks, particularly in the brittle-to-ductile transition region. In a single crystal, the critical energy release rate for a cleavage crack to propagate was often considered to be the same as the effective surface free energy. In polycrystalline materials, the cleaving process of crystal planes will be interrupted when the crack encounters grain boundaries. Due to the crystal misorientation, the crack will change its fracture surface from the cleavage plane of one grain to that of another, and additional fracture work is required to overcome the barrier effects of grain boundaries. While there has been much emphasis on grain size effects on the plastic resistance (Hall, 1951; Petch, 1953) and the beneficial effects of grain size reduction on raising the brittle strength are well known (Petch, 1954), the specific role of grain boundaries in affecting cleavage crack growth resistance has not been clarified. Crocker, et al (1996) studied specific forms of break-through across boundaries and classified them into four types related to the observed

features of fracture along boundaries. In a quite detailed modeling study Anderson, et al. (1994) considered the mode of propagation of cleavage cracks across hexagonal grains and demonstrated that the cumulative probability of overall fracture in a "weakest link" context of triggering brittle response in structures is directly influenced by the impediments that grain boundaries have on cleavage crack propagation. The only detailed model of the role of grain boundaries on impeding the percolation of cleavage cracks across a field of randomly misoriented grains in steel is that of McClintock (1997). In this he proposed a number of criteria of overcoming individual grain boundaries by a quasi-statically advancing cleavage front and estimated the specific work of fracture due to plastic shear on grain boundaries bridging primary cleavage facets of adjoining cracked grains. There have been no corresponding experimental studies of these phenomena.

1.3 Previous Developments on the Brittle-to-ductile Transition

1.3.1 Fundamental Considerations of Mechanisms

The phenomenon of the abrupt ductile-brittle (D-B) fracture transition in engineering practice has been known at least since the famous Boston molasses tank fracture in 1919 (for an account of the catastrophe see The Boston Globe, 1989; related discussion is presented by McClintock and Argon, 1966); descriptions of other early non-ship brittle fractures were given by Shank, (1954). The more searching modern studies, with particular emphasis on steel, go back to the immediate post World-War II years. Nearly all the early research of that period was concentrated on estab-

lishing relatively global criteria for the fracture transition phenomenon through experiments on impact fracture, through study of notch effects, of alloying and processing conditions, that were deemed to be relevant in suppressing the Charpy V-Notch transition temperature (Parker, 1957). The considerations of the brittle fracture of steels received a major boost through the generalization of the Griffith criterion of brittle fracture by Irwin (1948) and Orowan (1949) who reinterpreted the effective critical energy release rate, to include in the work of fracture the plastic work of ligament tearing between adjacent cleaved grains. Moreover, it was recognized that microcracks that cause brittle behavior can be produced by arrest of intense shear bands (dislocation pile-ups) at grain boundaries (Zener, 1949; Stroh, 1954, 1955, 1957) or intersections of deformation twins (Hull, 1960). The role of these phenomena in brittle fracture of steels was summarized by Petch (1954). A comprehensive experimental study that had considerable impact in clarifying the microstructural phenomena associated with the brittle to ductile transition range of steels was that of Hahn, et al., (1959) on E-steel. This study established that in smooth bar experiments, with no initial crack present, brittle behavior in the lower shelf is indeed triggered through the production of grain-sized cleavage microcracks by the mechanisms discussed above, but that in many instances in the lower shelf, grain boundaries acted as "fire-breaks" relegating the microcracks dormant, often to be blunted and rendered harmless by further deformation. Complete global brittle behavior resulted at a temperature where apparently, the first such microcrack could break through grain boundaries under the high prevailing stress. The Hahn, et al., study remains as one of the most important sources of description of the phenomena of fracture transitions in steels, under conditions of quasi-homogeneous deformation.

In a set of basic considerations starting with Armstrong (1966), further amplified by Kelly et al. (1967) and finally sharpened by Rice and Thomson (1974), the fundamental notion of intrinsic brittleness vs. intrinsic ductility of materials was established, based on a scenario of the response of an atomically sharp crack tip to mode I loading in initially dislocation free solids. Thus, in the intrinsically brittle solids an energy barrier exists to the emission of dislocations from crack tips under conditions of impending crack growth by cleavage, resulting in brittle behavior at low temperatures. In intrinsically ductile solids there is no such energy barrier and dislocations can be emitted from the crack tip well before it can grow by cleavage. In spite of its kinetical shortcomings, the Rice-Thomson analysis has been remarkably successful in correctly classifying solids into intrinsically brittle and ductile ones. More recently, additional fundamental developments have removed the kinetic shortcomings of the Rice-Thomson model by considering increasingly realistic forms of saddle point configurations involved in the crack-tip emission of dislocations (Argon, 1987; Cheung et al., 1991; Schock and Puschl, 1991; Rice, 1992; Rice et al., 1992; Rice and Beltz, 1994; Xu et al., 1995, 1997). Through these more precise studies it has now been well established that the "saddle point" configuration for dislocation emission responsible for the transition to ductile behavior, in a certain class of brittle solids, is the formation of an embryonic amount of dislocation core material at the crack tip under stress. Solids in this category include BCC transition metals such as α - Fe and some alkali halides. They are distinguished by the characteristic of possessing no significant energy barriers to kink motion along dislocation lines, resulting in a steep stress dependence of dislocation velocity. In these solids the saddle point configurations expand unstably in a field of decreasing stress and can result in bursts of dislocation multiplication. The best theoretical predictions of Xu et al., (1997) for α - Fe based on this mechanism gives a T_{BD} of 300K that is close to what is commonly observed in many steels. (However,

for a different conclusion that puts Fe and other BCC metals into the same category as elemental semiconductors and compounds, which is discussed below, see Hirsch and Roberts, 1997).

A larger set of brittle solids encompassing not only the elemental semiconductors of Si and Ge but possibly most other compounds, are those in which there is a substantial energy barrier to kink motion along dislocation lines, resulting in very sluggish dislocation mobility - (even at high temperatures) and in a nearly linear stress dependence of dislocation velocity. In such solids the B-D transition is governed by the mobility of the emitted dislocations away from the crack tip. Since Si is such a material and can be obtained commercially, free of dislocations in the form of large single crystals of high purity, and moreover has an extensively-developed base of understanding of its crystal plasticity (Alexander and Haasen, 1968; Alexander, 1986; Bulatov et al, 1995), it has proved to be a very fruitful model material for the study of the B-D transition (St John, 1975; Brede and Haasen, 1988; Hirsch et al., 1989; Chiao and Clarke, 1989; George and Michot, 1993; Brede et al, 1991; and Hsia and Argon, 1994, Argon and Gally, 2001). Through these studies a direct connection was established between the activation energy of dislocation motion and the T_{BD}, as well as key observations on the forms of dislocation emission from crack tips, in support of model predictions (Zhou and Thomson, 1991; George and Michot, 1993; Xu, et al. 1997).

As an alternative scenario to the basic forms of dislocation emission from crack tips described above, a different mechanism has been suggested by Khanta et al. (1994 a, b) based on notions of defect-mediated melting which envisions nucleation of dislocations *en-masse*, from highly stressed perfect crystal volume elements that are not necessarily connected to the crack tip. The

present evidence resulting from the experiments of Gally (1999) is strongly against this mechanism.

1.3.2 *Important Operational Procedures Related to the Ductile-Brittle Transitions in Steel Structures*

The simple Davidenkov model (see McClintock and Argon, 1966) representing competition between rate-independent brittle cleavage and rate-dependent plastic flow has stimulated much operational procedure for dealing with the D-B transition in engineering practice, based on mechanism-inspired phenomenology. A key element shaping these developments has been the observation of McMahon and Cohen (1965) that fracturing of large-grain-boundary carbides is much more often responsible for the formation of the grain-sized microcracks than dislocation pile-ups or intercepted deformation twins. An associated notion has been that such processes, either through the fracturing of the carbide or through the resulting grain-sized microcracks, serve to define the "brittle *strength*" or "cleavage *strength*" of the Davidenkov construction, and that reaching this brittle strength locally could be sufficient to trigger global brittle behavior. Moreover, this scenario has been widely considered to be equally applicable to the lower shelf region, setting off brittle response without much accompanying plastic relaxation, as well as being the cause of conversion of ductile-tearing-type fractures into brittle cleavage forms of crack propagation in the upper shelf. While the logic for this universal applicability of the triggering scenario has not been very tight, several models of it have achieved wide acceptance. In the first of these models by Ritchie, Knott and Rice (1973) (RKR model), the triggering of global brittle behavior has been postulated to result when the cleavage strength is reached over a characteristic length in the plastic zone near the tip of a ductile macrocrack. Based on curve fit results, the characteristic

length λ_c was considered to be $2d$, with d being the grain size, i.e. the triggering event was the sudden appearance of microcracks in two adjacent grains. However, subsequent investigations carried out by Knott and coworkers (Tweed and Knott, 1987; Bowen, et al., 1987) resulted in a substantial modification of this criterion of two adjacent fractured grains by replacing the critical condition with a characteristic length criterion over which the local stress reached the cleavage strength, where, however, this length could not be associated with a specific microstructural dimension. The basis for this modification was the observation by Tweed and Knott (1987) that in weld metal, global brittle behavior could often be triggered by the fracture of a single large silicate inclusion, overriding any apparent interaction of the final cracking process with grain boundaries. While this particle-cracking-trigger notion has been extended by Bowen, et al. (1987) to carbides in general, clear evidence in support of this connection has been absent in the above work. Nevertheless, the trigger notion has been widely accepted as the rationale for the widely-practiced "weakest *link*" developments representing the variability in the measured fracture toughness results of K_{IC} on a probabilistic framework, involving methodology familiar in the well-known Weibull statistics of brittle fracture. Accounts of the current Japanese practice in the use of the weakest link approach are presented in an ASTM Symposium (1994). Knott (1997) has given a critique of this approach, particularly in relation to the risks involved in the extrapolation of measured results to probabilities of brittle response of large scale structures.

The initiation of brittle cleavage behavior at the upper shelf (ductile-to-brittle transition) is always proceeded by a ductile-tearing-type of fracture, absorbing large amounts of energy. The weakest link approach has also been applied to this range of behavior. Here it is assumed that in the advance of a ductile-tearing-front, the advancing characteristic strain field which normally probes

the dimple-producing cavity nucleation events from small carbides, also probes larger inclusions which, once separated or are cracked, trigger the global brittle response. Xia and Shih (1996) have developed FEM models of this behavior, incorporating the probability of the macrocrack-front encountering large MnS or silicate inclusions, into the model through the usual Weibull statistics of a single event, leading to a brittle catastrophe. In their paper Xia and Shih also refer to many other additional simulations of similar type.

The validity of the "weakest-link" approach and its de-emphasis of grain boundary effects has been questioned on several grounds. Anderson, et al., (1994) have demonstrated that a traditional weakest link concept, applied to the triggering of global brittle behavior from the known crack-tip plastic strain fields, can not result in the observed steep probability patterns of the variability of the measured fracture toughness results. These authors demonstrate that the fracturing of single inclusions may be a *necessary* condition for initiating a brittle response but not a *sufficient* one since the final cleavage crack must propagate through a field of randomly misoriented grains, and that the interaction of the macrocrack with grain boundaries through the tearing of the bridging ligaments must make important contributions. Using a model that incorporates these interactions as a conditional probability proved to be more successful in accounting for the actual observed trends in the variability of K_{IC} results. Such grain boundary interactions have also been considered in detail by McClintock (1997) through evaluating specifically the ductile ligament tearing work by upper bound continuum models of simple shear for a brittle cracking front percolating by cleavage through a field of randomly-misaligned grains.

1.3.3 Energetics of dislocation nucleation from crack tips

As discussed above, the possibility of emission of dislocations from crack tips has been considered as a basic material characteristic governing a brittle to ductile transition in crystalline solids. Some of the more prominent modeling studies of dislocation emission from atomically sharp cracks subjected to various modes of loading (I, II or III) were referred to in Section 1.3.1 above. In the more recent of these simulations pioneered by Rice and coworkers (Rice et al., 1992), the progressive evolution of a critical configuration of an embryonic form of dislocation on a slip plane going through a crack front under mixed modes I and II was studied by using a realistic interplanar tension/shear potential. This led to the finding that the critical 2-D saddle point configuration of a dislocation emitted from the crack tip is in the form of dislocation core matter resulting in a relative inelastic crack-tip displacement of only half a Burgers vector, and is associated with a critical energy release rate, G_{IIC} that is just equal to the *unstable stacking energy* of two half spaces translated by a half Burgers translation. To obtain estimates of actual B-D transition temperatures, however, 3-D saddle-point configurations of dislocation embryos have to be determined. Such analyses in approximate form were performed by Schock and Puschl (1991) and more exactly by Rice and Beltz (1994) by a perturbation analysis. The latter, however, became rather imprecise for the interesting range of $G_{\mathrm{II}} < G_{\mathrm{IIC}}$. More accurate 3-D saddle point analyses of possible embryonic configurations of dislocations at crack tips on both inclined slip planes going through the cleavage crack front as well as on oblique slip planes cutting through the crack front were performed by Xu, Argon and Ortiz (1995, 1997) utilizing a variational boundary integral method developed by Xu and Ortiz (1993) earlier. In this approach the tension/shear potential of Rice was employed in modified form, tailored for the cohesive properties of α-Fe, and surface production resistances in the energetics of the saddle point configurations. These analyses showed

that the overwhelmingly preferred sites for dislocation emission were cleavage surface ledges and oblique planes bordering on free surfaces, both of which had been noted by George and Michot (1993) in their experiments. As already stated above, actual estimates of the T_{BD} for iron obtained by this method were around 300K, close to what is found for low-carbon steels.

Another form of simulation was the successful adaptation of the Riedel-Rice (1980) model of stress relaxation around cracks in creeping solids to the mobility-controlled brittle-ductile transitions in Si (Argon et al., 1997). This simulation did not only account very well for the experimentally-determined dependence of the T_{BD} on loading rate, $\dot{K}_I$, in Si single crystals, but could also quite successfully model the dislocation content of the critical plastic zones of thermally arrested cracks that achieve a full transition into ductile behavior, in excellent agreement with the experiments of Gally (1999).

1.3.4 Experiments on crack arrest in silicon single crystals

Previous investigations of the B-D transition of cleavage fracture in Si single crystals were carried out under less-than-ideal conditions in pre-cracked samples at different constant temperatures, either in constant loading rate experiments or under conditions of stress relaxation (St. John, 1975; Brede and Haasen, 1988; Hirsch et al. 1988, George and Michot, 1993), where the crack tip is subjected to changing conditions. In the experiments of Brede, Hsia and Argon (1991) and Hsia and Argon (1994), followed up by the most recent research of Gally (1999), a unique approach was taken. In these experiments, cleavage cracks in specimens of constant K-factor geometry or double cantilever geometry were propagated at given average velocities up a temperature gradient

until the crack was arrested at a certain characteristic temperature, by purely crack-tip-initiated plasticity, depending on only the average crack velocity. Apart from maintaining the driving forces on the crack nearly constant, the arrest experiment gives directly information for the activation energy ΔG^* of the key arrest process through the dependence of T_{BD} on crack velocity as, $\Delta G^* = k_B T_{BD} \ln(c/v)$ where v is the average crack velocity and c is the velocity of a shear wave.

In these experiments the expected dependence of the T_{BD} on average crack velocity was measured and gave an activation energy of the key arrest process as 1.9eV. which is close to the value of 2.2eV. for dislocation glide, established by previous investigators. Moreover, the crystal plasticity-based crack arrest processes were probed by a variety of complementary methods such as etch pitting and Berg-Barrett x-ray topographic imaging conducted at the Brookhaven National Laboratory facility. These demonstrated that the active slip systems involved in the crack arrest process were those on which dislocation emission is energetically favored, and that all dislocations in the crack-tip-shielding plastic zones had come from the crack tip. Moreover, the dislocation contents of these plastic zones were in excellent agreement with the model based on the Riedel-Rice (1980) development discussed above.

These findings have importantly clarified the brittle to ductile transitions in Si associated with thermal processes alone and point into the directions for applying them to the study of fracture transitions in polycrystalline ferritic steels involving the role of grain boundaries as the next most important factor. This was a subject of this thesis.

1.4 Organization of Thesis

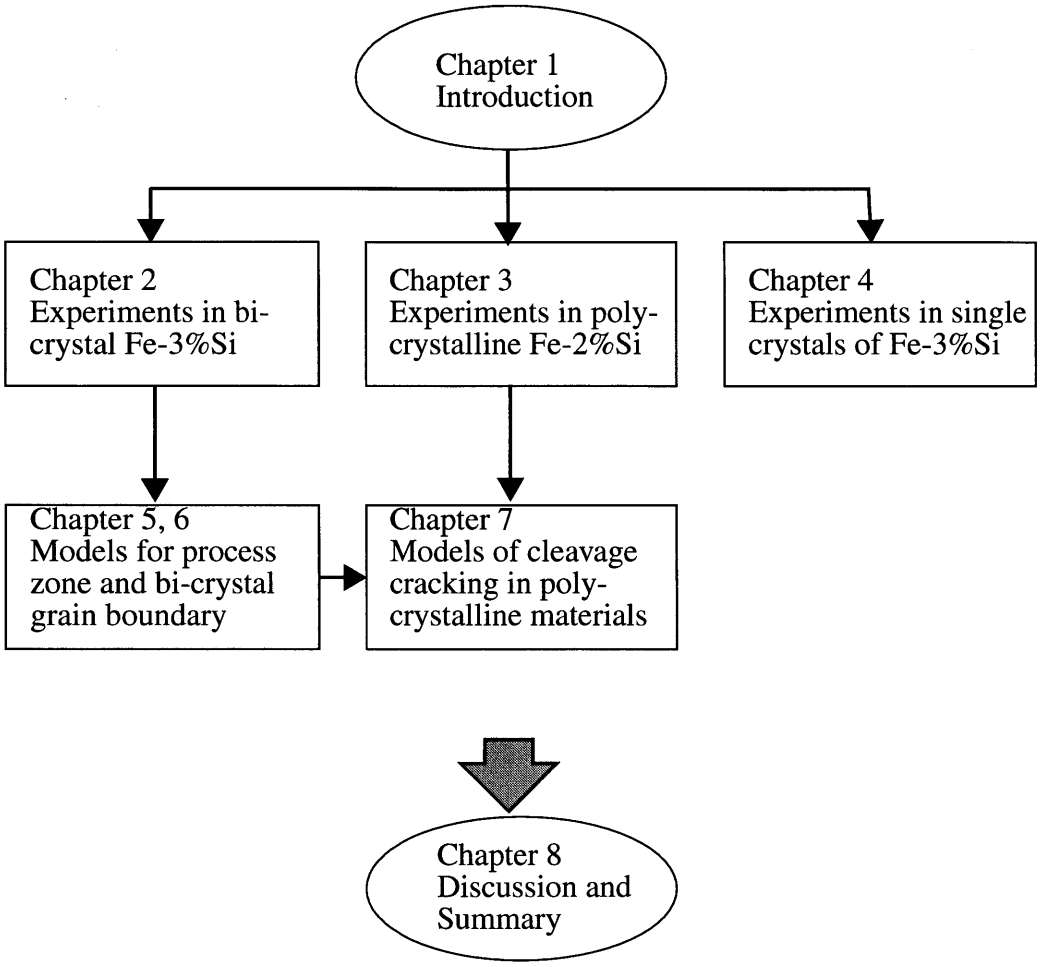

Fig.1-1 Organization of the thesis

In Chapter 1, the motivation and objectives of the current research are introduced, and related background about previous research of the role of grain boundaries in cleavage cracking is discussed. In Chapter 2, grain-boundary toughness measurement experiments on wedge-loaded double-cantilever beam (DCB) specimens of bi-crystals of Fe-3%Si alloy under various temperatures are introduced. The relationship between the critical stress intensity for break-through of high-

angle grain boundaries and the crystal misorientation was studied, and two different modes of break-through processes of cleavage cracking across grain boundaries were identified. In Chapter 3, the observed propagation modes of cleavage cracks across coarse-grained Fe-2%Si alloy samples are presented. Thermal crack arrest experiments that were performed in single crystals of Fe-3%Si alloy with (100) plane parallel to the median plane of the specimen and <100> or <110> axes parallel to crack propagation direction are presented in Chapter 4.

In Chapter 5, the relatively large fracture toughness measured in single crystals of Fe-3%Si was examined and interpreted by a process-zone model. Based on similar concepts, the PC/MC fracture transition was modeled as the processes of plastic bending and ductile shearing of cleavage ligaments left behind between adjacent cleavage strips. A mechanistic model that was developed is presented in Chapter 6 for peak resistance of individual high-angle grain boundaries to cleavage crack penetrating through them. The results fit with experimental data very well. In Chapter 7, a systematic analysis was performed for fracture resistance of polycrystalline material and grain-size effects.

Finally, in Chapter 8, the findings in this thesis will be summarized and discussed.

Figure 1-1 shows the framework of this thesis and relationship among chapters.

CHAPTER 2

BI-CRYSTAL GRAIN BOUNDARY FRACTURE RESISTANCE EXPERIMENTS

2.1 Material

The principal thrust in the experiments with bi-crystal grain boundaries was the assessment of their resistance to cleavage crack growth in iron and steel. This was pursued by a detailed study of the effect in a substantial set of bi-crystals with a wide range of lattice misorientation. The pursuit became possible through the donation of a large ingot of Fe - 3%Si alloy by the Allegheny Ludlum Steel Co. In the slowly-cooled ingot of about 12 cm thickness, the size of grains ranged from roughly 5 mm diameter on the surface to about 50-80 mm in the interior. The chemical composition by weight of the material as given in Table 2.1 indicates a substantial carbon content.

Table 2.1 Chemical Compositions of the Fe-3%Si ingots as received

Elements	C	Si	S	P
Content in weight (%)	0.63	3.4	<0.01	<0.01

Metallographic examination of the microstructure of the as-received ingot revealed a high concentration of very large size elongated carbides, ranging in size from 10 μm to fractions of a

millimeter, and with the carbide size increasing with increasing grain size. In addition, a high concentration of ubiquitous narrow deformation twins were also found in most of the possible variants. Preliminary cleavage studies of grains indicated quite significant perturbations to the growth of cleavage cracks by the narrow deformation twins and to a much lesser extent by the carbides. Nevertheless, the carbides were removed by a special two-step schedule of decarburization of the material, to be described below. Predictably, the deformation twins proved quite resistant to removal by any meaningful heat treatment.

2.2 Material Preparation

2.2.1 Harvesting of bi-crystals from the ingot

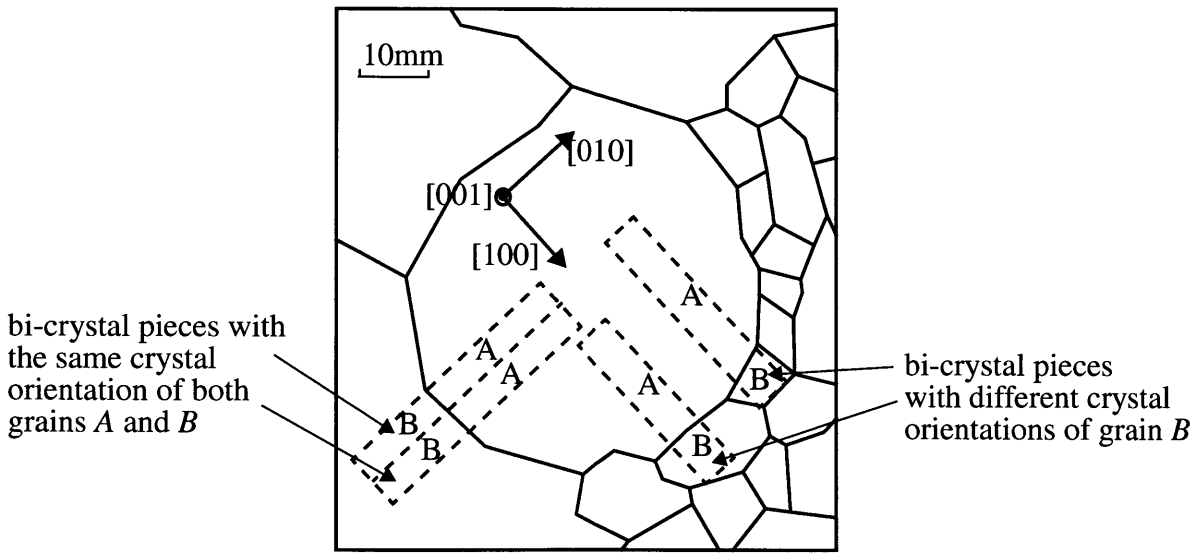

Fig. 2-1 Sketch demonstrating the method of harvesting bi-crystals from an *Fe*-3% *Si* alloy ingot containing large grains

The entire set of bi-crystals used in this investigation was harvested from a special block of Fe - 3%Si alloy ingot. The block of roughly 12cm thickness had lateral dimensions of 30×40 cm. Out of this block two slices of approximately 6 mm thickness were cut across the thickness direction of the block. The slices were surface ground to a fine finish. By virtue of the large grain sizes in the ingot, many grains in the slices were of a through-thickness nature. The surface-ground slices were etched in 3% *nital* for approximately 24 hours to reveal the low-energy (100) facets in the large collection of grains contained in the slice. Most grains, being randomly oriented in relation to the ground surface of the slice, produced pyramidal etching facets representing corners of cubes of {100} type planes. There were, however, also grains which exhibited only sets of two etching facets indicating that such grains contained one of their <100> directions lying in the ground surface. Finally, there were several quite large grains of 25-30mm diameter which contained no etching facets but only a set of shallow etch pits with flat bottoms, signifying that these grains had one of their {100} planes lying parallel the surface of the slice and containing two mutually perpendicular {100} planes perpendicular to the surface of the slice as depicted in the sketch of Fig.2-1. These grains with their adjoining family of attached smaller grains were candidates for extraction of bi-crystals. X-ray Laue back reflection analysis confirmed the accuracy of this method of determination of grain orientation by etching. Upon identification of the desired central grain, it and its surrounding grains were removed from the large slice by electrical discharge machining (EDM). The large, properly-oriented central grain was identified as *A*. Further EDM sectioning parallel to one or the other of the <100> type directions of grain *A* across its boundary into the surrounding grains then furnished a set of bi-crystal pairs *A* and *B*. Since two adjacent slices of the ingot contained further extensions of grains *A* and most of the surrounding *B* grains, a number of identical prismatic bi-crystal pairs could also be harvested, which were uti-

lized in repeating some experiments or to explore the temperature-dependent response of identical bi-crystal pairs. The orientations of the surrounding *B* grains were all obtained by X-ray Laue back reflection analysis.

Table 2.2 Characteristics of the 17 bi-crystal samples: measured values of K_{ICGB}/K_{ICA} and normalized experimental and computed toughness compared

Sample	1	2	3	4	5	6	7	8
ψ	0.175	0.210	0.331	0.157	0.140	0.122	0.140	0.594
φ	0.559	0.052	0.245	0.367	0.332	0.734	0.069	0.210
K_{ICGB}/K_{ICA}	1.461	1.049	1.168	1.226	1.192	1.575	1.042	1.233
$(\Delta K_{ICGB})_E/(\Delta K_{ICGB})_C$	1.132	0.942	0.977	0.967	1.046	1.096	0.964	0.984
Sample	9	10	11	12	13	14	15	16
ψ	0.229	0.402	0.052	0.385	0.210	0.367	0.490	0.524
φ	0.455	0.699	0.052	0.297	0.227	0.455	0.245	0.069
K_{ICGB}/K_{ICA}	1.283	1.602	1.036	1.225	1.141	1.404	1.204	1.121
$(\Delta K_{ICGB})_E/(\Delta K_{ICGB})_C$	1.030	0.923	1.002	0.995	1.000	1.078	0.969	0.921
Sample	17							
ψ	0.280							
φ	0.542							
K_{ICGB}/K_{ICA}	1.425							
$(\Delta K_{ICGB})_E/(\Delta K_{ICGB})_C$	1.073							

2.2.2 Characterization of lattice misorientations of surrounding grains

As will become clear from our experimental results to be presented below, the form of interaction of a cleavage plane with a grain boundary and its penetration into the adjacent grain *B* is governed primarily by the tilt and twist misorientations of the adjoining grain across the grain boundary, (see also Gell and Smith, 1967). The angles of tilt ψ, and twist φ of grain *B* across the grain boundary plane, relative to grain *A* can be given as (Fig. 2-2),

$$\psi = \frac{\pi}{2} - \text{acos}(\alpha_{31}\sin\beta + \alpha_{32}\cos\beta) \tag{2-1a}$$

$$\varphi = \frac{\pi}{2} - \text{acos}(\alpha_{31}\cos\beta + \alpha_{32}\sin\beta) \tag{2-1b}$$

in Eqns (2-1a) and (2-1b) α_{31} and α_{32} are the direction cosines locating the unit normal vector **n** of the principal cleavage plane of grain *B* relative to the axes **i** and **j** of grain *A*, parallel to the [100] and [010] directions respectively of that grain; and where β is the angle between a vector **d**, parallel to the line of intersection of the grain boundary with the principal cleavage plane (001) of grain *A* and its [100] direction as shown in Fig. 2-2. Ideally, the angle β should have been zero, but could not be controlled in the experiments. As the fractography show it was often in the range of 20^{o}-30^{o}, without any significant effect on the mechanisms discussed below. While the inclination of the plane of the grain boundary also requires an angle α giving the rotation of the plane of the boundary about the vector **d** in the boundary, this degree of freedom is considered inessential since the interaction of the cleavage crack in grain *A* with the grain boundary in its traverse into grain *B* is primarily governed with respect to a virtual boundary perpendicular to the cleavage plane ($\mathbf{n_A}$). Through the form of preparation of the bi-crystals it was possible to obtain 17 different bi-crystal pairs with relatively random distribution of tilt and

twist angles ψ and φ of grain *B* relative to the boundary planes with grain *A*. The different tilt and twist angles of these 17 different bi-crystals are given in Table 2.2.

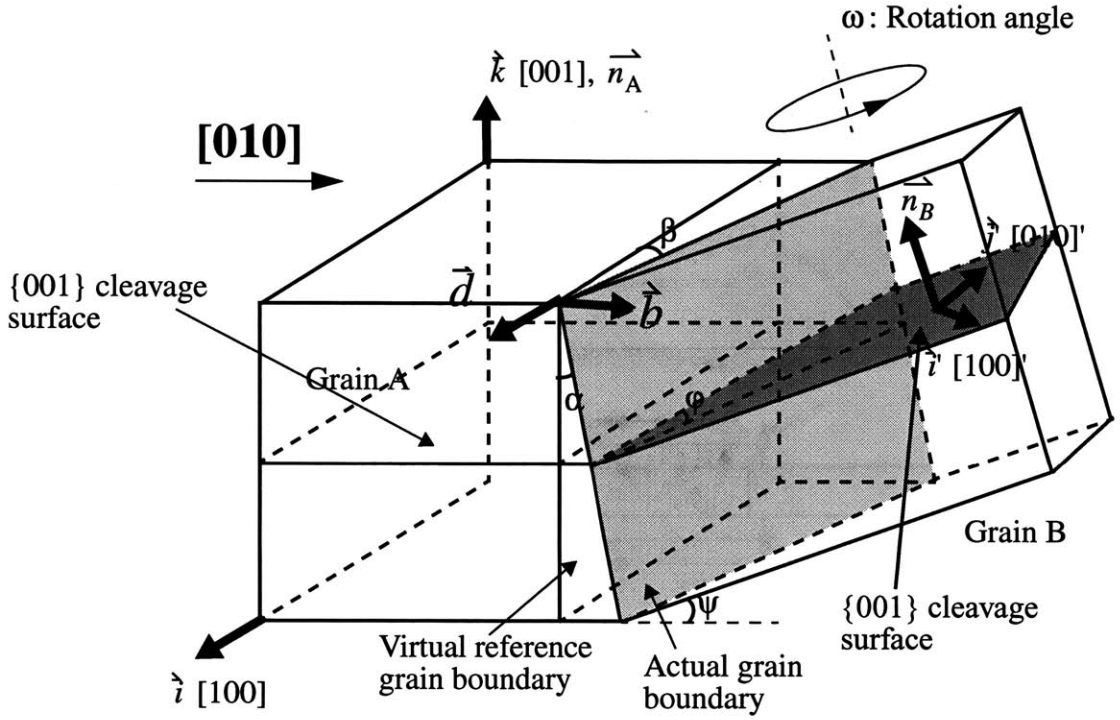

Fig.2-2 Determination of lattice tilt and twist misorientations across a grain boundary in a bi-crystal.

2.2.3 Decarburization of bi-crystals

To eliminate the complicating and undesirable interactions of cleavage cracks with the large carbides, all bi-crystals were decarburized according to a stringent schedule (Birks, 1969; Thelning, 1984). The schedule consisted of first breaking-down the carbides by a prolonged period (60 hours) of soaking of the bi-crystals at 1400C in a nitrogen environment, which successfully dissolved all carbides. This treatment was followed without interruption by a holding time of 2.5 hours at 1200C in a hydrogen environment to extract the dissolved carbon. The schedule ended with a slow furnace cooling to prevent entrapment of hydrogen and

embrittlement. The remaining carbon in the decarburized bi-crystals was less than 0.1% by weight and entirely in solution. A final *picral* etch detected no carbides in the grains. There was no measurable change in the *Si* content as a result of the decarburization treatment. As expected, the prolonged decarburization treatment had no effect on the population of the narrow deformation twins.

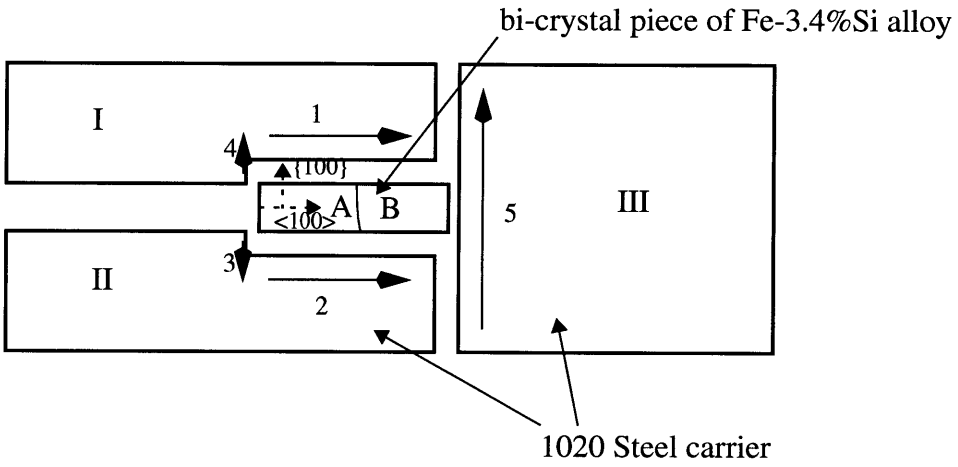

Fig. 2-3 Schedule of assembly by EB welding of bi-crystal slabs into 1020 steel carrier blocks to form DCB specimens.

2.2.4 Welding of bi-crystals into double cantilever beam "carrier" samples

The average size of the harvested and decarburized bi-crystal slabs was $40 \times 10 \times 4$ mm. These were electron-beam welded into fine-grained 1020 steel carriers according to a special welding procedure to minimize residual stresses in the construction of the double cantilever beam (DCB) specimens. The procedure is depicted in Fig. 2-3, showing the five separate welding paths to attach the bi-crystal slabs to the three 1020 steel blocks (always individually produced for each bi-crystal) with minimal distortion. The unwelded space between blocks I and II becomes the

main part of the initial crack. After welding, the DCB specimens were stress relieved at 400C for 2 hours, and subsequently surface ground to a final thickness of somewhat under 4.0mm. To reduce the risk of cleavage cracks turning out of the desired median plane, shallow side grooves of 60^{o} angle were machined by a special cutter with a contoured tip. The combined depth of the side grooves reduced the central ligaments of the DCB samples to b_n roughly 3.0 mm. At the tip of the crack, grain *A*, was provided with a 45^{o} chevron by EDM milling. In this manner 17 DCB samples were prepared for the first phase of the investigations at -20C.

2.3 Single Crystal Tension Tests

Single crystal tension specimens were cut out from a single large grain to carry out stress-strain experiments to determine the temperature dependence of the plastic resistance of the material of interest for reference. These specimens had not been decarburized since the remaining carbon in the material outside the carbides was at the solubility limit and that the relatively small volume fraction of the large carbides would affect the plastic resistance only to a minor extent. The Schmid factor for the principal {110}<111> type slip system was 0.44 while that for the alternative {112}<111> system was 0.37. Because of the low temperatures in the test and the higher Schmid factor, the $(110)[1\bar{1}1]$ system was taken to be the active one in the evaluation of the plastic glide resistance.

2.4 The Wedge-loading Test Configuration

To achieve the best conditions of propagating the cleavage cracks to probe the grain boundaries in the bi-crystals, a stiff loading system having a minimal compliance C_m was designed, and is shown schematically in Fig. 2-4. The DCB specimen containing the specific embedded bi-crystal was pried apart by means of a hardened steel wedge with a wedge angle of 10^o. To reduce

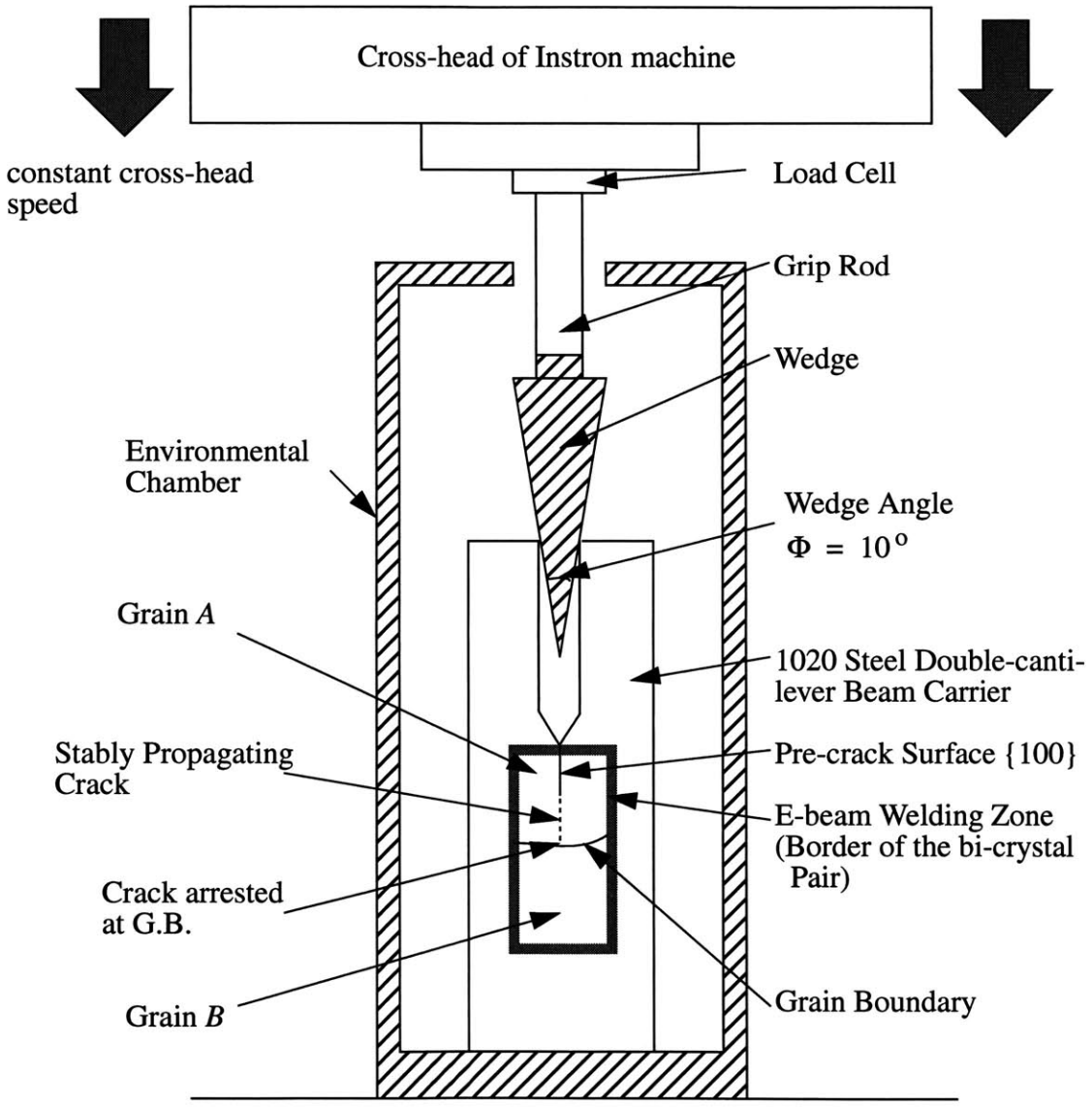

Fig. 2-4 Arrangement to perform wedge-loaded crack propagation experiments in DCB samples.

friction between the DCB specimen slab and the wedge, both contacting surfaces were covered with a graphite spray. The wedge was driven-in by the cross-head of a type 5508 Instron machine. The wedge insertion load was measured by a type LW0-300 flat compression load cell, having a compliance $C_{lc} = 1.86 \times 10^{-11}$ m/N given by the manufacturer, Transducer Techniques Inc. The loading rod, made out of solid type-304 stainless steel was kept as short as possible. The measured overall compliance C_m of the loading system was 9.0×10^{-8} m/N which was roughly 1% of the opening compliance of a typical DCB specimen.

An environmental chamber made up of aluminum sheet metal with an external layer of Styrofoam insulation, contained a Plexiglas window for viewing the specimens. The temperature in the chamber was maintained directly by a stream of cold nitrogen gas, fed into the chamber, and was controlled at a desired set-point by an Omega JK12 controller through a cryogenically-rated solenoid valve in the liquid nitrogen piping system. Temperature uniformity in the specimen, in equilibrium with its surroundings, was reached typically within 15 minutes.

2.5 The Ideal Wedge-loading Experiment

Figure 2-5 represents the idealized response of the DCB specimen to the propagation of a cleavage crack across a single grain boundary in a bi-crystal. While the actual behavior always differed from the idealized one, the latter serves to give a well-defined framework to evaluate the response in a quantitative manner.

In the ideal response, the crack in grain A begins to grow when the load reaches P_0 at the opening displacement δ_1 where the elastic energy release rate from the DCB specimen equals

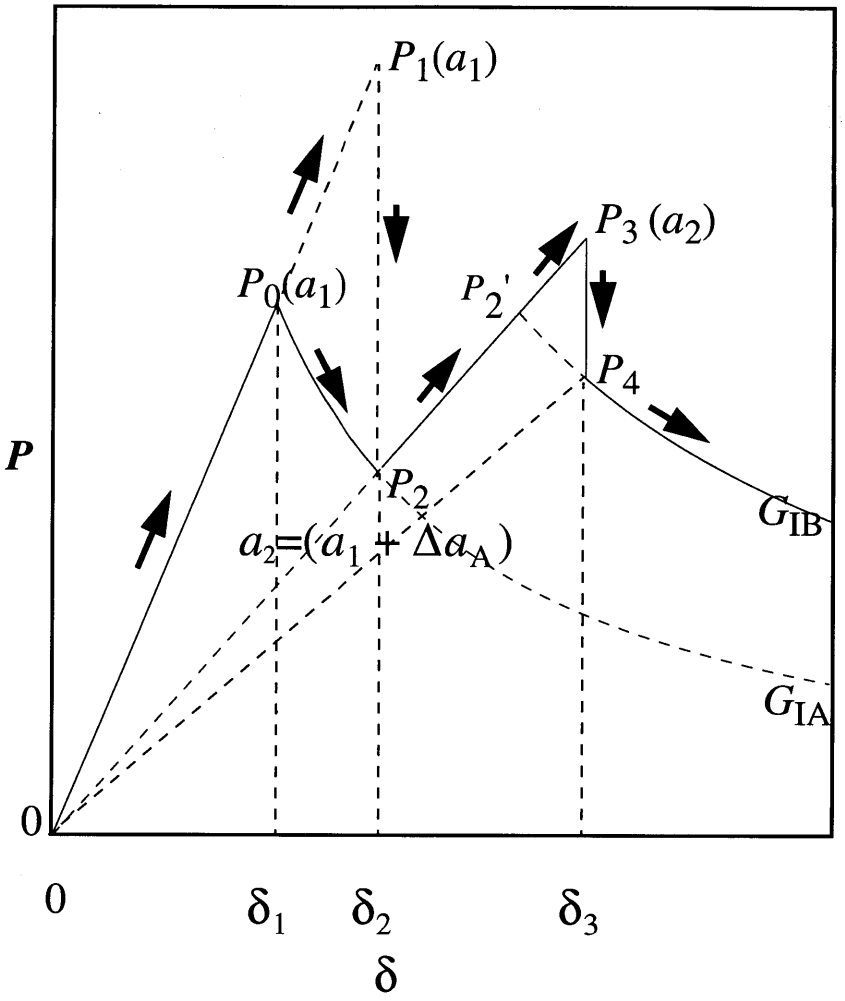

Fig. 2-5 Idealized opening load vs. opening displacement response characteristic of the DCB specimen in a "reversible" manner.

the specific work of fracture G_{ICA} of grain A (or its critical energy release rate) following a characteristic descent curve P vs. δ, given by:

$$P = \tilde{D}\frac{G_{ICA}^{3/4}}{\delta^{1/2}} \tag{2-2}$$

where $\tilde{D} = (Eh^3)^{\frac{1}{4}}\left(\frac{b}{8}\right)\left(\frac{16}{3}\right)^{\frac{3}{4}}$ is a constant of the DCB specimen, b is the DCB specimen thickness, and h is the height of each of its arms.

The crack grows by Δa_A until it encounters the grain boundary at a load P_2 and opening displacement δ_2. The area (OP_0P_2) of the P vs. δ diagram represents the work of crack extension by Δa_A, giving an estimate for G_{ICA}:

$$G_{ICA} = \frac{Area(OP_0P_2)}{b_n \Delta a_A} \tag{2-3}$$

where b_n is the thickness of the DCB specimen across the roots of the side grooves. At this point the cleavage crack probes the grain boundary and begins to penetrate into grain B in which, by virtue of its misorientations, and for reasons to become clear by the fractographic evidence described below, the specific work of fracture in grain B, G_{ICB}, (in terms of crack growth in the median plane of the DCB specimen) is larger than G_{ICA}. Thus, to initiate a further extension of the crack from a length of $(a_0+\Delta a_A)$ requires a load increase along line OP_2 to past point P'_2, to point (P_3, δ_3) where the peak grain boundary penetration resistance is reached and the crack advances under an excess driving force into grain B by an amount Δa_B in a sudden jump, accompanied by a characteristic load drop $\Delta P = P_3 - P_4$. During this crack jump, a certain work W_{gb} of breaking-through the GB is coupled with an increment of work of fracture of grain B over the crack growth increment of Δa_B. In Fig. 2-5 the former is represented by the area $(P'_2P_3P_4)$, while the latter corresponds to area (OP'_2P_4). In the experimental evaluation of the

resistance of grain boundaries, the above separation of the effect into work of boundary break-through and cleavage crack propagation in grain B was not made, and the entire effect was evaluated simply by defining the stress intensity increment ΔK_{ICGB} based on $\Delta P' = P_3 - P_2$ of Fig. 2-5 representing the collective actions of the resistance of the *GB* to break-through.

In the actual wedge loading experiment the initial penetration of the cleavage crack into grain A is not quasi-static but always requires an excess of "driving force" indicated by the dotted rise of load to P_1, due to a variety of imperfections at the initial crack tip. The crack then jumps through grain A under decreasing load ($P_1 \rightarrow P_2$) until it is stopped at the grain boundary.

2.6 Results of Single Crystal Experiments

The temperature dependence of the tensile yield stress and the critical resolved shear stress on the primary {110}<111> system and the alternative {112}<111> system is given in Fig.2-6. The calculated RSS rises from a plateau of around 150C from a level of 80MPa with increasing slope to a substantial level of 240 MPa around -50C. The higher temperature plastic resistance at 150C is most likely governed by the solid solution strengthening of the 3% Si. The rise below 50C is attributed to a combination of lattice resistance and solid solution resistance. The low temperature plateau below -50C and the quite erratic behavior there is attributed to an onset of deformation twinning. Figure 2-6 also shows a corresponding rise in the fracture stress which, below -50C, is far less affected by twinning. For our modeling discussed in Chapter 6, we are interested in RSS on the {110}<111> system.

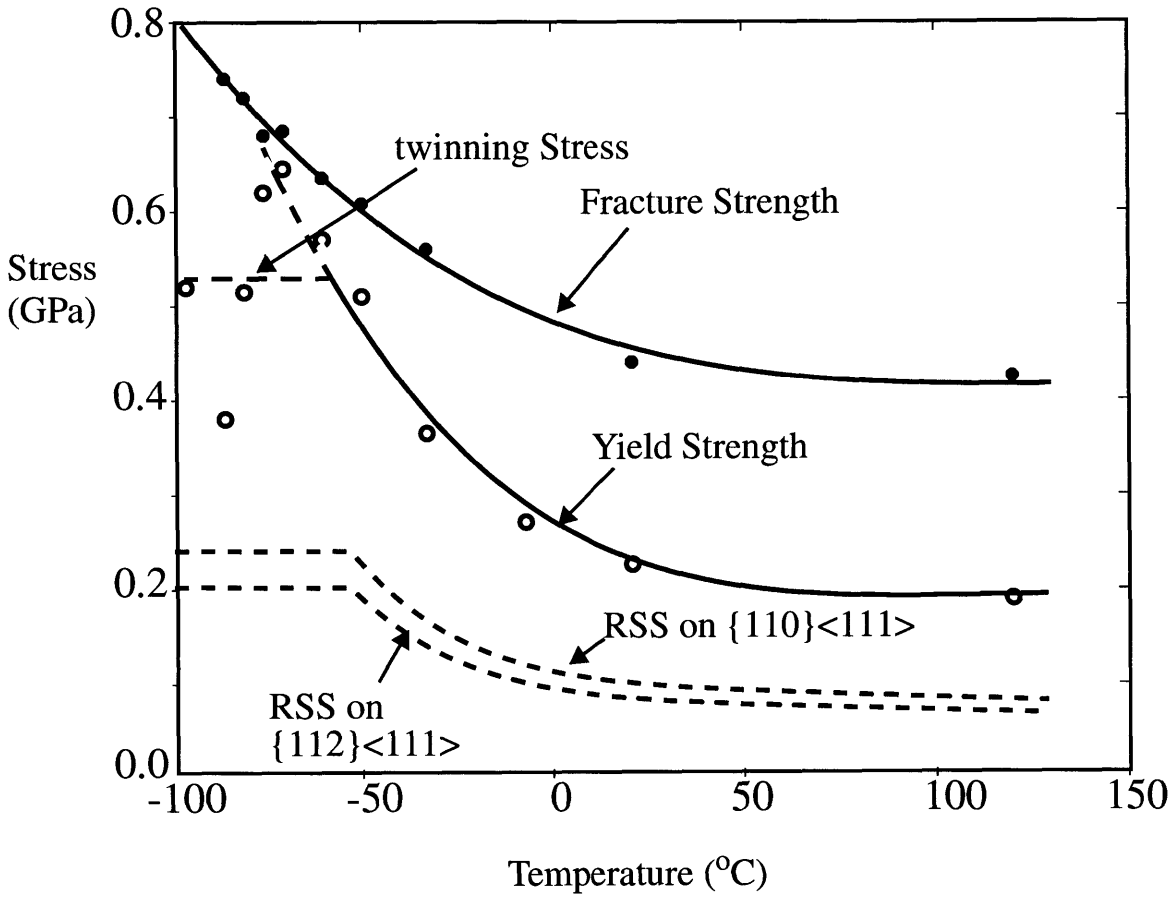

Fig. 2-6 Temperature dependence of the tensile yield strength, tensile fracture strength, and resolved shear stresses on the {110}<111> and {112}<111> slip systems on single crystal tensile tests of the *Fe* - 3%*Si* alloy. The dotted horizontal line through the region of scatter reflects an approximate level of twinning-controlled yielding.

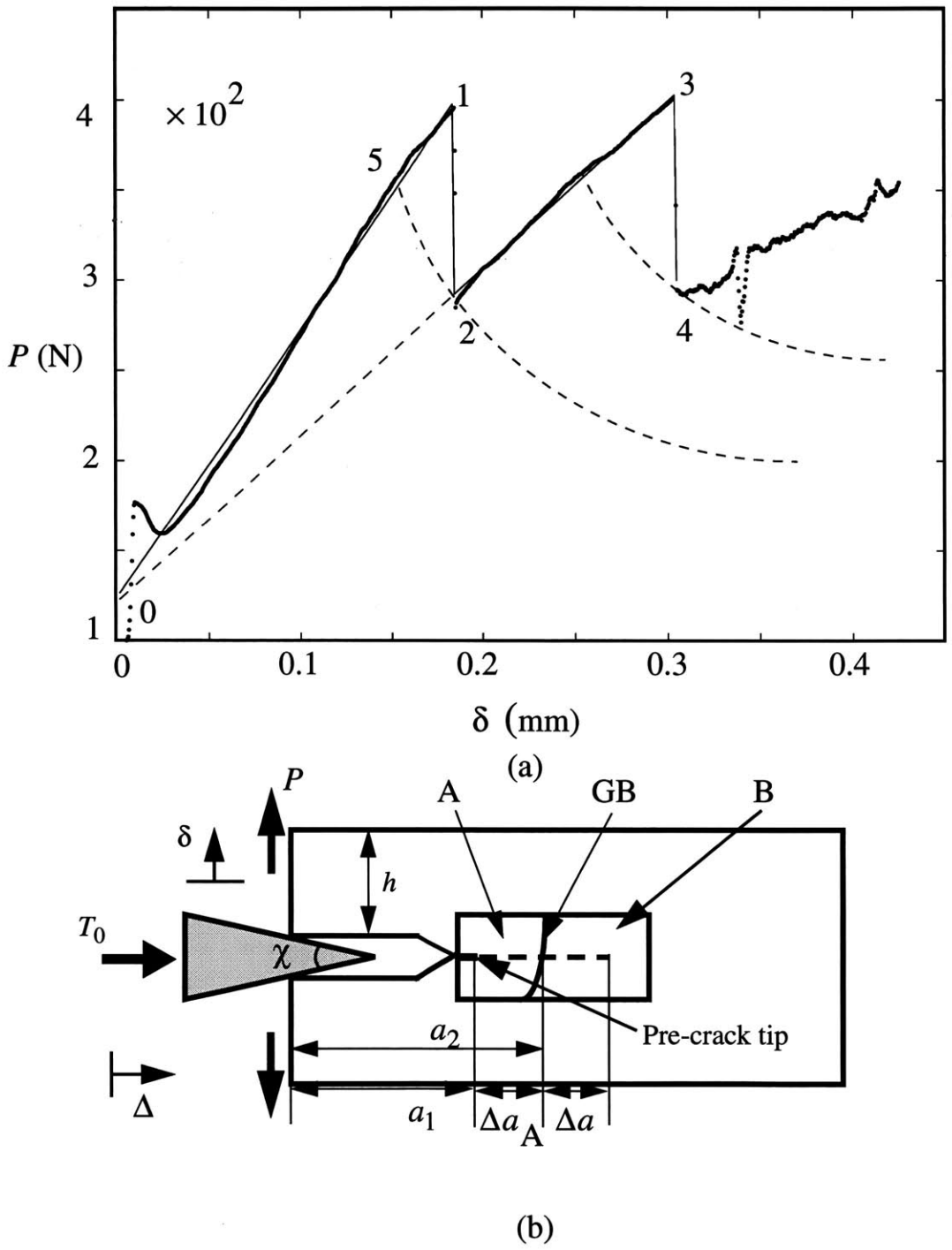

Fig. 2-7 (a) An actual $P(\delta)$ curve for a wedge loading experiment of sample 4 depicted in (b).

2.7 bi-crystal Fracture Experiments at -20C

Figure 2-7a shows the dependence of the DCB opening force P on the associated crack opening displacement δ at the contact point of the wedge in sample 4 (see Table 2.2). The values of P and δ were calculated through $P = T_0 / \left(2\tan\frac{\chi}{2}\right)$ and $\delta = \Delta\tan\frac{\chi}{2}$, respectively, with χ being the wedge angle, T_0 being the load acting on the wedge measured by the load cell, and Δ being the displacement of the wedge measured by LVDT (see Fig.2-7b). Because the crack tip was imperfect as-produced, the crack propagation was not of a quasi-static nature as outlined in Section 2.5. In the figure, the solid contour represents the recorded experimental data while the dashed curves are the fitted ideal response characteristics that resemble those discussed in Section 2.5. During the load rise from 0-1 the crack, of length a_1 (55.4mm) in Fig. 2-7b elastically flexes, exerting an increasing stress intensity. At a point past 5 of the initial DCB flexure line, the crack begins to grow across the chevron, indicated by the slight decrease of the loading slope. Because of crack-tip imperfections, the crack becomes overstressed to reach a K_I-level exceeding somewhat the K_{IC} for quasi-static growth. At point 1, K_I for initiation of crack growth is reached, the overstressed crack jumps in an unrestrained manner across grain A, and comes to rest at the grain boundary. At this stage the crack probes the grain boundary and, in a way that will become clear from the SEM observations, it begins to penetrate partially into grain B, but a full penetration requires an increase in the crack "driving force" K_I along a new loading line with smaller slope, due to the increased compliance. When point 3 is reached, under the increment ΔK_I, the crack breaks through the grain boundary and penetrates into grain B by a

further unstable jump. The crack comes to rest on the opposite border of grain B with the polycrystalline background, i.e., at point 4. The subsequent serrated loading behavior past point 4 conveys no relevant information.

The curve of Fig. 2-7a shows that frictional effects are still present between the wedge and the contacting faces in the DCB specimen, demonstrated by the fact that the loading does not start from zero but from a finite resistance. This artifact is formally rectified by shifting the origin of the loading curves to zero.

From basic beam theory the stress intensity probing the crack tip in grain A at the start can be stated as

$$K_I = \Gamma P a \tag{2-4}$$

where

$$\Gamma = \sqrt{\frac{12}{(1-\nu^2) b b_n h^3}} \tag{2-5}$$

where P being the applied DCB opening load with an initial crack length of a_1, and the other quantities are as defined in Section 2.5 above. Thus, the initial crack growth resistance K_{ICA} for grain A, then is:

$$K_{ICA} = \Gamma P_1 a_1, \tag{2-6}$$

where a_1 is the initial crack length and P_1 the critical load to initiate its extension at point (1) in Fig. 2-7a. The unstable jump of the crack is arrested at point (2), when the crack runs into the grain boundary.

Finally, the stress intensity K_{I3} to break through the grain boundary can be taken similarly to be

$$K_{I3} = \Gamma P_3 a_2 \tag{2-7}$$

where a_2 is the total crack length abutting on the grain boundary. Then, the incremental fracture toughness ΔK_{ICGB} attributable to the grain boundary fracture resistance can be taken as

$$\Delta K_{ICGB} = \Gamma a_2 (P_3 - P_2) \tag{2-8}$$

In this manner altogether 17 bi-crystal samples of different lattice misorientations between grains B and A were probed. The resulting measurements of the ΔK_{ICGB}, normalized with the overall average K_{ICA} for these 17 bi-crystal experiments are given in Table 2.2 as a function of the individual tilt and twist angles, ψ and φ. The overall average of the measured K_{ICA} was $14.1 \pm 0.6 \text{MPa}\sqrt{\text{m}}$. This value, compared with the value of $2-3 \text{MPa}\sqrt{\text{m}}$ corresponding to the surface free energy of about 10J/m^2 (Hondros and Stuart, 1967), is of substantial magnitude and requires an explanation, which we will provide in Chapter 6. Examination of the reported values of K_{ICGB}/K_{ICA} in Table 2.2 shows a clearly discernible increase with the twist angle φ.

Table 2.3 Measured normalized K_{ICGB}/K_{ICA} for the two specimen sets of bi-crystal experiments carried out in the temperature range of -20°C to 21°C.

T (°C)	-20	-10	-6	-3	0	2.5	5	10	21
Set "C"(*)	1.587	1.312	1.319	1.631	1.936	-	-	-	1.814
Set "D"(**)	-	1.114	1.106	1.199	1.340;1.262	1.426	1.348	1.440	1.503

(*) bi-crystal set "C" had $\psi = 7°$ and $\varphi = 42°$.
(**) bi-crystal set "D" had $\psi = 8°$ and $\varphi = 12°$.

The above development is based on simple beam theory. Somewhat more exact developments are possible, such as that given by Kanninen (1973), but differ in results from the simple theory by less than 5%.

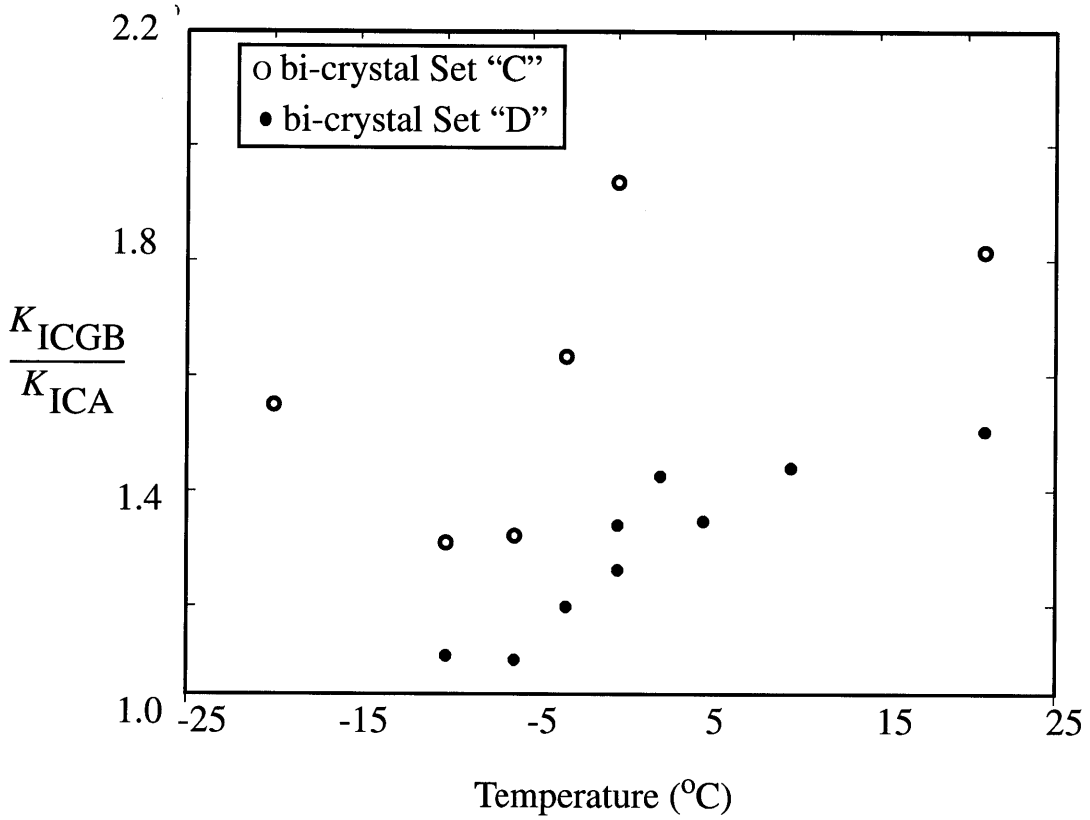

Fig. 2-8 The temperature dependence of the normalized grain boundary break-through toughness for two special orientation "C" (o) and "D" (*) showing a cleavage to *mixed cleavage* transition at about 0C.

2.8 Fracture Transition Experiments in bi-crystals

To explore how the grain boundary modulates the cleavage cracking across it with changing temperature, two sets of additional bi-crystal samples were prepared for use in wedge cracking experiments in a temperature range between -20C and 21C. In the first set, which we label as set "C", it was possible to use six other available bi-crystal samples of type "6" in Table 2.2, i.e.,

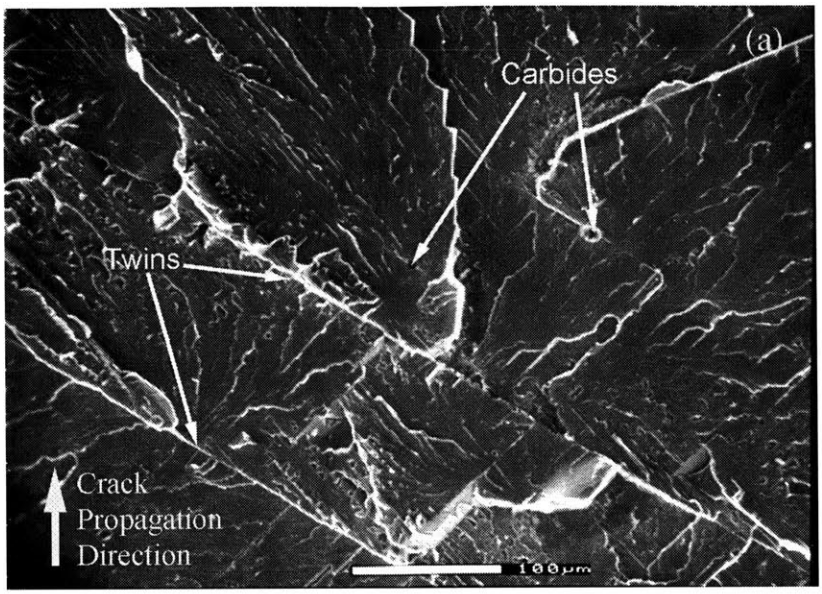

(a)

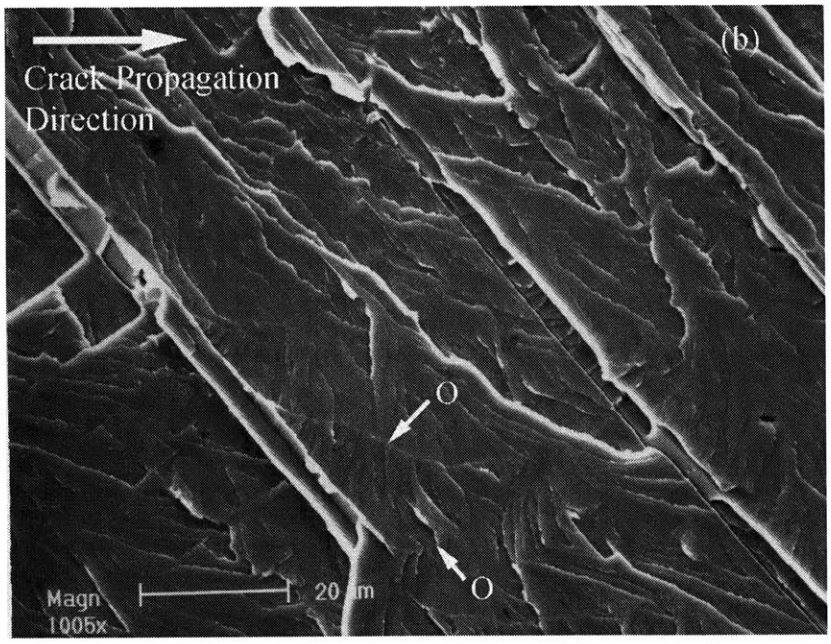

(b)

Fig. 2-9 SEM micrograph of fracture surface of grain *A* before decarburization showing repeated arrest and re-initiation of the cleavage crack by deformation twins (b) same observations after decarburization.

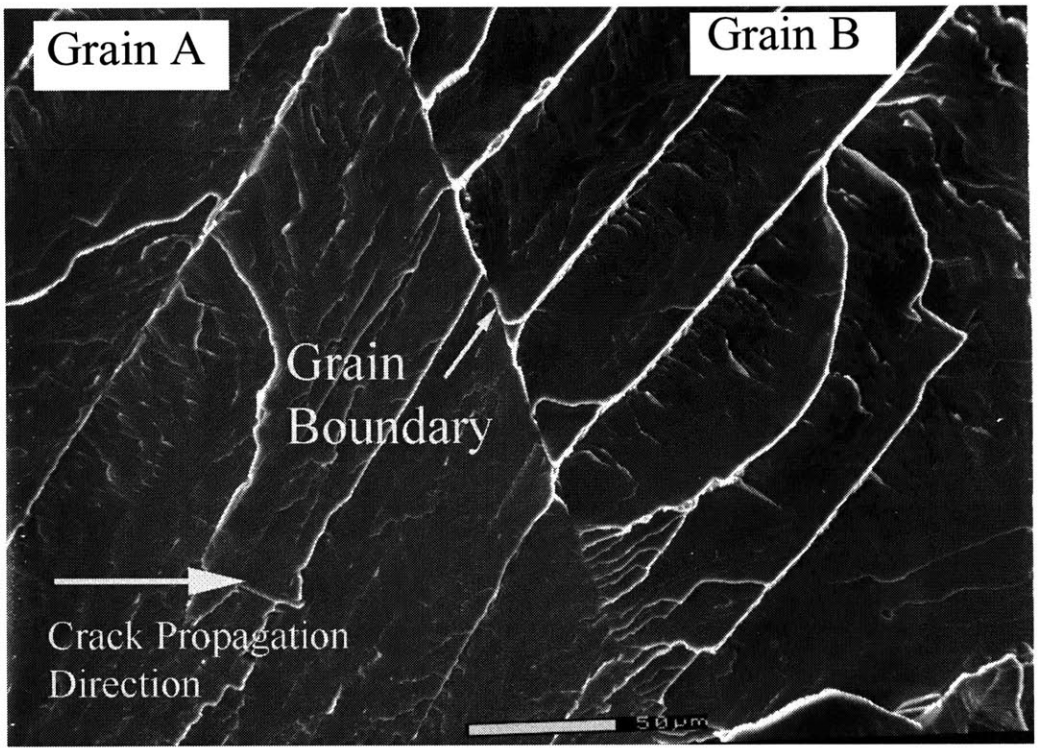

Fig. 2-10 SEM micrograph showing a "regular mode" of entry of a cleavage crack across a grain boundary into grain *B* along a series of twisted tiered cleavage strips in a specific case of bi-crystal 14.

with tilt and twist angles of $\psi = 7^o$ and $\varphi = 42^o$. For the second set nine bi-crystals of a rather different misorientation consisting of $\psi = 8^o$ and $\varphi = 12^o$ were extracted from the remaining large slice of the same ingot. This set is labeled as "D". The measured K_{ICGB} values normalized with K_{ICA} are listed in Table 2.3 and are also shown in Fig. 2-8 as $\Delta K_{ICGB}/K_{ICA}$ over the temperature range, where K_{ICA} is considered temperature-independent. The figure shows that there is a readily recognizable transition in the grain boundary cracking resistance between -2C and 0C in these two sets. The increment in cracking resistance is distinctly higher in set "C" with the larger twist misorientation angle. The nature of this transition will be clarified with the SEM fractography observations presented below. Since the fracture appearance in the entire temperature range remains to be substantially of a cleavage nature, the transition has been labeled as a *cleavage to mixed-cleavage transition.*

2.9 Fractographic Observation

2.9.1 Fracture surfaces in grain A

Figures 2-9a and 2-9b show portions of the cleavage fracture surfaces of grain *A* at -20C for a case without decarburization, and one with decarburization respectively. Figure 2-9a shows that the crack has been intercepted by the occasional large carbides. However, there are no significant emanations of cleavage river markings from these encounters, indicating that they have not played a significant role in the basic cleavage fracture. A much more significant interaction of

the cleavage crack occurs with the deformation twins. There are many examples in both figures of repeated arrest of the cleavage crack by the narrow twins followed by points of break-through marked by river markings emanating form these points. Stereoscopic observations of the encounters of the crack with twins indicated that these repeated arrest and reinitiation events of the cleavage crack by twins, fragments the crack plane into separate strips advancing at different levels. Since the fracture toughness in cleavage-like fractures correlates well with the fracture surface roughness, this roughness was measured with a *Zygo Interferometer*[1] on several fracture surfaces of grain *A* in the low temperature range and was found to be of a rms roughness amplitude of $2.7\mu m$.

2.9.2 Fracture across grain boundaries at -20C

Detailed fractographic examination of the penetration of the cleavage crack from grain *A* across the boundary into grain *B* exhibited two limiting modes. Figure 2-10 is a micrograph showing the dominant limiting mode identified as "regular", of entry of the cleavage crack from grain *A* into grain *B* in bi-crystal 14 ($\psi = 21^{o}$; $\varphi = 26^{o}$). After initial arrest, and within the characteristic increment of crack tip driving force, as depicted in Fig. 2-5, the arrested cleavage crack front penetrates into grain *B* at a number of relatively evenly spaced points a characteristic distance *w* apart. The fully-penetrated cleavage crack in grain *B* forms a series of "stair-case-like" tiers with flat surfaces of width $w/\cos\varphi$, with the twist inclination φ of the planes relative to the cleavage crack plane in grain *A*. In a transition-region the individual cleavage facets bow into the

1. An instrument that uses scanning white light interferometry to image and measure the micro structure and topography of surfaces in three dimensions (New View System 5000, produced by Zygo Corp. of Middlefield, Connecticut).

designated strips from their entry points as depicted in Fig. 2-11, forming the tiered primary cleavage facets of grain *B* and in the process producing secondary cleavage-like fracture facets connecting up cleavage strips in grain B. At the critical condition, the remaining grain boundary facets also give way by a combination of shear fracture or plastic shearing off, to complete the stair-case-type propagation of cleavage into grain *B*. The river line steps associated with the crack growth was discussed by Hull (1997) as a consequence of local mixed mode I/III condtiions.

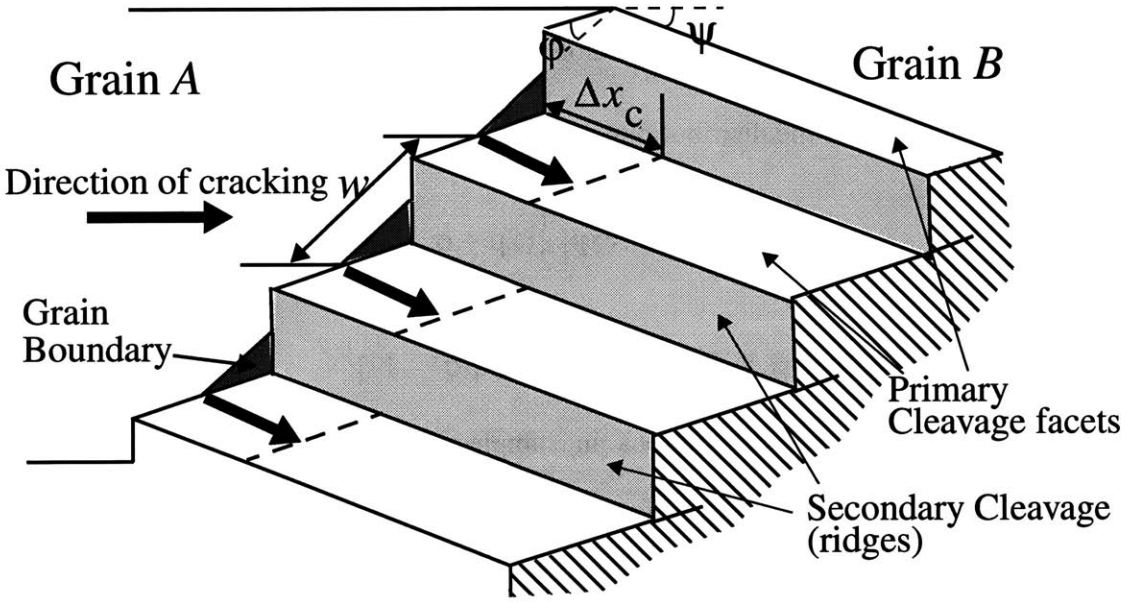

Fig. 2-11 break-through of a cleavage crack across a grain boundary.

Since the distances *w* between the break-through points along a grain boundary on the cleavage plane of grain *A*, were judged to be an important dimension in assessing the penetration resistance of a grain boundary to cleavage cracks, the number distribution of the distances *w* was measured for three separate grain boundaries.

These boundaries, identified as 13, 14 and 10, had systematically increasing angles of twist misorientations. Figures 2-12(a-c) show these distributions of w spacings between break-through points along the cleavage crack. All three distributions show rather similar shapes which fitted reasonably well to a log-normal distribution function $p(x)$ given as:

$$p(x) = \frac{1}{\sqrt{2\pi}\sigma x}\exp\left(-\frac{(\ln x - \mu)^2}{2\sigma^2}\right) \tag{2-9}$$

for $x>0$, where $x = w/w_0$ represents a normalized length parameter, and the parameters σ and μ govern the shape of the distribution function, with $w_0 = 1.0 \times 10^{-6}$m. The mean value $\bar{x}$ and the standard deviation s of the distributions are given by

$$\bar{x} = \exp\left[\frac{1}{2}(2\mu + \sigma^2)\right] \tag{2-10}$$

$$s = [\exp(2\mu + \sigma)^2(\exp\sigma^2 - 1)]^{1/2} \tag{2-11}$$

Specific evaluations of the distributions in samples 13 and 10 gave a peak value of the distribution in the range of roughly 2.5-3.0μm for both sample 13 (σ = 0.36; μ = 1.17; $\bar{w}$ = 3.47μm; s = 2.76 μm) and for sample 10 (σ = 0.16; μ = 1.63; $\bar{w}$ = 5.18μm; s = 4.12μm). The detailed examination of the ordering of these distances of break-through along the three individual boundaries, showed no important spatial clustering. There were no clear correlations between the distances w and the lattice twist misorientation angle, contrary to what might have been suspected. From these observations we conclude that the selection of the points of break-through by a cleavage crack along a grain boundary appears to be a random process, with the spacing w possibly depending only on a grain boundary structural feature. Figure 2-13 shows an

example of an "irregular" penetration mode of the cleavage crack across the grain boundary in the bi-crystal sample 13. In this case the cleavage crack has encountered the grain boundary first in a restricted region, and has penetrated across the boundary in a less regular form of entry points. As indicated by the river markings in grain *B*, the cleavage crack has then swung around and returned from grain *B* back to grain *A*, as depicted in Fig.2-14.

2.9.3 Fractures across grain boundaries above the cleavage to mixed-cleavage transition

Fractographic observations of cleavage transition from grain *A* to grain *B* indicated very similar features with, however, a significant difference in the appearance of the cleavage fracture surface of grain *B*, shown in Fig. 2-15. The cleavage facets in grain *B* are produced in a very similar manner as depicted in the sketch of Fig. 2-11. There is, however, considerable undercutting at the overlap regions of the primary cleavage strips. Instead of the formation of secondary cleavage-like fracture facets, bridging the primary strips, the ligaments between strips have undergone considerable sigmoidal plastic bending as depicted in the sketch of Fig. 2-16 where the cleavage strips are viewed from grain *B* toward grain *A*. This suggests that a significant portion of the additional fracture work in the mixed-cleavage plateau does not occur at penetration of the grain boundary, but immediately *subsequent* to it, affecting the fracture work of grain *B* all along its length, but requiring a substantial initial increase in the rate of production of fracture work at the critical stage of breakthrough. These various fracture surface features encountered in the bi-crystal penetration experiment have been found in abundance in the transition of cleavage cracks across grain boundaries in coarse-grained polycrystalline samples of Fe-2%Si alloy.

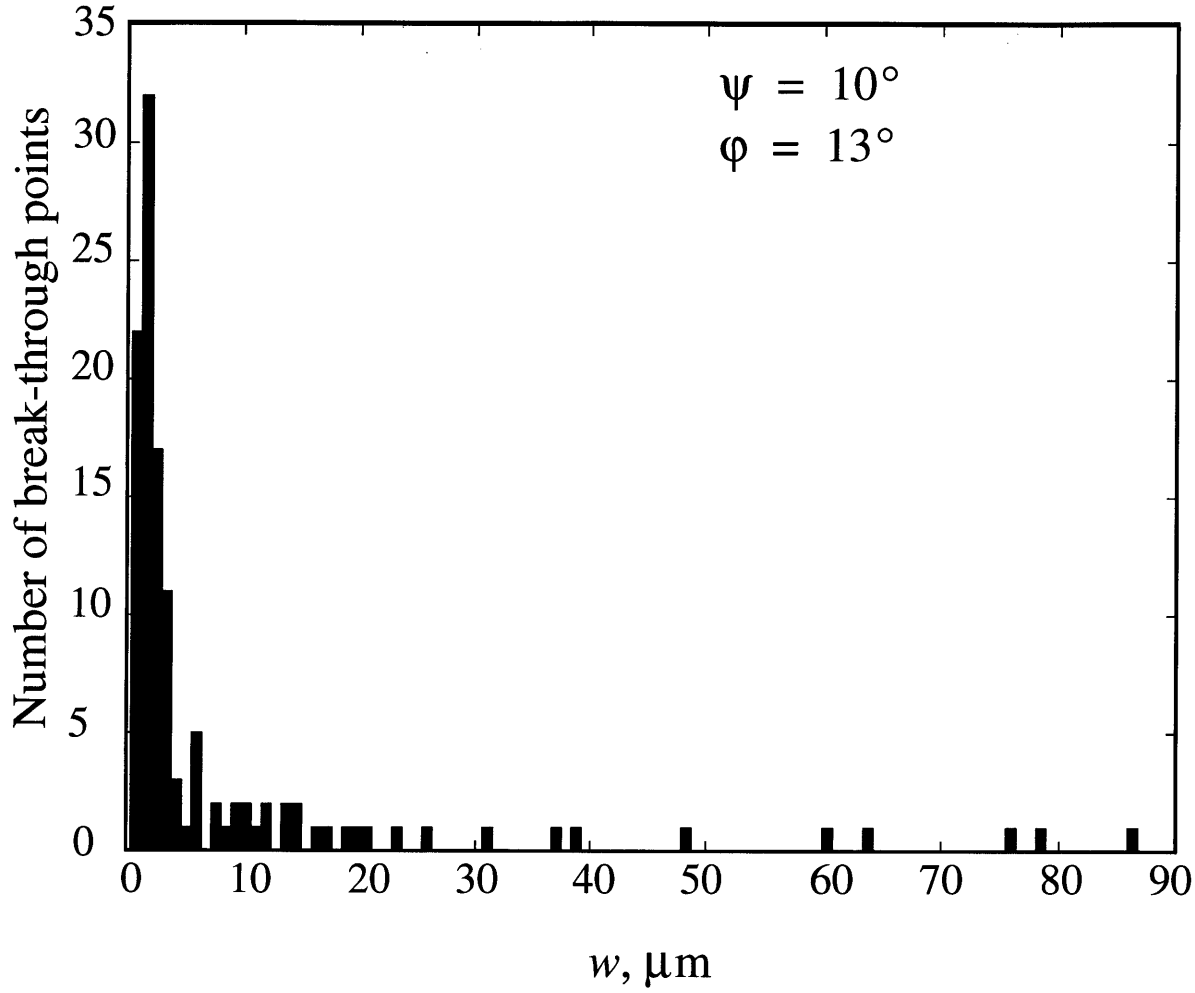
ψ = 10°
φ = 13°
Number of break-through points
0
5
10
15
20
25
30
35
0
10
20
30
40
50
60
70
80
90
w, μm

(a)

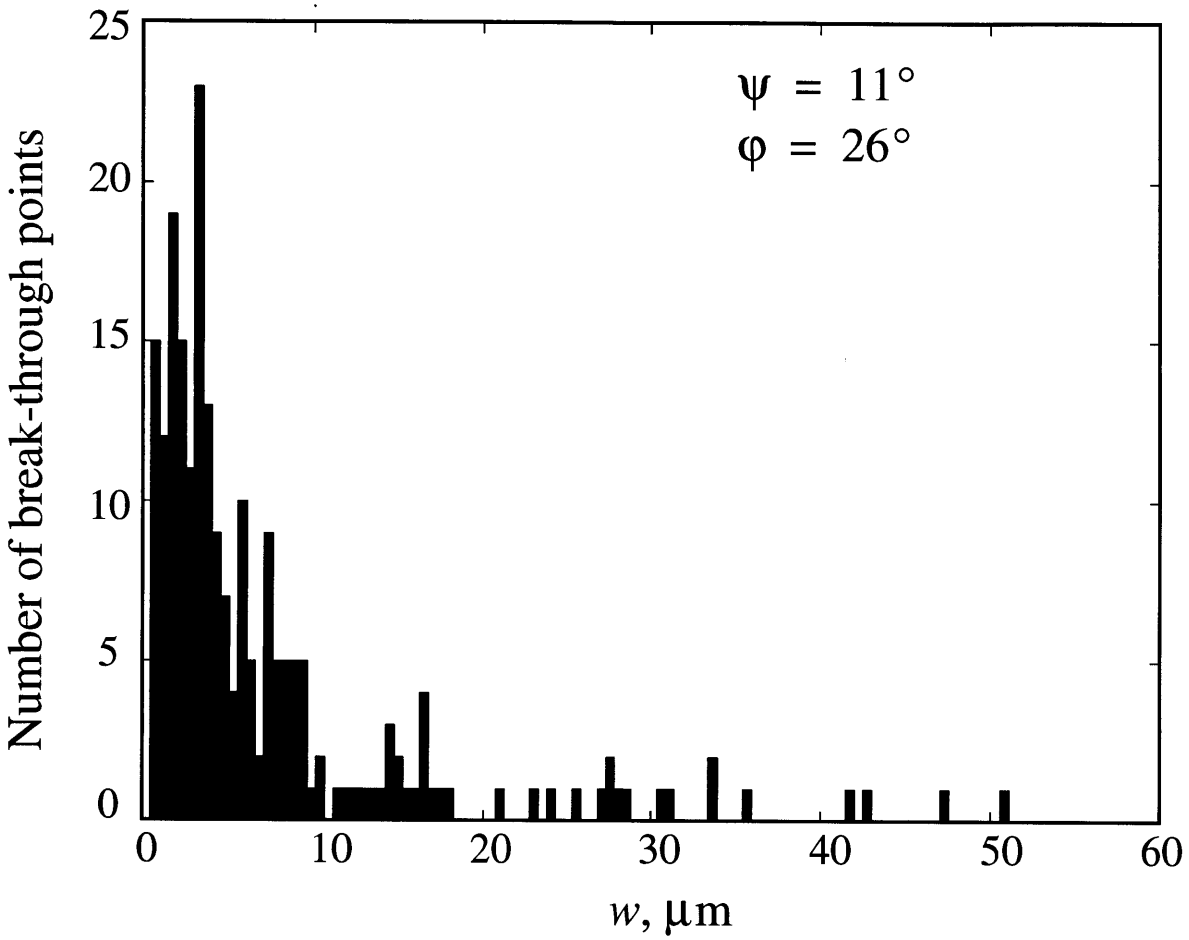
Number of break-through points
25
20
15
10
5
0
ψ = 11°
φ = 26°
0
10
20
30
40
50
60
w, μm

(b)

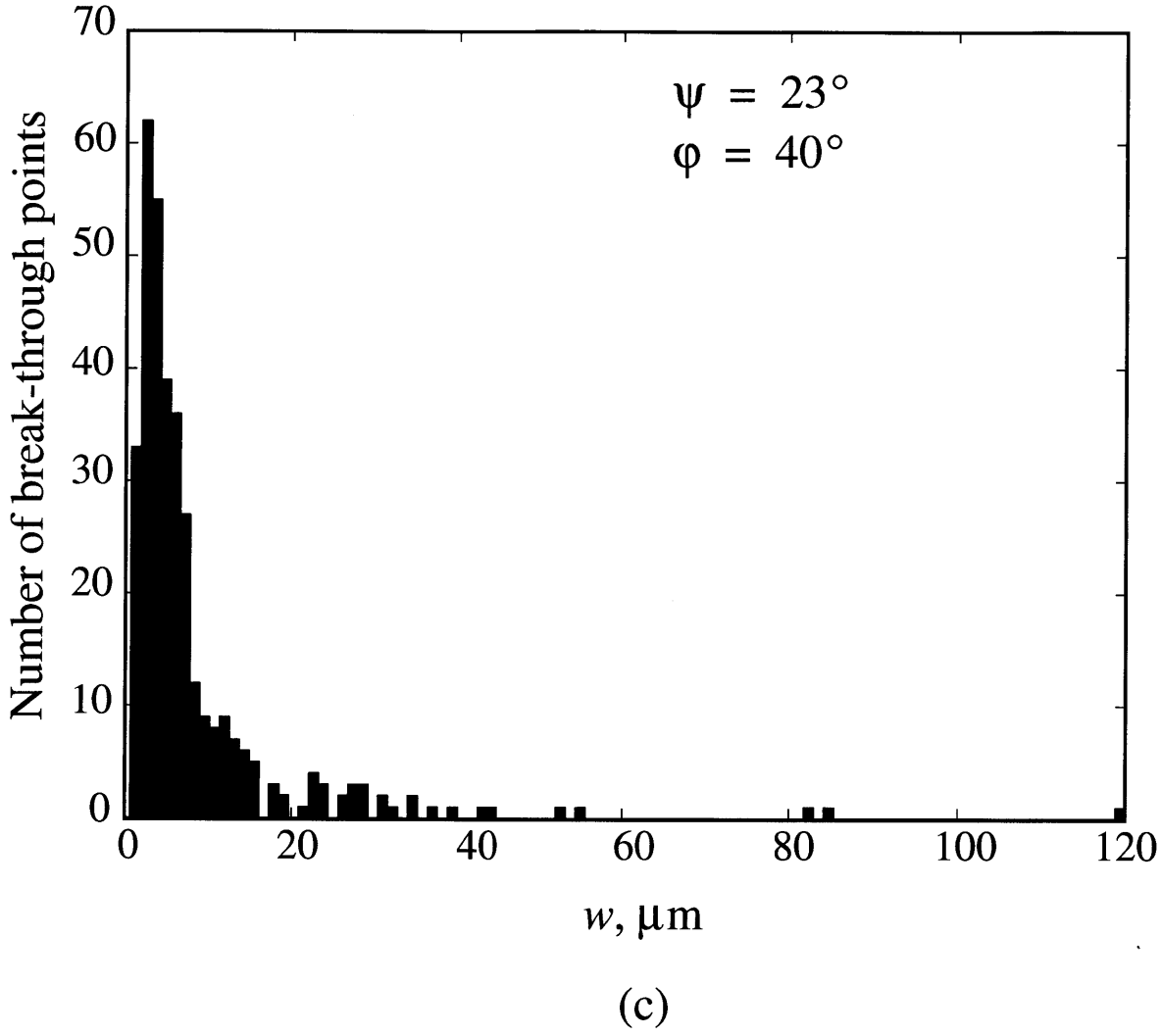

Fig. 2-12 Three specific determinations of the frequency distributions of the cleavage strip widths "*w*" in: (a) specimen 13; ($\psi = 10^{o}$, $\varphi = 13^{o}$); (b) specimen 14; ($\psi = 11^{o}$, $\varphi = 26^{o}$); (c) specimen 10; ($\psi = 23^{o}$, $\varphi = 20^{o}$).

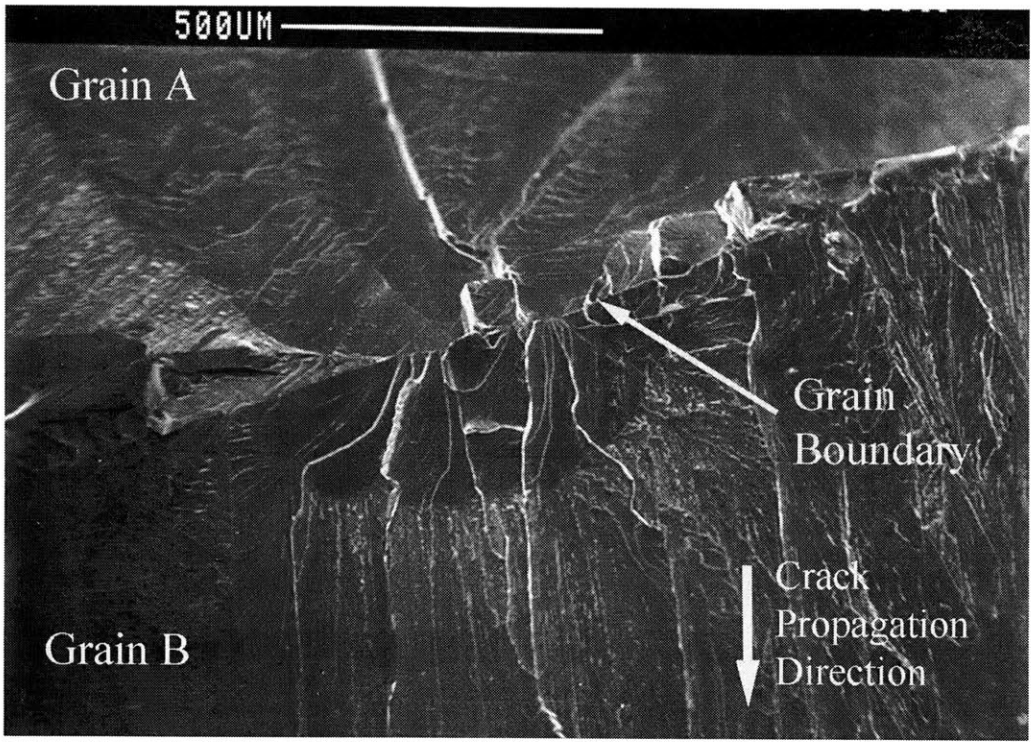

Fig. 2-13 SEM micrograph showing a case of an "irregular" mode of more localized break-through across a grain boundary.

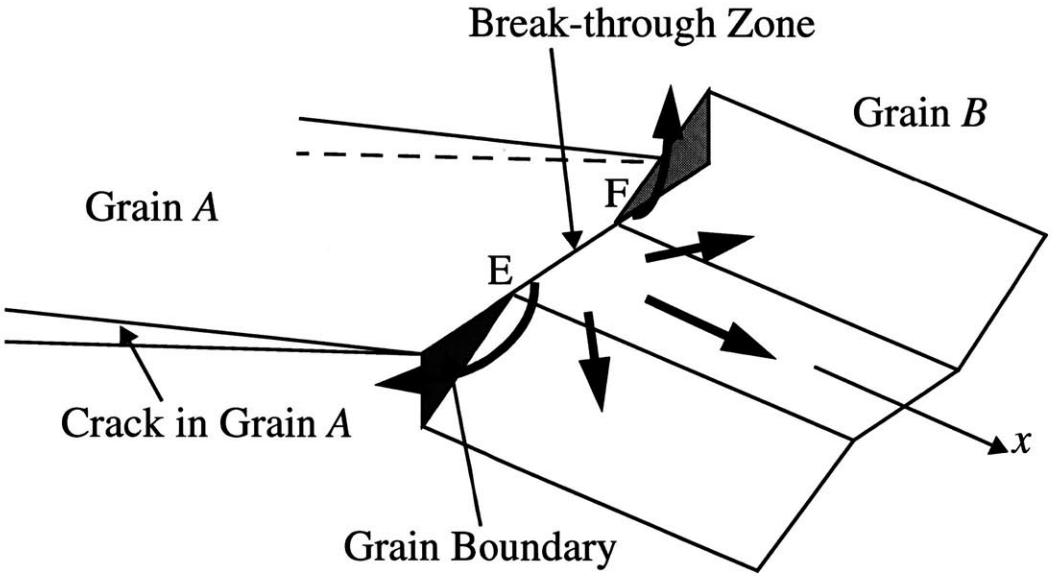

Fig. 2-14 Schematic showing an occasionally encountered case of local break-through of a grain boundary into grain *B* followed by return of the cleavage crack from grain *B* back into grain *A*.

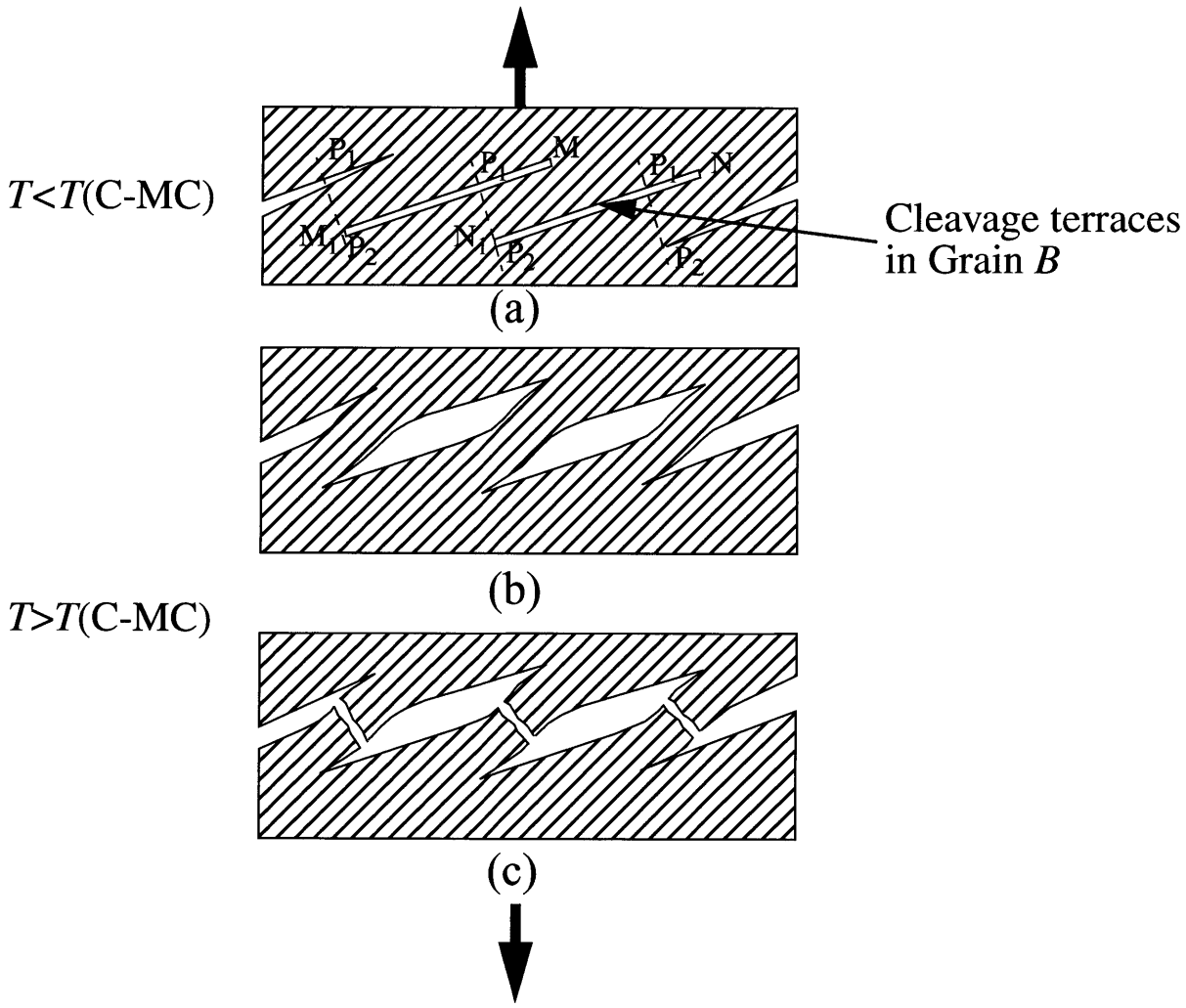

Fig. 2-16 Schematic depicting the connecting secondary cleavages between parallel cleavage strips in grain *B* below the cleavage-to-mixed cleavage transition, and (b) and (c) above the c-to-mc transition with the sigmoidal plastic bending and rupture of connecting ligaments, as viewed from grain *B* toward grain *A*.

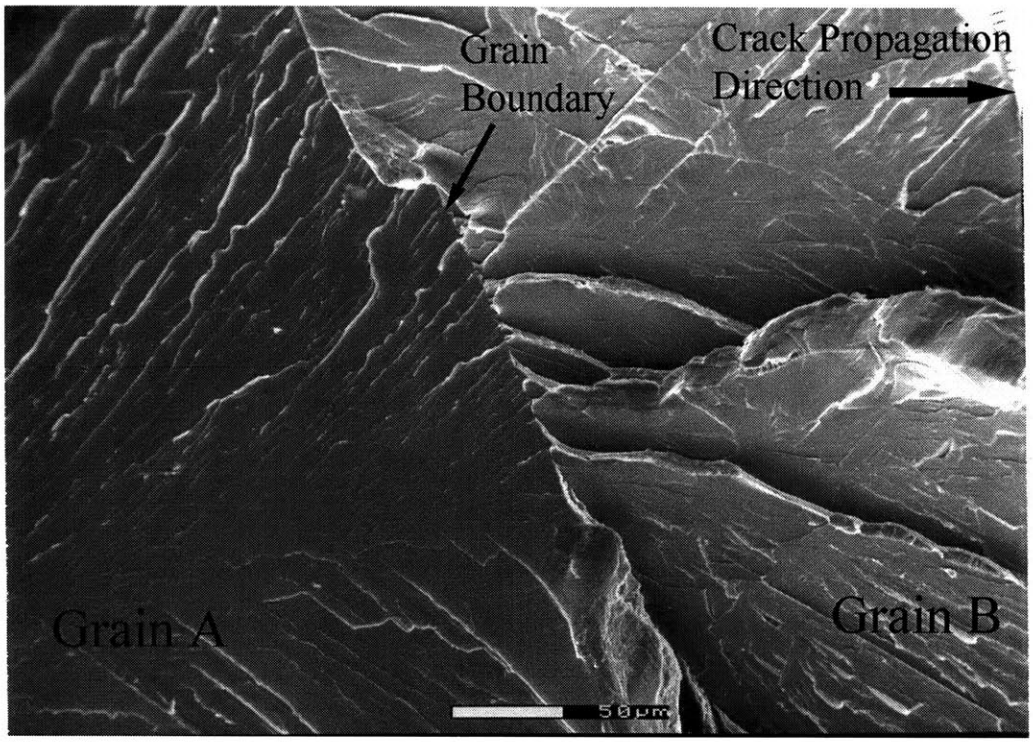

Fig. 2-15 SEM micrograph showing "undercutting" between adjacent cleavage strips, followed by sigmoidal plastic bending of connecting ligaments in grain *B* accounting for the increase in the break-through fracture work above the cleavage-to-mixed cleavage transition.

CHAPTER 3

CLEAVAGE CRACK PROPAGATION IN POLYCRYSTALLINE Fe-2%Si ALLOY

3.1 Materials

For the present investigation of the forms of brittle crack propagation across a field of grains in polycrystals, two complementary materials were selected. One was a very coarse-grained (in the range of 4mm) Fe-2%Si alloy to complement the previous investigation of the fracture resistance of individual grain boundaries discussed in Chapter 2. The other was a fine-grained decarburized 1010 steel of roughly 50μm grain size. The Fe-2%Si alloy was provided in square pieces cut from hot-rolled plates manufactured by Armco Metals of Middlefield, Ohio, with a thickness of approximately 26mm, and lateral dimensions of about 30 by 30cm. The material came from a batch used in an investigation on hot working of metals by Brown, et al. (1989)[1]. In the as-received material, there were small carbides of a size below 5 microns. To avoid undesirable interactions of such carbides with the cleavage crack propagation in the matrix, the material was annealed and decarburized according to a stringent schedule (Birks, 1969; Thelning, 1984) that had been used also in the earlier studies of bi-crystal Fe-3%Si alloy introduced in Chapter 2. The decarburization schedule consisted of first breaking-down the carbides by a prolonged period of 60 hours of soaking the alloy at 1400C in a pure nitrogen environment followed, without interruption, by a holding time of 2.5 hours at 1200C in a hydrogen environment, and ending up with a slow furnace cool to prevent entrapment of, and enbrittlement with, hydrogen. After the decarbur-

1. I am grateful to Professor Anand for making this material available to us.

ization, no carbides could be observed on fracture surfaces by SEM. The Vickers hardness of this material after the decarburization was 226 kg/mm^2. As already stated, the grain size of this alloy was quite coarse, in the range from 3mm to 10mm, with a few grains being as large as 30-50mm. Based on the visual examination of low temperature fracture surfaces of individual grains, which will be described in detail in Section 3.4 below, the orientation of grains appeared reasonably random. The chemical composition of the Fe-2%Si is given in Table 3.1.

Table 3.1 Chemical composition of the Fe-2%Si alloy

Element	C	Si	Al	Mn	Cu	Cr	Ni	Mo
Content(%wt)	<0.1	1.98	0.56	0.16	0.26	0.13	0.14	0.038

3.2 Specimen preparation

Compact fracture toughness tests (ASTM standard E399) were performed on the decarburized Fe-2%Si alloy. Standard fracture specimens were machined from the material, having dimensions of width w = 63.5mm, thickness b = 20.3mm, height $h = 1.2w$ = 76.2mm and initial crack length, a_0, in the range of about 39mm. All samples were pre-fatigued to produce well-characterized sharp initial pre-cracks.

The decarburized 1010 steel specimens were machined into double-edge cracked plate (DECP) shapes, of width w = 19.1mm, thickness b = 4.0mm, and initial crack length a_0 = 2.5mm. The edge cracks were electrical discharge machined (EDM) in the mid plane of the gauge area by using a 0.1mm copper EDM wire. The machined specimens were annealed for 2 hours at 600C.

3.3 Testing procedures

The fracture tests on the compact fracture toughness specimens of Fe-2%Si and DECP specimens of the decarburized 1010 steel were carried out on a Type 5508 Instron machine with a Type 319-007 environmental chamber. The specimens were tested at temperatures ranging from –30C to as high as 350C. For the high-temperature experiments, the environmental chamber was filled with dry nitrogen gas to prevent oxidization of the fracture surfaces. During the experiments, loads and load-point-displacements were measured and recorded continuously through the machine load cell and the LVDT of the Instron machine. For the compact fracture toughness tests of Fe-2%Si alloy, the temperature range covered the entire set of phenomena of pure-cleavage to a transition to mixed-cleavage behavior around 0C, to the conventional brittle-to-ductile transition temperature at around 250C and beyond up to 350C.

For the fracture tests on the DECP specimens of decarburized 1010 steel, to reach the lowest possible temperature, a cryogenically rated solenoid valve controlled by an Omega JK12 controller was installed in the piping system of liquid nitrogen to control the low temperature nitrogen gas flow into the chamber responding to the feedback signals from the thermocouple directly attached to the specimen surface. For these lowest temperature tests the commercial temperature controlling system of the chamber was deactivated. Temperature uniformity in the DECP specimens was reached typically within 15 minutes. However, as already stated above, due to the very low carbon content in the decarburized 1010 steel and the absence of other hardening agents, even at the

lower limit of –150C of this special environmental chamber the fracture behavior of the material remained above its brittle-to-ductile transition temperature.

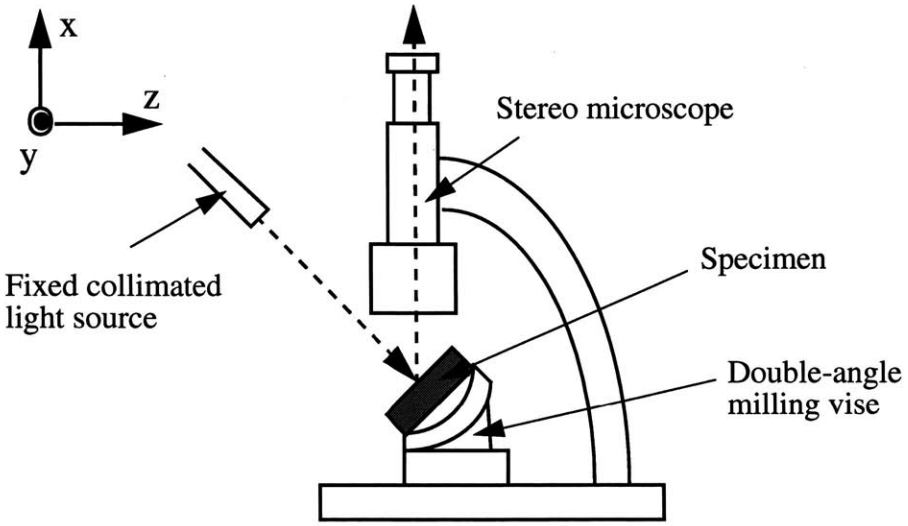

Fig.3-1 Sketch of the modified stereo microscope for determination of inclination of cleavage planes in individual grains relative to sample reference surfaces.

3.4 Methods of fracture surface characterization

To study the forms of interaction between propagating cleavage cracks and grain boundaries, fracture surfaces across the field of fractured grains of three of the Fe-2%Si specimens were characterized in detail. For this purpose a special device was produced to measure the tilt and twist orientation of cleavage fracture surfaces of each individual grain with respect to the lateral specimen surface and the expected median geometrical plane of the desired crack propagation. The device is shown in Fig.3-1. The stage of a stereo microscope was replaced by a double-angle vise

having a base capable of rotating 360° about a vertical axis (x) and able to incline from horizontal by 45° up or down about an axis (y), with attached goniometers permitting the rotation angles to be measured to within ±0.5 °. A parallel light source was fixed on the frame of the stereo microscope as shown in the figure. The system was first calibrated by means of a mirror placed in such a position as to reflect the light from the light source into the microscope tube along its optic axis. Then the mirror was replaced by the fractured specimen to be characterized. By rotating the vise along the x- and y- axes, the position of the specimen was adjusted so that cleavage facets of each individual grain reflected the light into the microscope. In this way the tilt and twist angles for each grain in the fracture field relative to the external specimen axes could be measured and recorded. The relative tilt and twist angles between individual grains across their common grain boundaries could then be readily calculated from this information, as discussed in Chapter 7. The cleavage facet in each grain was of [100] type.

Through viewing the cleavage surfaces of each grain of the fractured coarse-grained Fe-2%Si alloy, the break-through patterns and river markings could be determined to establish in each case the grain boundary which was penetrated-through first by the propagating cleavage crack. The results were reported as fracture propagation maps to be presented in Chapter 7.

3.5 Temperature dependence of plastic resistances

Since the brittle-to-ductile transition behavior of metals and alloys, particularly the two iron-based materials Fe-2%Si and the decarburized 1010 steel, is governed primarily by the temperature-dependence of their plastic resistance, this information was established first. Figure 3-2

shows the results for these two materials. The information on the Fe-2%Si alloy was obtained by re-scaling the corresponding information of the Fe-3%Si alloy reported in Chapter 2. The re-scaling was accomplished on the basis of the ratio of the Vickers hardiness of these two alloys at room temperature. The information on the decarburized 1010 steel was developed through direct determination of the stress-strain behavior of this material in tension experiments carried out at different temperatures, in the same environmental chamber discussed above.

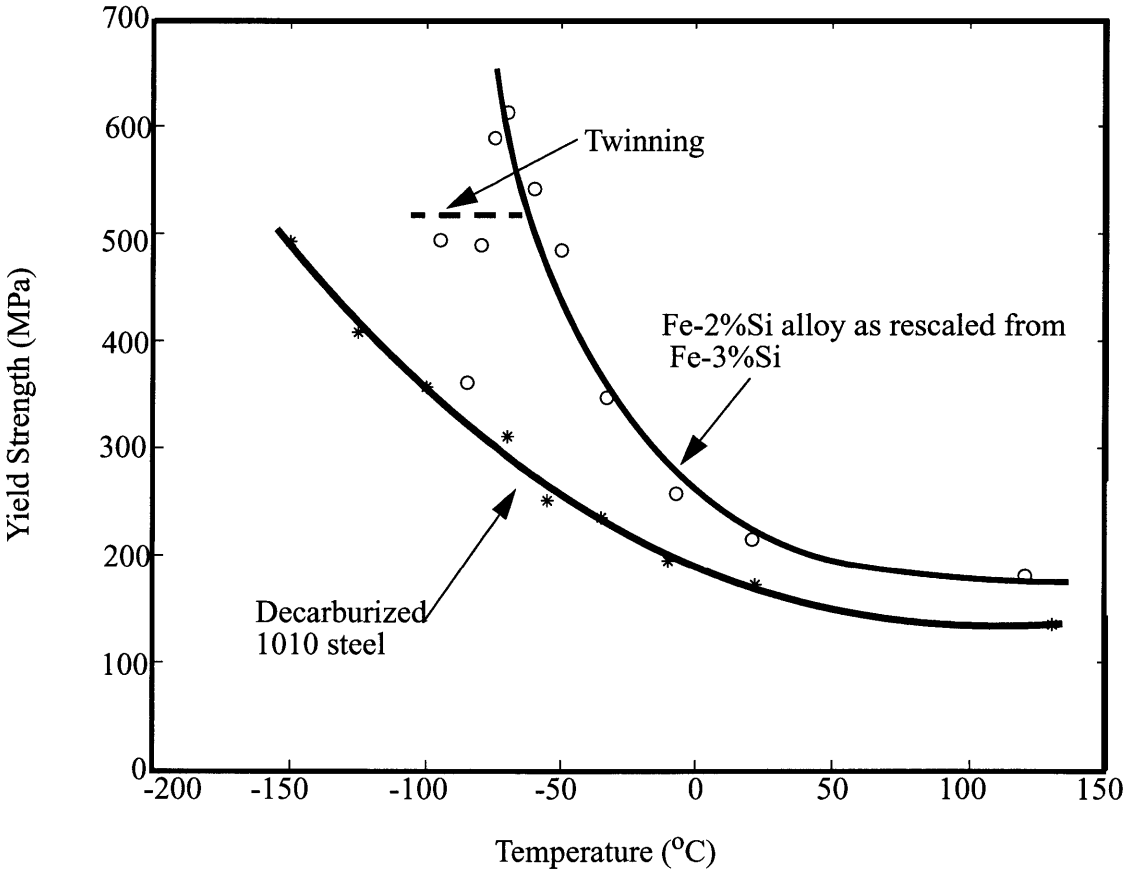

Fig.3-2 Temperature dependence of tensile yield stresses in Fe-2%Si alloy (as scaled from data on Fe-3%Si single crystals) and decarburized 1010 steel.

Figure 3-2 shows that the expected brittle-to-ductile transition temperature of the two materials will be radically different, based primarily on the temperature-dependence of their plastic resis-

tances, as we will amplify further in Chapter 7. The horizontal dotted line related to the curve for the Fe-2%Si alloy, together with the possible large scatter at low temperatures, results from the widespread twinning in the single crystals of the Fe-3%Si alloy tested in a multiple slip orientation that was reported in the previous study. From that study it is also known that the temperature-dependent yield stress curve and the corresponding fracture stress curve come together at around 680MPa and -60C, indicating that under these conditions yielding and fracture are simultaneous. From this we estimate the brittle strength of the Fe-3%Si alloy to be 680MPa and assume that this magnitude should also be close to the brittle strength of the very coarse grained Fe-2%Si alloy of interest to us here. Noting that the average grain size of the Fe-2%Si alloy samples was around 4mm and that of the 1010 steel was around 50 microns, and that the brittle strength should scale inversely with the square root of the grain size, we estimate the brittle strength of the decarburized 1010 steel to be well above 1.0GPa.

Parenthetically, we note that after decarburization, to a 0.05 wt% C it is improper to refer to the decarburized 1010 steel as a *steel*. It should best be referred to as "commercial purity iron". Nevertheless, because of its original designation we will continue to refer to it as decarburized 1010 steel.

3.6 Compact fracture experiments on the Fe-2%Si alloy

Figure 3-3 shows the dependence on temperature of the measured K_{IC} fracture toughness of the Fe-2%Si alloy. The figure clearly shows two kinds of fracture work transition, one at around 0C and the other at around 250C. The one involving the small change in fracture work, at 0C, was

identified to be the pure-cleavage to mixed-cleavage (PC/MC) transition reported in Chapter 2 in the experiment of fracture resistance of individual bi-crystals in Fe-3%Si alloy. There, it was found that below the transition temperature, when a cleavage crack breaks through a grain bound-

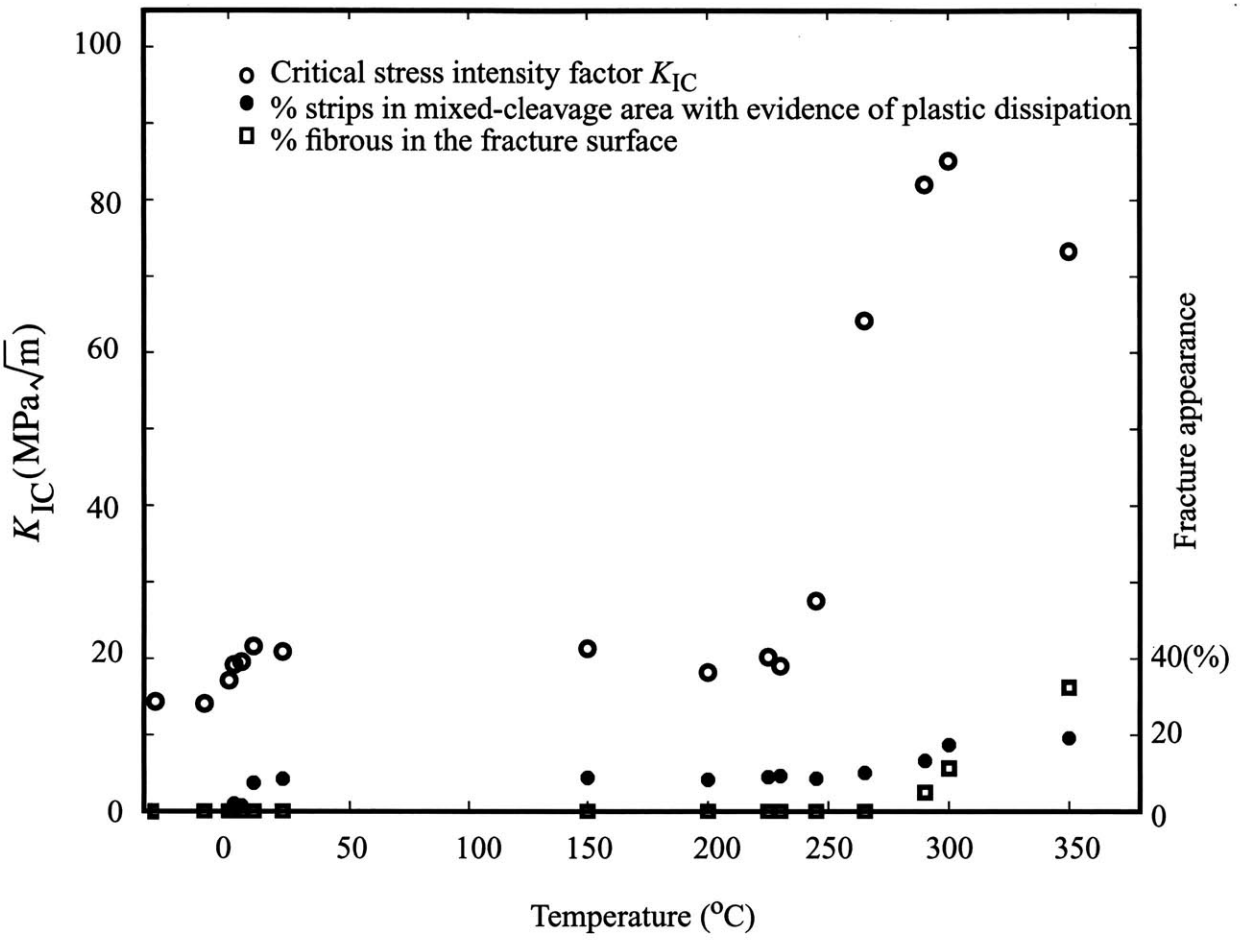

Fig.3-3 Temperature dependence of the fracture toughness, K_{IC}, and fracture appearance in coarse-grained Fe-2%Si alloy.

ary into a neighboring grain, the break-through occurs at roughly evenly-spaced "gates" and forms a tiered cleavage surface in the adjoining grain, resulting in a set of quasi-regularly spaced cleavage strips resembling a staircase, with the descent angle of the staircase being governed primarily by the twist misorientation of cleavage planes across the boundary. In the transit of the cleavage crack across the grain boundary in the pure cleavage (PC) range, below the transition

temperature, the peak cracking resistance is governed by the rate of increase with respect to crack advance of: a) primarily the additional cleavage surface production in the adjoining grain; and b) secondarily, the increase in plastic shearing work at the grain boundary along the cleavage steps. Above the PC/MC transition, the geometrical features of the transit of the cleavage crack appear nearly identical to those below the fracture transition. However, additional plastic work is involved in sigmoidal plastic bending of ligaments between the cleavage strips in the adjoining grain before the ligaments are eventually severed by cleavage or by a cleavage-like separation, with the additional plastic bending of the ligaments accounting for the increment in fracture work, over and above that in the pure cleavage range below the fracture transition. The changing appearance of the fracture surfaces with temperature is shown in Fig.3-3 in the form of percent of fibrous fracture.

Figure 3-4 shows a SEM micrograph of the fracture surface below the PC/MC transition in the present studies, with two grain boundaries that have been traversed. Figure 3-5 shows a representative area of the fracture surface above the PC/MC transition, where, in addition to the cleavage surfaces of the tiered fracture in grains, noted in the bi-crystal study, now appearing as well-delineated river markings, a coarser form of undercutting of adjoining cleavage processes near grain boundaries is visible, associated with plastic bending of a coarser set of ligaments. The appearance of the fracture surfaces remains substantially unchanged from that shown in Fig.3-5 between the PC/MC transition temperature and the traditional BD transition around 250C. Figure 3-6 shows a prominent example of fracture of a remaining coarse ligament between two substantially offset cleavage strips inside a grain in the MC range, where the mutual undercutting of the cleavage processes was followed by considerable sigmoidal plastic bending before eventually a com-

plex and jagged cleavage-like fracture process severed the ligament. Another source of quite substantial fracture work, over and above the average fracture work of cracks traversing grain boundaries, is that which is involved when a small fraction of "recalcitrant" grain boundaries of large misorientation eventually give way with a very complex ductile shearing and tearing process, after the main fracture front across grains has gone around them and left them behind. An example of the tearing-apart of such a recalcitrant grain boundary is shown in Fig.3-7.

Figure 3-3 shows considerable scatter in the measured K_{IC} results in the plateau region between the two fracture transitions. This is a direct result of the very coarse grain size in the alloy, making variations between different compact fracture samples large. These variations are less a result of variation of average grain size, but are rather due to the very small number of grains across the critical fracture front where the crack started growing unstably. Thus, between different fracture samples there are large variations in the number of grains across the thickness along the critical fracture front and their respective twist and tilt misorientations between grains along the front. These discrete events and how the main crack percolates through the field of grains is discussed in more detail below in Chapter 7.

Finally, Fig.3-8 shows a region of the fracture surface immediately above the BD transition temperature with a mixture of ductile dimple type separation and continued cleavage type separation. In fact this feature of a strong persistence of terminal cleavage fracture among ductile dimple type fracture remained up to 350C, well above the BD transition, and reflected the strong tendency to cleavage of grains in this upper shelf behavior, even after considerable plastic flow in this solid solution strengthened alloy.

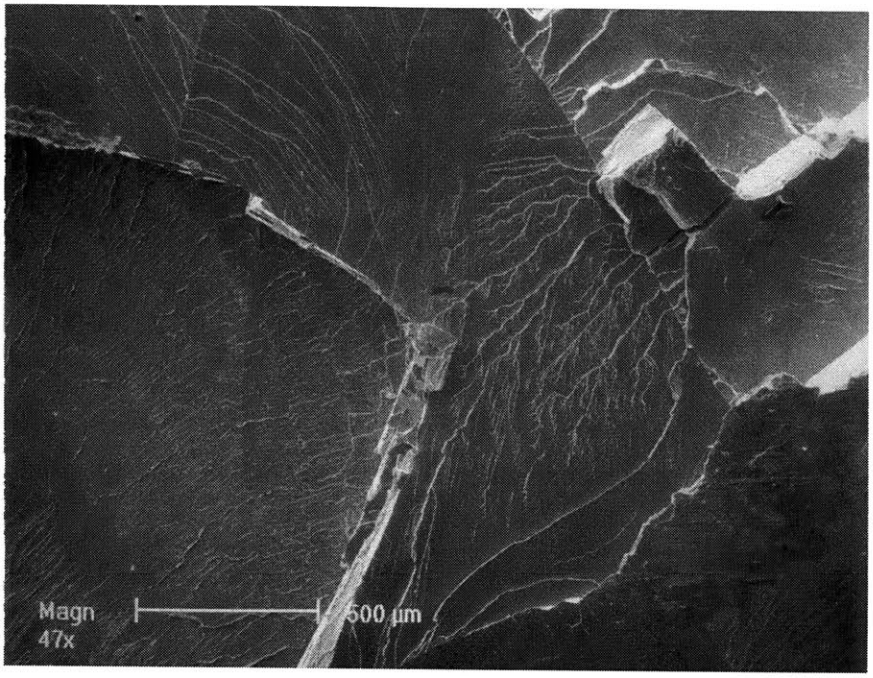

Fig.3-4 SEM micrograph of fracture surface of Fe-2%Si below the PC/MC transition at -30C.

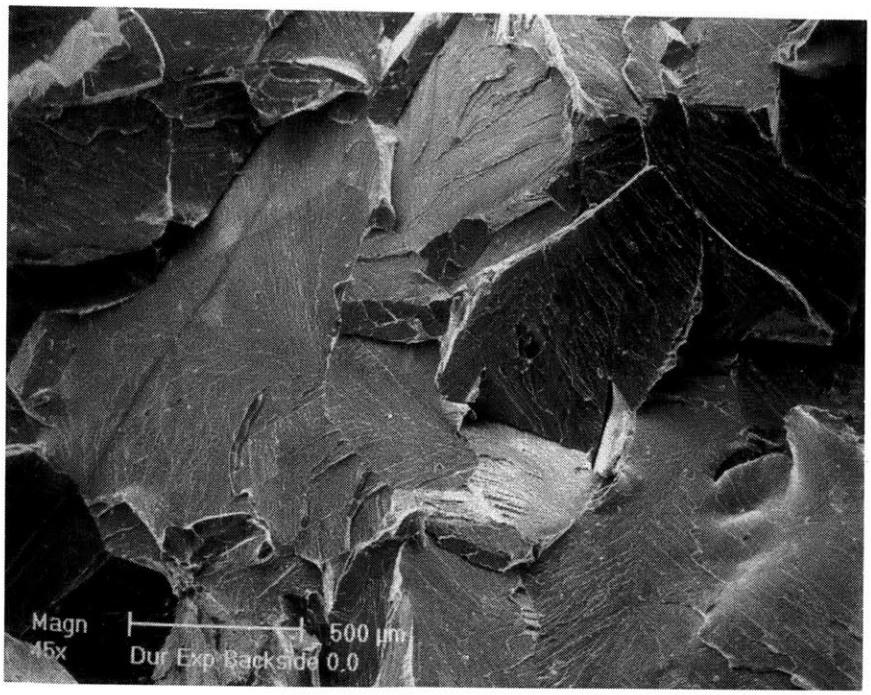

Fig.3-5 SEM micrograph of fracture surface of Fe-2%Si above the PC/MC transition at 20C.

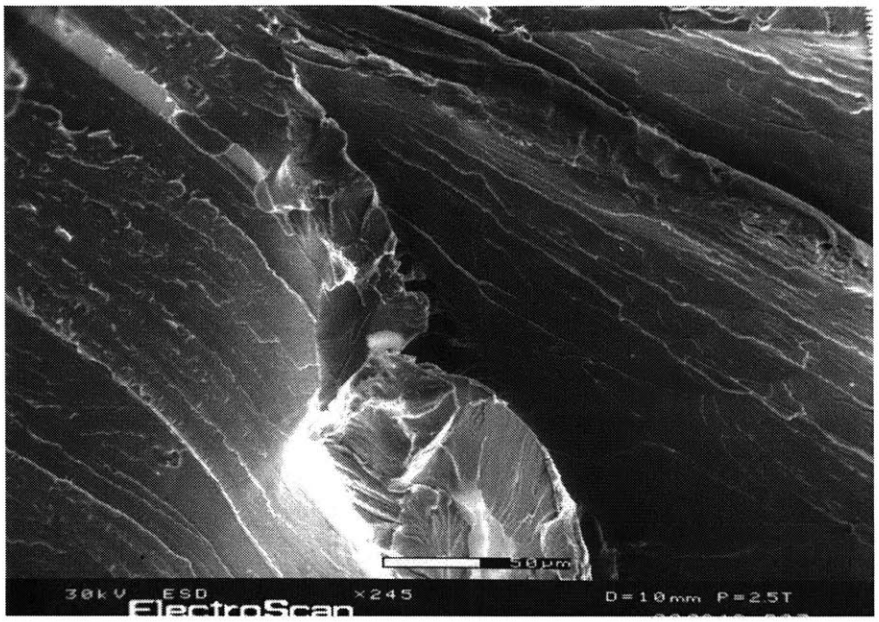

Fig.3-6 SEM micrograph of a complex bridging fracture between two parallel cleavage facets inside a grain in Fe-2%Si alloy (22°C).

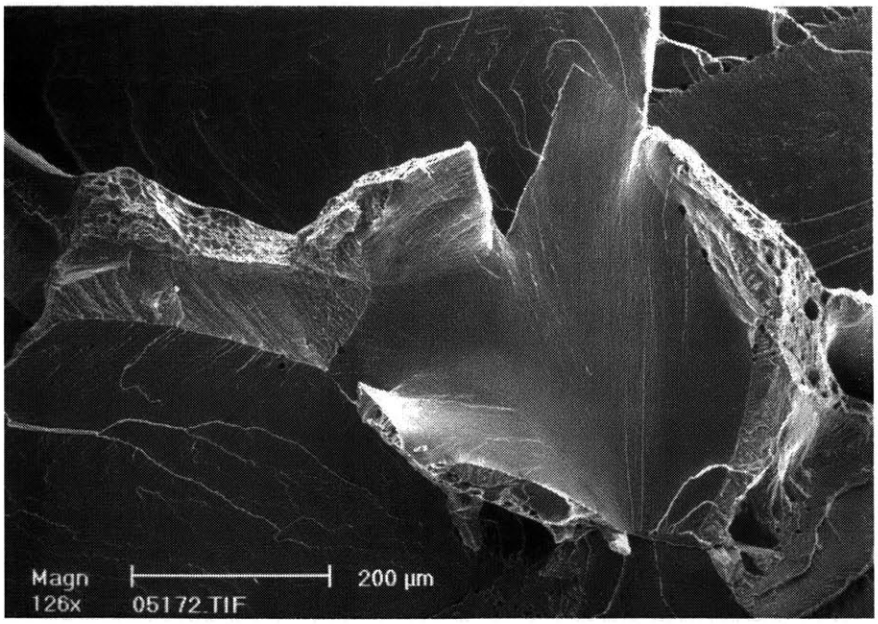

Fig.3-7 SEM micrograph of a complex fracture along a recalcitrant grain boundary in Fe-2%Si alloy at -30C.

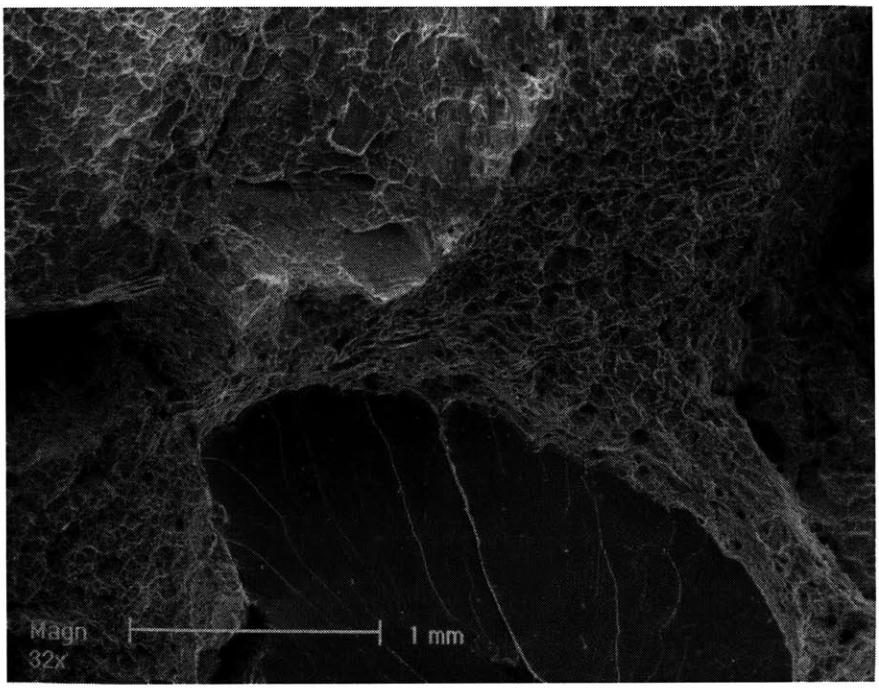

Fig.3-8 SEM micrograph of fracture surface immediately above the conventional brittle-to-ductile transition at around 250C in Fe-2%Si alloy, showing areas of clear ductile dimple fracture and cleavage fracture.

3.7 Fracture experiments on the decarburized 1010 steel

The temperature dependence of the fracture toughness of the decarburized 1010 steel is given in Fig. 3-9. Because of the low plastic resistance of this material, the fracture resistance as determined from the DECP samples is given by the *plane stress* J-integral value, J_C (although it is difficult to get really plane stress conditions in DECP specimen), according to well established procedure (Kumar, et al. 1981). Clearly, in the temperature range between –150C and 150C the material is well above its conventional brittle-to-ductile transition temperature indicated by the level of the measured J_C values. The micrograph of Fig.3-9 of the fracture surface at -100C shows an area of ductile dimple type separation among cracked grains. Nevertheless, on the whole, as Fig.3-9 indicates, the fracture surface appearance is nearly completely of cleavage type and remains so up to -50C. This is more clearly demonstrated by the fractography of Figs.3-11a, b and c showing representative fracture surfaces at -125C, -70C, and -40C. This upper shelf cleavage response is indicative of the intrinsically brittle nature of Fe where a terminal cleavage mode of separation can still occur after substantial plastic work, and signals a possibility of a troubling tendency to overall terminal brittle behavior in large structures.

The *plane stress* fracture toughness values J_C referred in Fig.3-10 in the entire temperature range of -150C to 150C are quite large, primarily because of the low plastic resistance of the material devoid of any significant hardening agent and the elevated brittle strength, estimated to be around 1.0GPa, based on the moderately small grain size. This has made the DECP sample configuration with the grain dimensions used in this study, more in the nature of a stubby tension

specimen, rather than a fracture toughness specimen. Nevertheless, the behavior represented in Fig.3-9 is that of a very tough, material in the near-cryogenic temperature range. We discuss this behavior further in Chapter 7 in comparison with the behavior of the Fe-2%Si alloy.

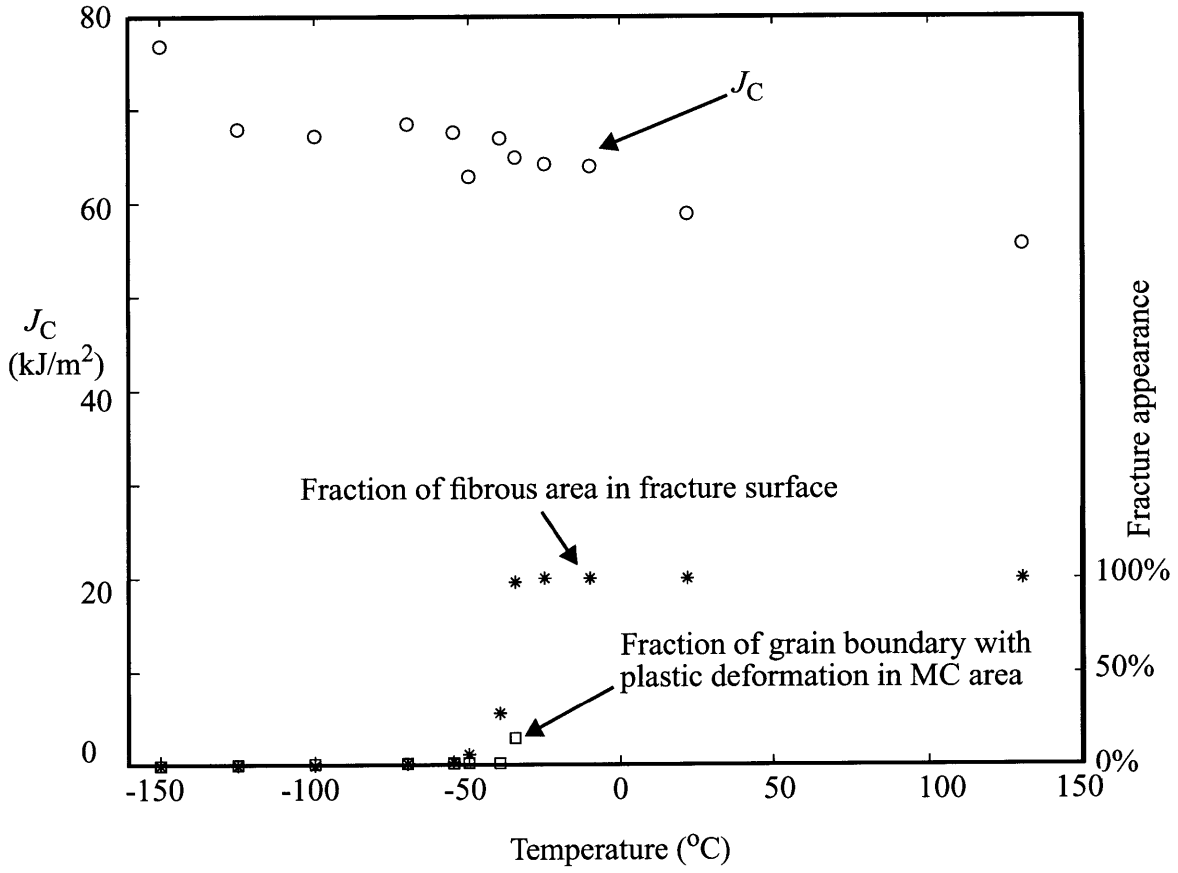

Fig.3-10 Temperature dependence of J_{IC} plane stress fracture toughness in DECP specimens of decarburized 1010 steel showing the persistence of terminal cleavage fracture above the brittle-to-ductile transition in the upper shelf region.

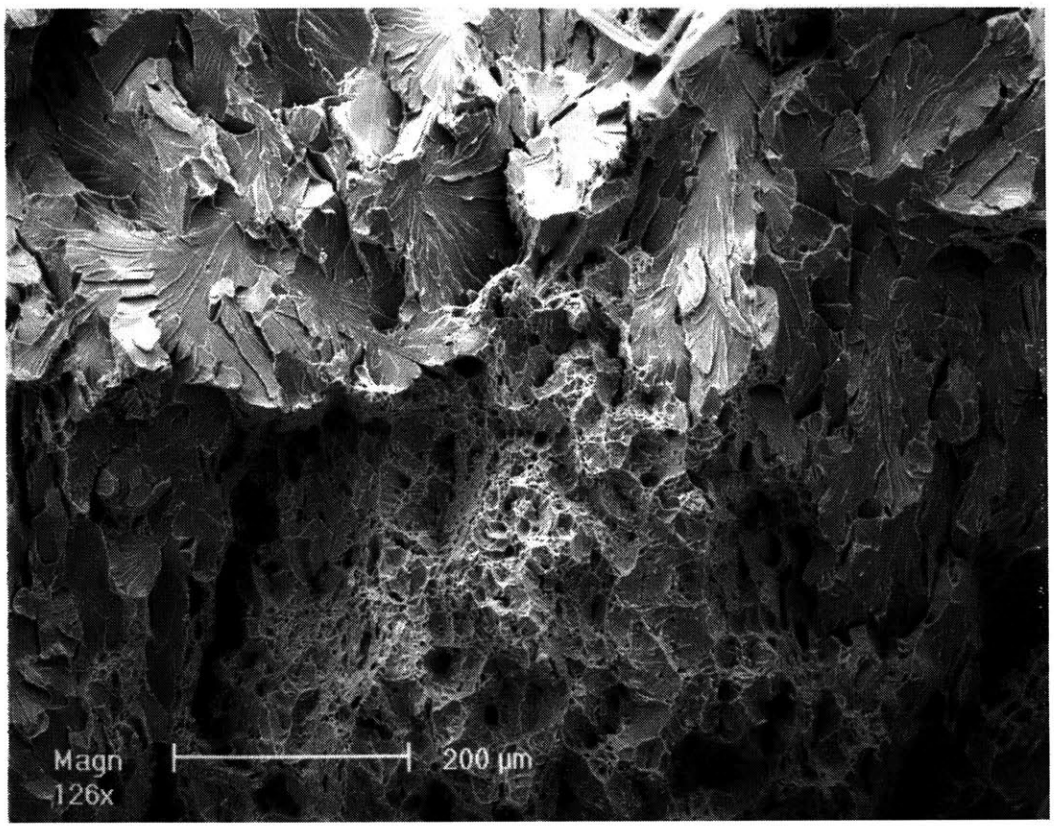

Fig.3-9 Fracture surface of decarburized 1010 steel at -100C, well above its brittle-to-ductile transition temperature, showing a mixture of cleavage and ductile dimple fracture.

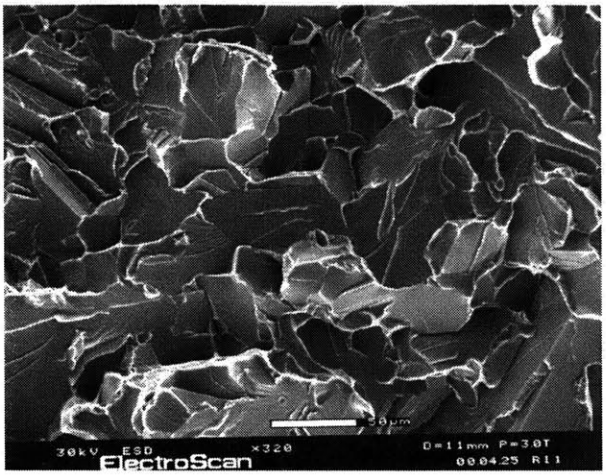

(a)

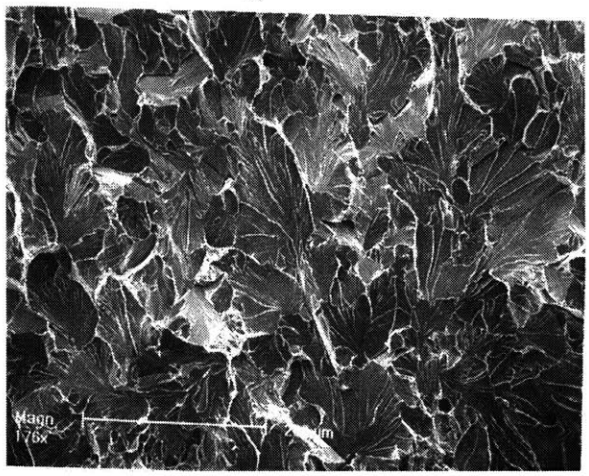

(b)

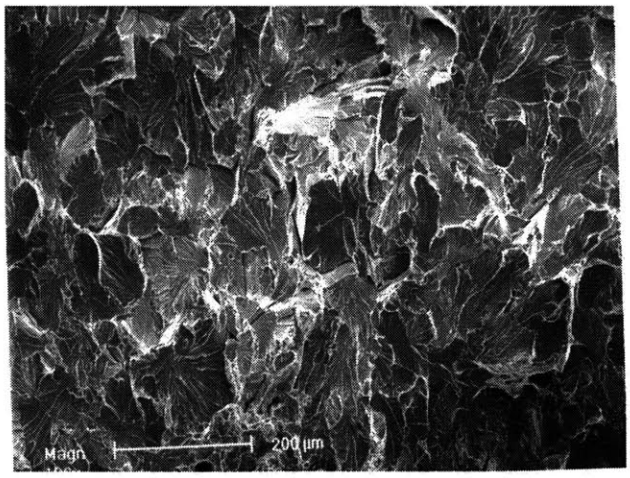

(c)

Fig.3-11 A sequence of SEM micrographs of fracture surfaces in decarburized 1010 steel: a) at -125C; b) at -70C; and c) at -40C.

CHAPTER 4

THERMAL CRACK ARREST EXPERIMENTS IN SINGLE CRYSTALS OF FE-3%SI ALLOY

4.1 Material and Specimen Preparation

To study the brittle-to-ductile transition in Fe-3%Si alloy single crystals, we carried out thermal crack arrest experiments. The material studied in the experiments was extracted from large single crystals of Fe-3%Si alloy provided by the Allegheny-Ludlum Steel Co, but was not from the same batch as the ingots used in bi-crystal experiments in Chapter 2. By using an electrical-discharge machine (EDM), two sets of slabs with the length of 100mm, the width of 10mm, and the thickness of 4mm were cut from those single crystals. The 100×10 and 100×4 surfaces of both sets of slabs were parallel to (100) crystal planes, while in the first set of slabs, the direction along the 100mm edge was parallel to the <100> direction and in the second set it was parallel to the <110> direction. The crystal orientation was determined before EDM cutting and double-checked afterwards by the Laue back reflection method.

The carbon content of the as-received material was relatively high, and equi-axed carbides with the size of several microns could be observed on polished surfaces. To avoid the influence of carbides on crack propagation, the extracted single-crystal Fe-3%Si slabs were decarburized in an environmental tube furnace and subsequently subjected to a heat treatment schedule similar to that for the bi-crystal specimens discussed in Chapter 2. This treatment consisted of soaking for

30 hours at 1400C in pure nitrogen to break down carbides and dissolve the carbon into the background, followed by exposure to a dynamic hydrogen environment at 1200C for about 2 hours to remove the carbon. After decarburization, the carbon content was less than 0.01% by weight, and the silicon content was unaffected at 3.61% by weight. The spectral analysis was performed by Galbraith Laboratory, in Knoxville, TN.

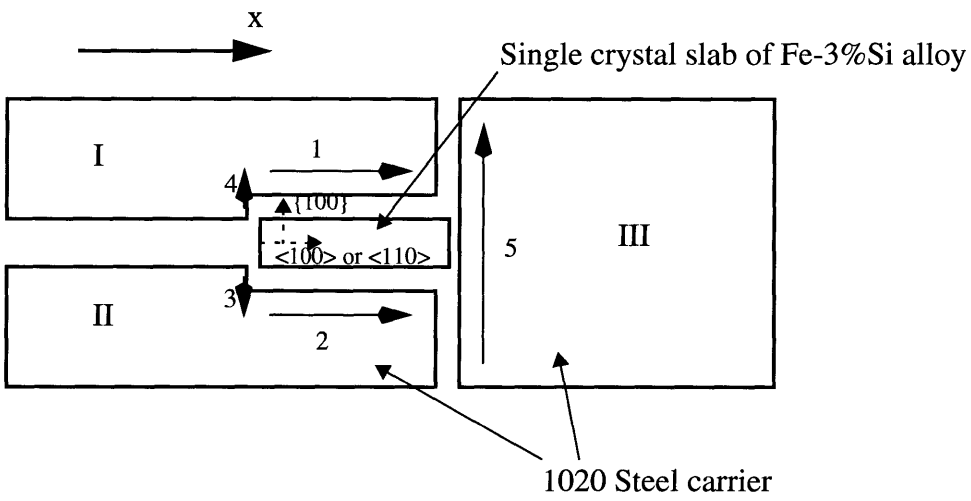

Fig.4-1 Schematic diagram of the electron-beam welding process. The arrows and the numbers denote the directions and the order of welding paths.

Double cantilever beam (DCB) specimens were fabricated by electron-beam welding the decarburized Fe-3%Si single crystal slabs into 1020 steel carriers. The welding paths and schedules are shown in Fig.4-1. They were designed to minimize residual stresses. The gap between the two DCB arms became the main part of the pre-crack. It can be seen that, in the DCB specimen, the (100) plane of the single crystal slab was always parallel to the median plane of the specimen, and, depending on which set of slabs was used, the axis parallel to the x-direction could be either <100> (group A specimens) or <110> (group B specimens). The E-

beam welded specimens were annealed at 250C in a nitrogen environment for 2 hours to reduce residual stresses.

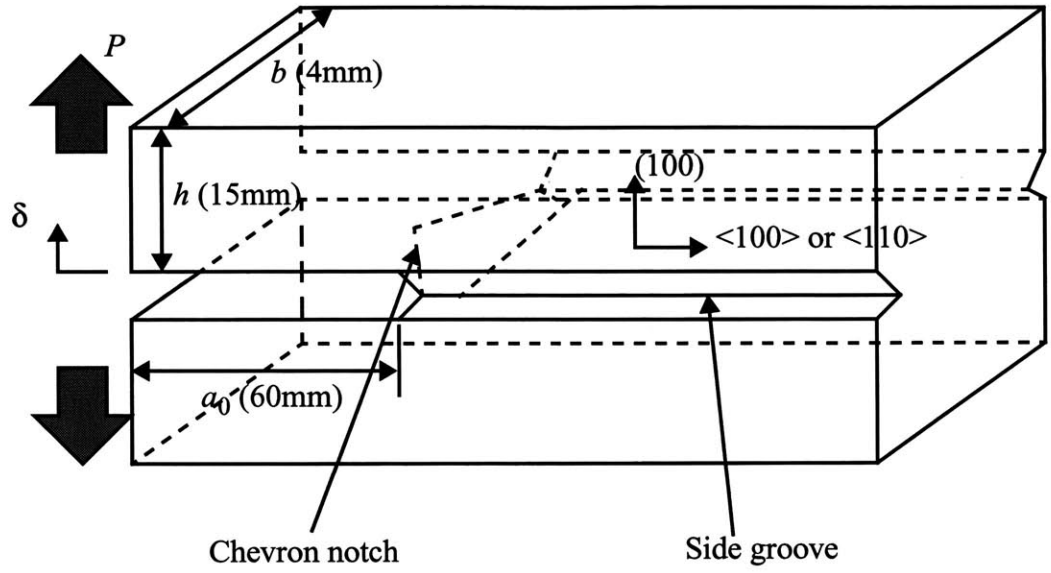

Fig.4-2 A schematic diagram of DCB specimen

Chevron notches of 45° angle were cut by EDM at the root of the precrack to help to initiate a sharp cleavage cracking process in the experiments. Shallow 60° side grooves were cut along the x-direction (see Fig.4-1) in the median plane of the specimen by using a double-edged carbide cutter. The remaining thickness across the two roots of side grooves was around 3mm, about 75% of the original specimen thickness.

To make the crack growth in the DCB specimen as stable as possible, the compliance of the specimen should be much larger than that of the loading machine (Gally, 1999), which necessitates large crack length and narrow DCB arms. However, the geometry of the environmental chamber set an upper limit to the crack length to be about 60mm. Accordingly, we chose the height of the DCB arm, *h*, as 15mm, the smallest value that could avoid plastic

bending of the DCB arms before the crack was thermally arrested. Figure 4-2 shows a schematic diagram of a final DCB specimen.

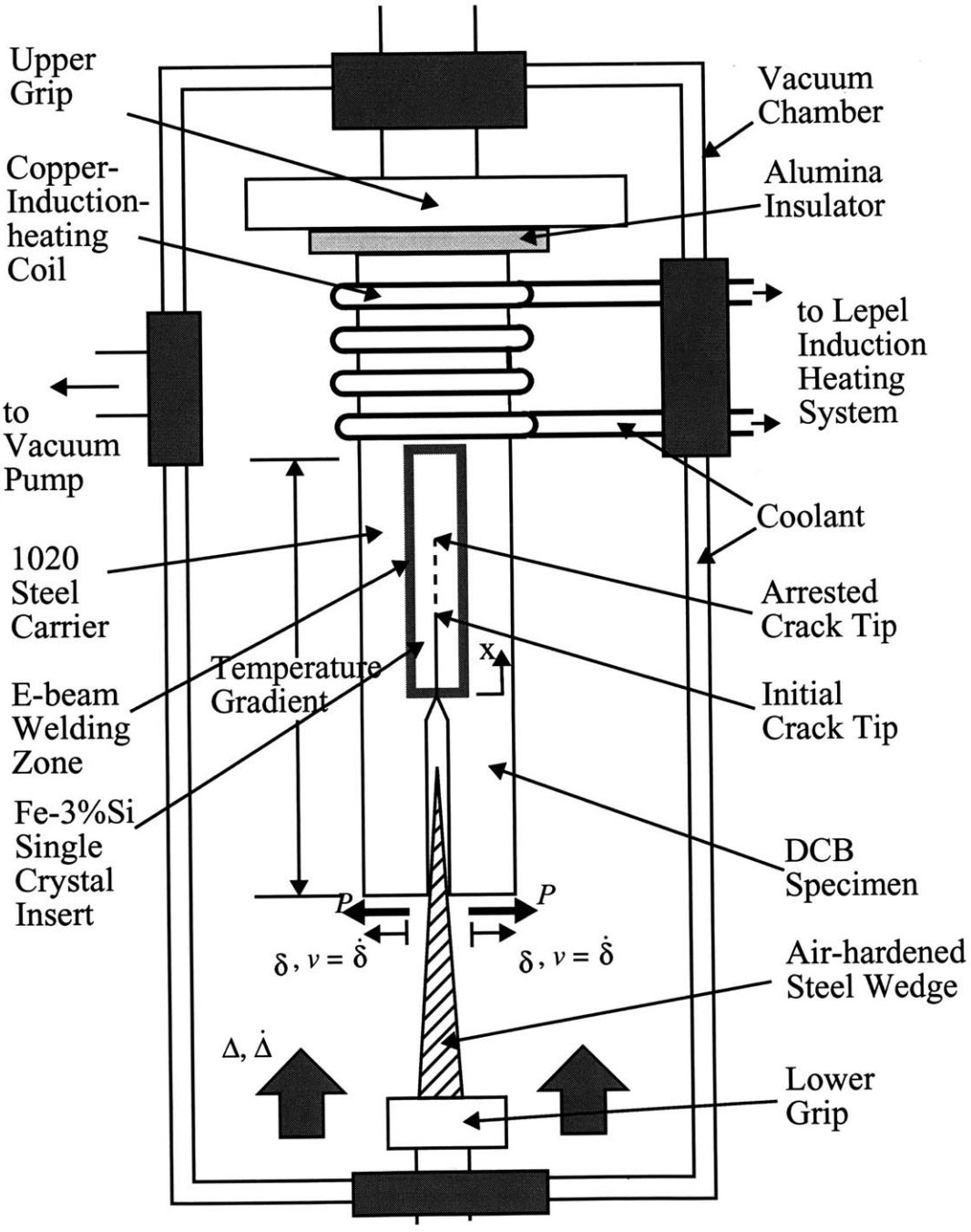

Fig.4-3 Experimental Set-up for thermal crack arrest experiments in Fe-3%Si single crystals

4.2 Temperature Gradients along Specimens

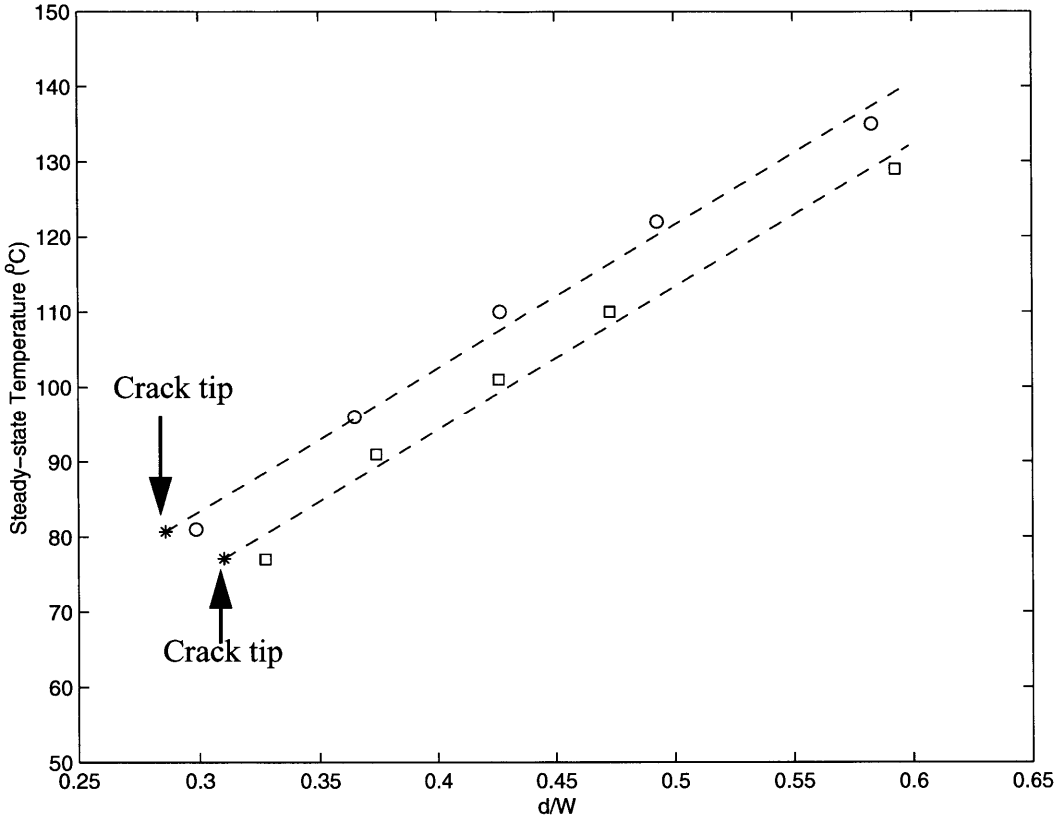

Fig.4-4 Temperature gradients along x-axis in two different DCB specimens, where *d* is the distance from the thermocouple to the end of the specimen, and *W* is the total length of the specimen.

Figure 4-3 shows the experimental set-up schematically. The experiments were carried out on a reconfigured type 1350 Instron machine with a sealed Centorr vacuum chamber. To thermally arrest a crack propagating in the median plane of the DCB specimen along the x-axis, a type T-254-225 Lepel induction heating system was used to produce a temperature gradient. The specimen was immersed, upside-down, into the water cooled copper induction-heating coil covered with a glass fiber sleeve, which kept the specimen and the copper coil electrically

isolated. The copper coil was connected to the Lepel system. During the experiment, the induction heating coils operating at 60Hz produced by induction heating in the upper part of the specimen a rapid temperature rise, resulting in a temperature gradient along the x-axis between the crack tip and the end of the specimen. The tubular copper coil and the wall of the environmental chamber were water-cooled by a type III Neslab closed liquid circulation system that kept the temperature of the coil and the chamber close to room temperature. Throughout the experiment the pressure inside the environmental chamber was kept below 10^{-6} Torr to prevent oxidation of the specimen and possible convection to adversely affect the temperature gradient. The specimen was insulated from the chamber by an alumina plate; therefore the steel wedge contacting the specimen and the lower actuator at room temperature became the only heat sink. The alumina insulator also helped to isolate the induction coil from the load cell. Typically, the steady state temperature gradient along the x-axis could be achieved in 30 minutes.

In the experiment, the temperature at the upper end of the specimen was kept below 200C. Based on thermal conduction alone, at steady-state, the temperature gradient should be constant. This was found to be the case. The temperature gradients in two different specimens measured by thermocouples directly attached on the single crystal slabs are shown in Fig.4-4. During the experiment, the input power of the Lepel system was carefully controlled such that the temperature at the upper end of the specimen was maintained around 150C-170C. The temperature at the lower end was measured to be around 80C. It will be shown below that the brittle-to-ductile transition (BDT) temperature of Fe-3%Si alloy single crystal was in the range from 100C to 130C under the applied loading rates. Thus, during the crack propagation from the low-temperature end to the high-temperature end, when the crack tip reached the place where the

local temperature equalled the BDT temperature, the crack was arrested due to a sharp increase of fracture resistance.

4.3 Experimental procedure

To perform the thermal crack arrest experiment, the lower grip of the Instron machine was moved upward with a constant speed to advance an air-hardened steel wedge with a wedge angle of 10^{o} between the two arms of the DCB specimen to force the crack to propagate. To minimize friction between the wedge and DCB arms, a layer of fine graphite powder had been sprayed on the wedge surfaces.

The dashed line in Fig. 4-5 shows the ideal reversible load-displacement curve for a smoothly growing crack. The load first increases linearly before the crack starts to propagate. The slope S_c of the initial loading curve, OA, is given by simple beam theory as:

$$S_c = \frac{1}{\tilde{C}_s} = \frac{P}{\delta} = \frac{Ebh^3}{8a^3} \tag{4-1}$$

where $\tilde{C}_s$ is the compliance of the specimen, E is the Young's modulus of the material, h and b are the arm height and the thickness of the DCB specimen, respectively, a is the crack length, P is the cracking opening load, and δ is the crack opening displacement (see Fig.4-3). The values of P and δ were calculated through the load measured by the load cell and the displacement of the wedge measured by LVDT through similar method discussed in Chapter 2. With increasing load, when the critical stress intensity factor is reached at the crack tip, the crack should start to grow stably along the x-axis under ideal conditions, and the load will decrease smoothly along

the curve A-B due to increasing specimen compliance. Through simple beam theory the functional form of curve A-B is

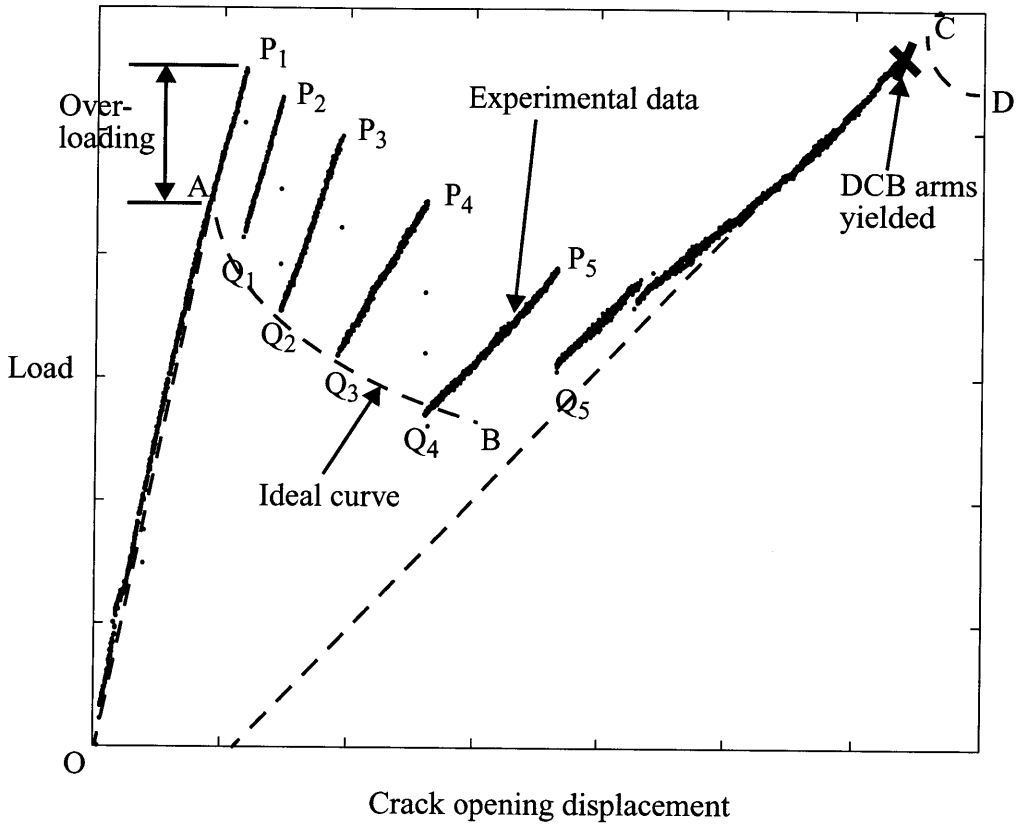

Fig.4-5 A typical load-displacement curve.

$$P = \tilde{A} G_{IC}^{\frac{3}{4}} / \delta^{\frac{1}{2}} \tag{4-2}$$

where $\tilde{A} = (Eh^3)^{\frac{1}{4}} \left(\frac{b}{8}\right) \left(\frac{16}{3}\right)^{\frac{3}{4}}$ is a constant of the DCB specimen, and G_{IC} is the critical energy release rate for brittle fracture in the single crystal at temperatures below the BDT temperature (where the temperature dependence of the Young's modulus has been ignored).

In Eqn.(4-2) it is assumed that the fracture resistance of the material remains constant at the lower shelf level. When the crack tip approaches the place where the local temperature equals the BDT, the crack is arrested because of the sharp increase of fracture resistance. Then, the load will increase linearly again upon continued insertion of the wedge into the DCB specimen, until the critical stress intensity factor at the upper shelf is reached. Then the crack could grow stably again, and the load would decrease smoothly along the curve C-D, under ideal quasi-static conditions given as:

$$P = \tilde{A}\bar{G}_{IC}^{\frac{3}{4}}/\delta^{\frac{1}{2}} \tag{4-3}$$

where $\bar{G}_{IC}$ would be the required energy release rate for an assumed ductile crack extension process of the single crystal Fe-3%Si alloy above BDT.

In the actual experiment to achieve close to ideal conditions the crack was sharpened first by propagating it in the pure cleavage mode by a certain distance at very low temperature. For this the specimen, clamped across the crack tightly in a vise, was immerged in liquid nitrogen. A standard brass block was then dropped on the wedge inserted into the DCB specimen to propagate the crack through the Chevron notch. Subsequent examination of the fracture surface showed that this procedure resulted in a very sharp crack tip. Nevertheless, in the actual experiments, even with such initial sharpening of the precrack tip, it was impossible to achieve stable crack growth, due to a variety of geometrical imperfections. The crack tip was always somewhat overloaded before it started to propagate. This resulted in jerky crack extension. The data points in Figure 4-5 show an experimental load - wedge displacement curve with such step-

Table 4.1 Experimental Results of K_{IC}

Specimen number*	Group	crack opening rate (mm/ sec.)	T_{BD} (°C)	Tempe-rature at cold end (°C)	Tempe-rature at upper end (°C)	The number of crack jumps	Original crack length (mm)	Length of each crack jump (mm) K_{ICa} (MPa*m$^{-1/2}$): K_{IC} for the crack to propagate K_{ICb} (MPa*m$^{-1/2}$): K_{IC} at arrest the crack
100c	A	0.042	130	74	172	5	52.3	Jump length:8.4;10.2;13.4;16.4;5.0 K_{ICa}: 7.6;6.8;8.2;8.0;9.1 ($\overline{K}_{ICa}$ = 7.9) K_{ICb}: --;5.4;5.8;5.7;6.7;7.6($\overline{K}_{ICb}$ = 6.2)
100f	A	0.042	111	94	174	2	51.8	Jump length: 5.6; 4.1 K_{ICa}: 9.0; 7.8 ($\overline{K}_{ICa}$ = 8.4) K_{ICb}: --; 7.2; 7.2 ($\overline{K}_{ICb}$ = 7.2)
100g	A	0.0028	106	83	143	3	55.4	Jump length: 4.5; 7.0; 8.6 K_{ICa}: 7.8; 6.4; 8.3 ($\overline{K}_{ICa}$ = 7.5) K_{ICb}: --; 6.1; 7.4; 7.0 ($\overline{K}_{ICb}$ = 6.8)
100h	A	0.0028	120	88	155	2	53.0	Jump length: 8.4; 18.1 K_{ICa}: 7.1; 8.3 ($\overline{K}_{ICa}$ = 7.7) K_{ICb}: --; 7.2; 6.8 ($\overline{K}_{ICb}$ = 7.0)
110e	B	0.040	124	97	177	2	53.7	Jump length: 13.6; 9.3 K_{ICa}: 6.0; 7.5 ($\overline{K}_{ICa}$ = 6.8) K_{ICb}: --; 5.7; 6.4 ($\overline{K}_{ICb}$ = 6.1)

* The thickness b and the height of DCB arm h of all the specimens are 4.0mm and 19.0mm, respectively.

wise crack advance involving 5 crack jumps, each resulting in clearly discernible increases in specimen compliance. After the final jump, the P-δ curve acquired a definite upward curvature, with the final slope giving a positive intercept on the displacement axis, indicative of some plastic crack opening. In the experiments, since the height of the DCB arms was chosen as small as possible, there was also always some plastic bending of the specimen arms.

After the crack had been thermally arrested, the actuator motion was reversed, resulting in some elastic reversal flexing of the arms backward, pushing the wedge out. Then, the induction heating system was turned off, the specimen was cooled slowly inside the vacuum chamber, and removed. Altogether, 4 successful experiments were performed for group A specimens with the <100> direction parallel to the x-axis and 1 for group B with the <110> direction parallel to the x-axis. Two different crack opening rates were used on group A specimens. The results are listed in Table 4.1.

4.4 Crack length measurement

After the thermal crack arrest experiment was over the specimens were immerged into liquid nitrogen and separated by impact loading of the wedge with a hammer to expose the fracture surfaces. Since this final separation occurred close to liquid nitrogen temperature, negligible accompanying plastic deformation was expected.

To calculate critical stress intensity factors from the jerky load-displacement curves, the crack length associated with each crack jump had to be obtained accurately. This could be either

calculated through the experimental load-displacement curves or measured directly from the exposed fracture surface. In practice, the crack length was first estimated through Eqn.(4-1), and then, checked by means of SEM examination of the areas close to the estimated crack arrest places and the pattern of re-initiated river markings. In this way, the crack lengths were measured quite accurately for each step. The measured results of crack jump lengths are listed in Table 4.1.

4.5 Berg-Barrett X-ray Topographic Imaging

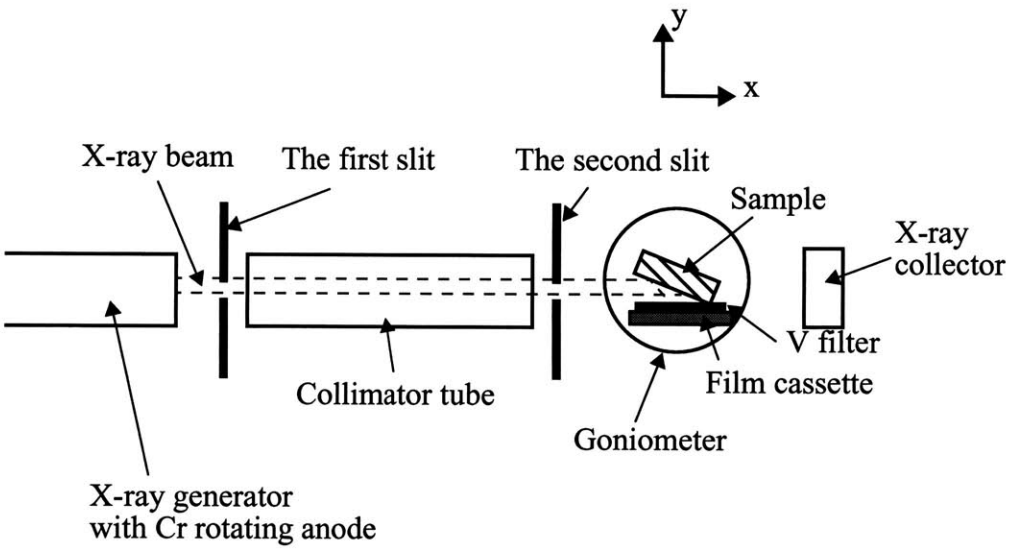

Fig.4-6 Schematic diagram of experimental set-up of Berg-Barrett equipment, as viewed from the top.

4.5.1 Experimental set-up

To reveal the dislocation patterns governing the brittle-to-ductile transition in the single crystals of Fe-3%Si, dislocation etch pitting was tried but proved to be unsuccessful due to the generally unreliable nature of the procedure, in Fe-3%Si aggravated by the relatively high roughness of fracture surfaces. Usually dislocation etching of the Fe-Si alloy was performed on eletropolished surfaces to produce dislocation pits (Stein and Low, 1960; Saka and Imura, 1972, 1973; Moon and Vreeland, 1968; Erickson, 1962). However, in our experiment to visualize dislocation structures at arrested crack fronts we could only study cleavage surfaces as produced. To remedy this difficulty we attempted Berg-Barrett x-ray topographic imaging of the fracture surfaces. Berg-Barrett x-ray topographic imaging is a method to record defect structure close to the surface of a near-perfect single crystal (Newkirk, 1959; Turner, Vreeland and Pope, 1968). As shown in Fig.4-6 schematically, a high-resolution film is placed very close to the single crystal and is exposed by reflected x-ray beam. If the crystal is perfect, the image on the film should be uniform darkness. If there are defects in the crystal, the defects would reinforce intensity of the reflected x-ray radiation and show up on the film as dark lines or spots.

The x-ray source used in the experiment was a type RU300 rotating anode Rigaku x-ray generator, equipped with a proper Cr anode giving a vertical line source and a reconfigurated enclosure to admit a type 1152 Rigaku Lang camera that was aligned with a 6^{o} angle to the normal of the shutter of the anode housing. The sample was placed on a goniometer in the center of the camera. There were two vertical slits on the two sides of the tubular collimator between the sample and the x-ray source, therefore the divergence of the incident x-ray beam was only of the order of few microradians.

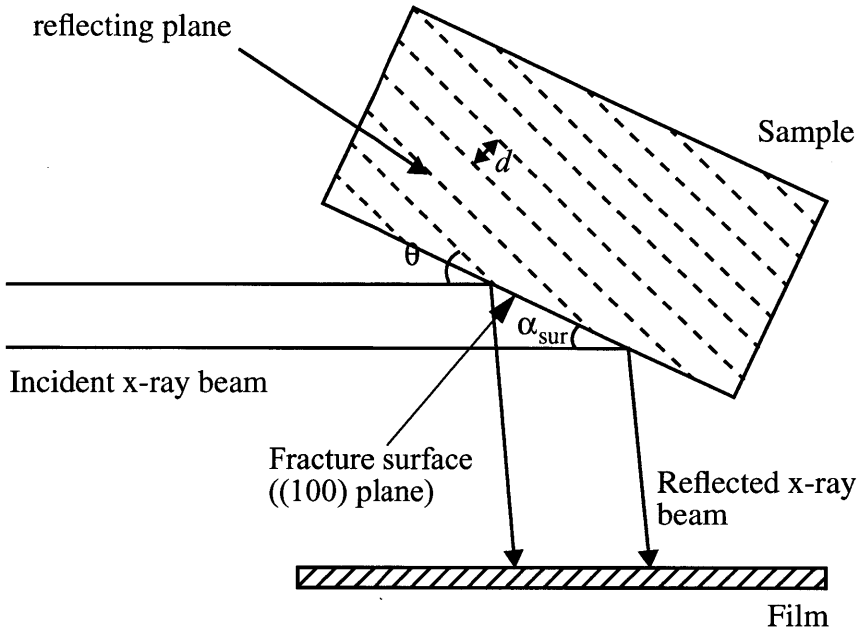

Fig.4-7 Top view of the Berg-Barrett set-up

A controlling system was produced such that the rotation angle of the goniometer could be adjusted smoothly by means of a copper wire from the outside while the x-ray generator was on. The tilt angle of the goniometer was controlled through a flexible shaft. Thus, through a Geiger counter, peak reflection from the desired crystallographic plane could be found by adjusting the two angles such that the orientation of the sample satisfied Bragg's law. Then, the film mounted on an aluminum plate and sealed by black tapes was installed on the film holder of the camera and positioned as close to the sample as possible, with the surface of the film parallel to the incident x-ray beam. The whole goniometer, including the sample and the film, moved back and forth along a precision track vertical to the incident x-ray beam and parallel to the horizontal plane, driven by a type 1470 drive motor. Thus, the x-ray beam could scan across the whole sample surface, and information about the dislocation structure exposed on the fracture surface

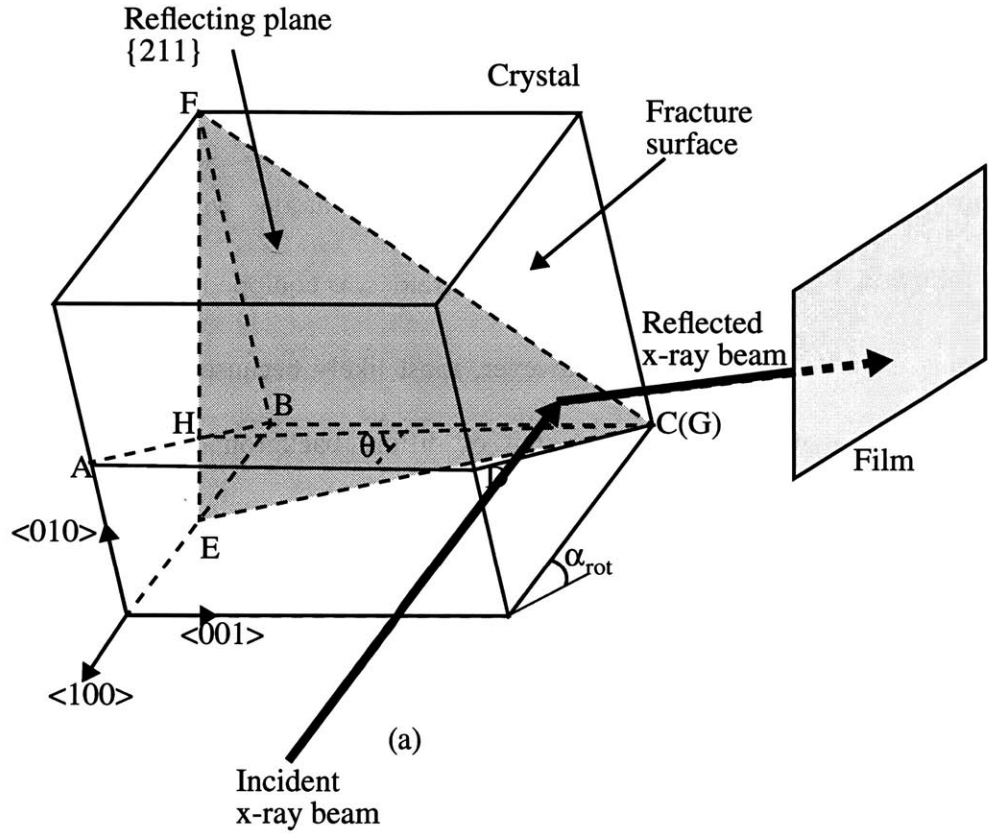

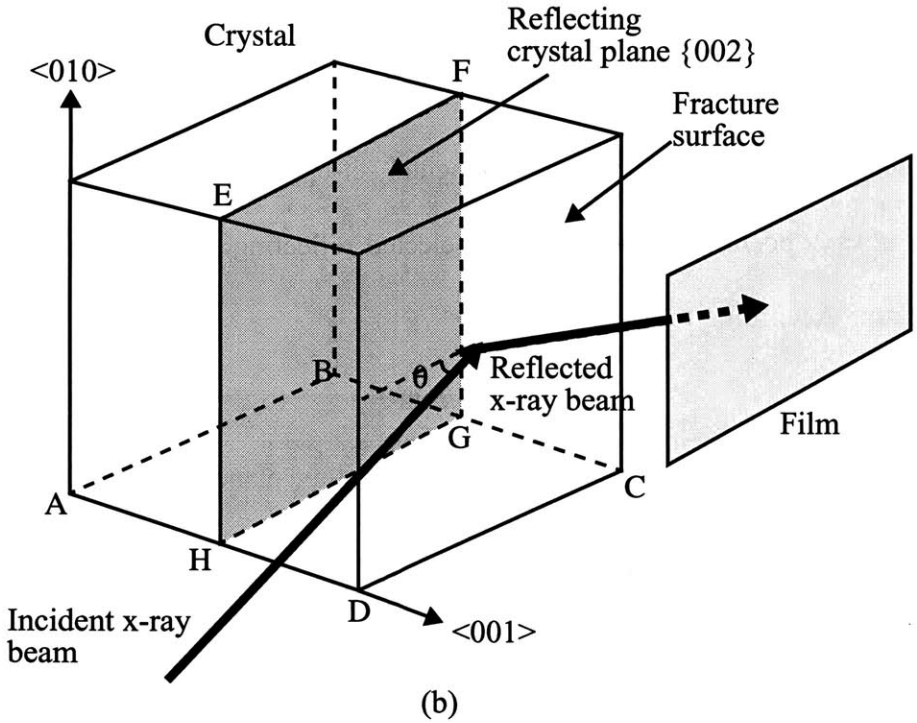

Fig.4-8 Choices of reflecting plane: (a) {112} plane, and (b) {002} plane.

could be recorded on the film. The film used in our measurement was Ilford 25-micron high-resolution nuclear plate, provided through the courtesy of Dr. David Black of NIST.

For best conditions for the use of the Berg-Barrett technique with Fe it is necessary to use Cr $K\alpha_1$ radiation. For this purpose the x-ray generator was equipped with a Cr rotating anode target producing a vertical line source. However, most likely because of the relatively high silicon content in the material, a large amount of diffuse background scattering was encountered, possibly due to fluorescent radiation from the silicon. To improve the images as much as possible, 30 micron thick V foil was placed immediately in front of the film to filter the fluorescent radiation from silicon in solution in the Fe as well as the white radiation from the Cr anode.

4.5.2 Reflecting crystal plane

Figure 4-7 shows the top view of the experimental set-up for the Berg-Barrett equipment. The sample was always positioned such that the selected reflecting plane was perpendicular to the horizontal plane. According to Bragg's law,

$$n\lambda = 2d\sin\theta \tag{4-4}$$

where n = 1, 2, 3...; d is the distance between reflecting planes, which can be calculated as $d = \frac{a}{\sqrt{h^2 + k^2 + l^2}}$, with a being the lattice parameter, and (hkl) being the indices of the reflecting plane; λ is the wavelength of incident x-rays, which is 2.2896Å for Cr $K\alpha_1$ radiation; and θ is the angle between the incident x-ray beam and the reflecting plane. For pure iron, the

lattice parameter a = 2.8664Å. The lattice parameter of Fe-3%Si alloy should be somewhat larger than this value because of the high Si concentration that dilates the lattice. Nevertheless, we will use this value in the following calculation for the first order determination of the diffraction conditions. In the real experiment, since the *in-situ* adjustment of the rotation angle and the tilting angle of the sample was possible, the θ-angle estimated below was a good starting point.

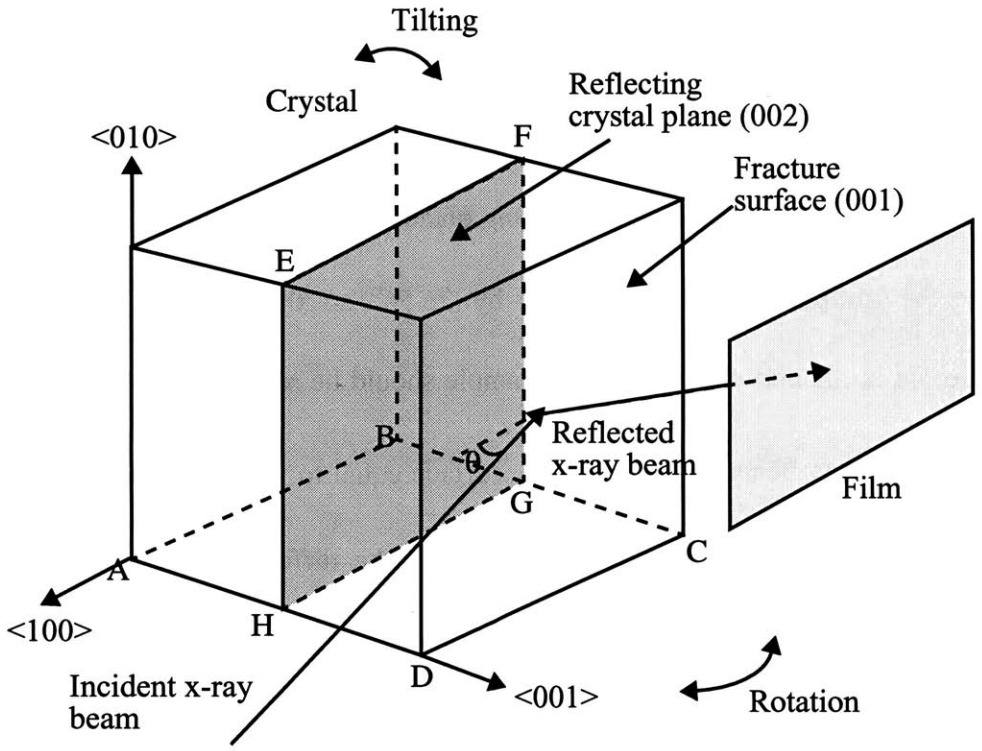

Fig. 4-9 Arrangement of single crystal of Fe-3%Si alloy with {200} being the reflecting plane.

Through Eqn.(4-4), the θ-angle can be calculated as

$$\sin\theta = \frac{\lambda}{2a}\sqrt{h^2+k^2+l^2} = 0.3994\sqrt{h^2+k^2+l^2} \qquad (4\text{-}5)$$

It can be seen that, among the reflecting systems which are not forbidden for BCC crystals, the only possible choices of reflecting planes are {110}, {200} and {112}. The {110} reflecting system is the strongest one. Unfortunately, the θ-angle for {110} system $\theta_{110} = 34.39°$ is smaller than 45°, therefore it is geometrically impossible to arrange the orientation of the sample to make the reflected x-ray beam hit the film. The {200} system is the next strongest one, and the θ-angle for it is $\theta_{200} = 53.02°$; The {112} system is the third strongest reflecting system, and its θ-angle is $\theta_{112} = 78.04°$.

Both of the {112} and {200} system are possible to be used in the Berg-Barrett imaging. The geometry of these two possible choices of reflecting planes is shown in Fig.4-8. However, to use {112} system, the sample needs to be tilted by 26.56° so that the (211) plane can be perpendicular to the horizontal plane. Then the sample should be rotated to keep the angle α_{sur} between the incident x-ray beam and the fracture surface equal to 12.14° to makes the θ-angle 78.04°. This process is very complicated and increases the difficulties in locating the peak reflection. In addition, the very large 2θ-angle 156.08° makes it difficult to arrange the experimental devices. Therefore, in our experiments, the {200} reflection was used.

Figure 4-9 shows schematically the arrangement of the sample with the (002) reflecting planes.

4.5.3 Experimental procedure

The Berg-Barrett experimental set-up was aligned and calibrated by using NaCl single crystals. Since the (200) plane is the strongest reflecting system in NaCl, the arrangement of the NaCl sample was very similar to that of the Fe-3%Si sample. The width of the first and the second collimator slits, the position of the collimator tube, and the height of the goniometer was optimized to get the clearest x-ray image of dislocation bands for NaCl single crystals that had been compressed by 2-3%. The width of the first slit was chosen to be 0.1mm, and that of the second slit was adjusted to be 0.15mm. The x-ray images taken for the NaCl crystals were of high quality and the shear bands in the crystals were shown clearly.

Because the intensity of the reflected x-ray beam was very sensitive to the orientation of the sample, to get high-resolution images, the rotation of the goniometer around the <010> direction (see Fig.4-9) had to be adjusted very accurately to keep the angle between the incident x-ray beam and the fracture surface within $\pm 0.1^\circ$ degree from the optimal θ-angle. Also, the fracture surface had to be kept exactly vertical to the horizontal plane, which required to adjust the tilting angle around the <100> direction (see Fig.4-9) very accurately.

Before the experiment, the sample was fixed on the goniometer by double-sided tape, and the Laue back reflection method was used to help find the exact zero position. A special holder of the goniometer was designed for the Laue back reflection x-ray machine with exactly the same locking-pin system as the that in Lang camera to minimize systematic error. Then, the goniometer with the sample fixed on it was inserted into the Lang camera and the rotation angle and the tilting angle were adjusted as well as possible to achieve the desired θ-angle. After the x-ray generator was turned on, these two angles were adjusted slightly through the control

system and the flexible shaft introduced above, respectively, until the peak reflection of the x-ray beam was detected by the Geiger counter attached to the camera. It was found helpful to put a third 0.2mm wide slit and another V filter in front of the Geiger counter to diminish the influence of fluorescent radiation from silicon and white radiation from the Cr anode.

After the peak reflection had been found, the Geiger counter was replaced by the film cassette containing the high-resolution nuclear plate, with the surface of the plate being parallel to the incident x-ray beam and being placed as close to the sample as possible. Usually, the distance between the plate and the sample was less than 0.5mm. During the experiment, the whole stage of the camera, including the goniometer and the film holder, was moved back and forth by a driving motor along the track perpendicular to the incident x-ray beam and parallel to the horizontal plane. The range of the movement was carefully controlled through a relay system such that the incident x-ray beam would only scan the area of the sample that was of interest. The exposure time of the nuclear plate was comparable to that of ISO 50 films. Usually, the exposure time had to be at least 6-7 hours per mm of scanning distance, with the x-ray source used.

After exposure, the nuclear plate was first hydrated in distilled water for 10 minutes, and developed in dilute D19 Kodak developer (2 parts water: 1 part developer) for about 40 minutes, then fixed in general Kodak fixer for about 2 hours until the whole plate became clear. The entire process was performed in an ice bath in total darkness. Finally, the plate was washed in running distilled water for at least 1 hour.

Because of the jerky nature of the fracture surfaces in Fe-3%Si alloy, and the very strict requirement of accuracy for crystal orientation, it was impossible to record dislocation structure of the whole fracture surface in one experiment. In each experiment, only a small portion of the fracture surface in which the orientation of the cleavage plane was nearly planar was scanned. The rest of the fracture surface would not show up on the film due to the slight changes of the orientation of cleavage plane in these regions. Even so, it was found that the x-ray images were always quite patchy, indicating that the cleavage plane in the exposed small area was apparently not really planar.

4.6 Experimental Results

4.6.1 Fracture resistance

Through a load-displacement curve, the critical stress intensity factor could be calculated for each crack jump, each crack stop and the final thermal arrest. The crack jump lengths were measured on the fracture surface through SEM after the experiments. In Fig.4-5, data point P_i (i = 1, 2,...5) gave the value of crack opening load when the crack started to jump, through which the critical stress intensity factor for crack jump could be calculated as (see Figs.4-2 and 4-3)

$$K_{IC} = Pa\sqrt{\frac{12}{(1-\nu^2)bb_n h^3}} \tag{4-6}$$

where b_n is the remaining crack width between roots of side grooves, and a is crack length. Similarly, the critical stress intensity factor for crack stops and final thermal arrest could be obtained through load values given by data points Q_i. The results are listed in Table 4.1, where

the critical stress intensity factor for a crack jump was denoted as K_{ICa}, and that for crack stop and thermal arrest was denoted as K_{ICb}.

Different loading rates were used for different samples. Figure 4-10 shows the relationship between measured brittle-to-ductile transition temperature T_{BD} and loading rate v ($v = \dot{\delta}$; see Fig.4-3). Considering the exponential relationship between loading rates and BDT temperature,

$$\nu \propto \exp\left(\frac{U}{k_B T}\right), \tag{4-5}$$

the activation energy of the triggering process of the brittle-to-ductile transition, U, was estimated to be 1.03eV.

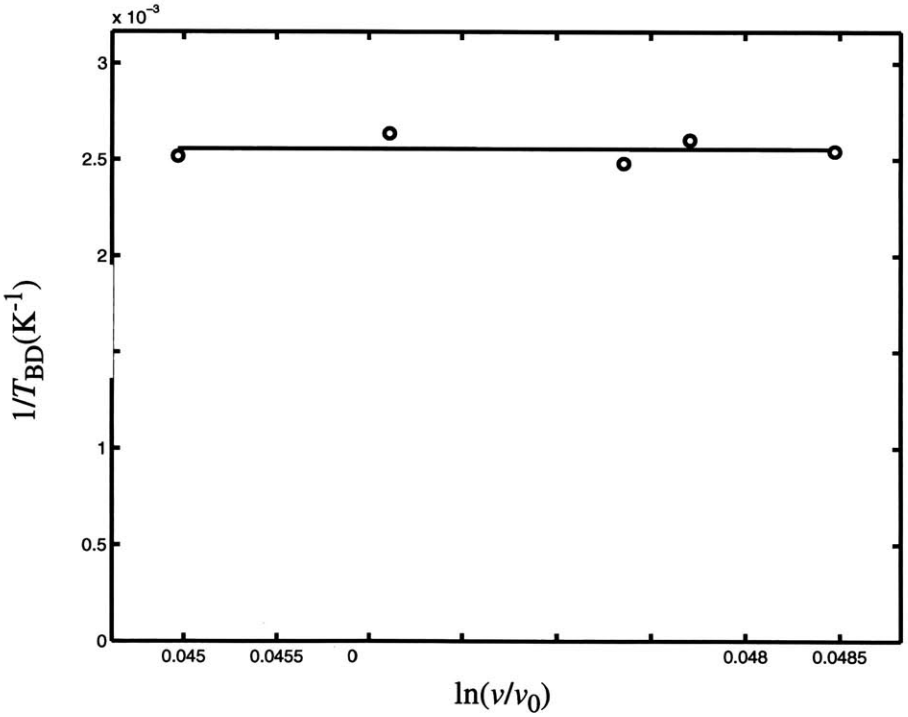

(v: rate of crack opening (mm/sec); v_0=1mm/sec)

Fig.4-10 Relationship between BDTT and loading rate

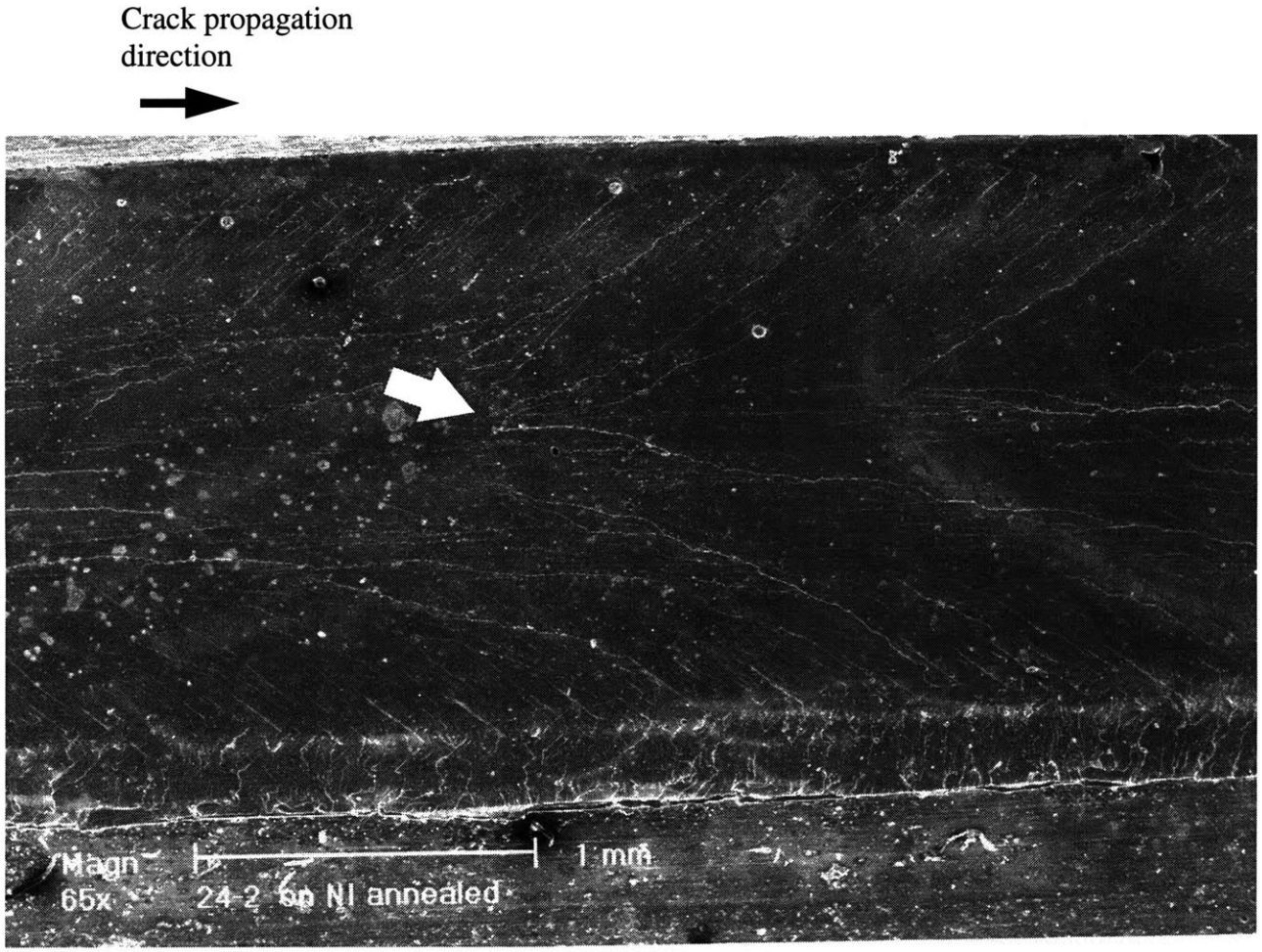

Fig. 4-11 SEM photo of a crack stop in sample 100c (the arrow indicates the place where the crack front was stopped).

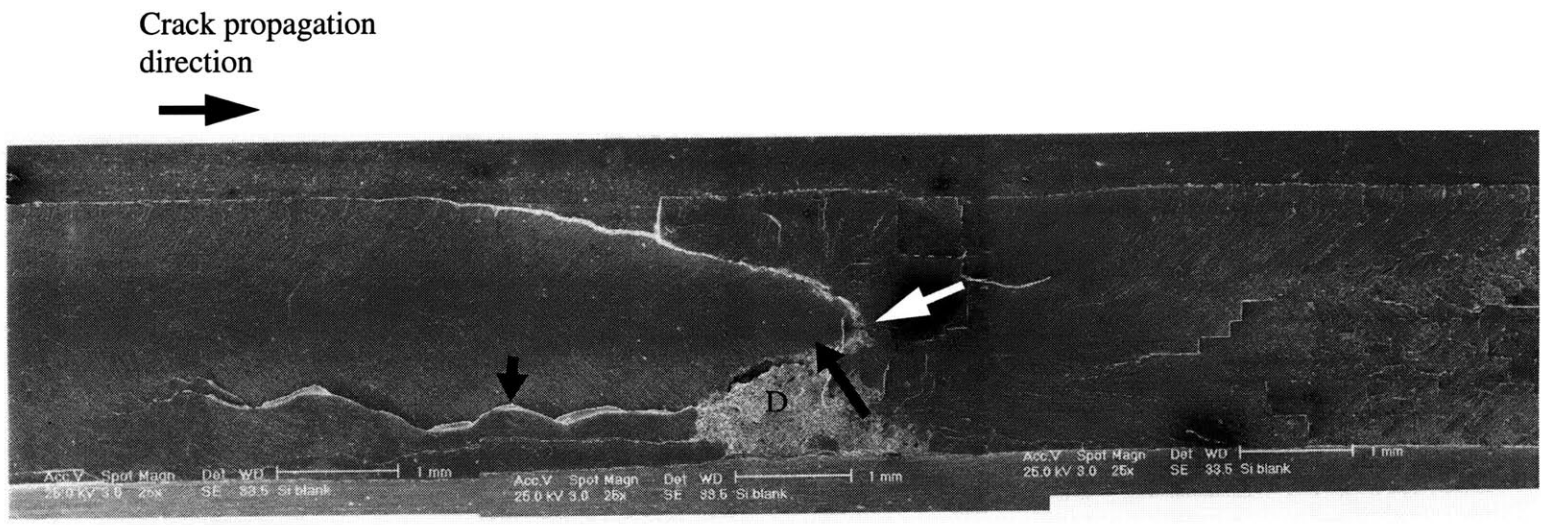
Crack propagation
direction
D
Acc.V Spot Magn Det WD 1 mm
25.0 kV 3.0 26x SE 33.5 Si blank

(a)

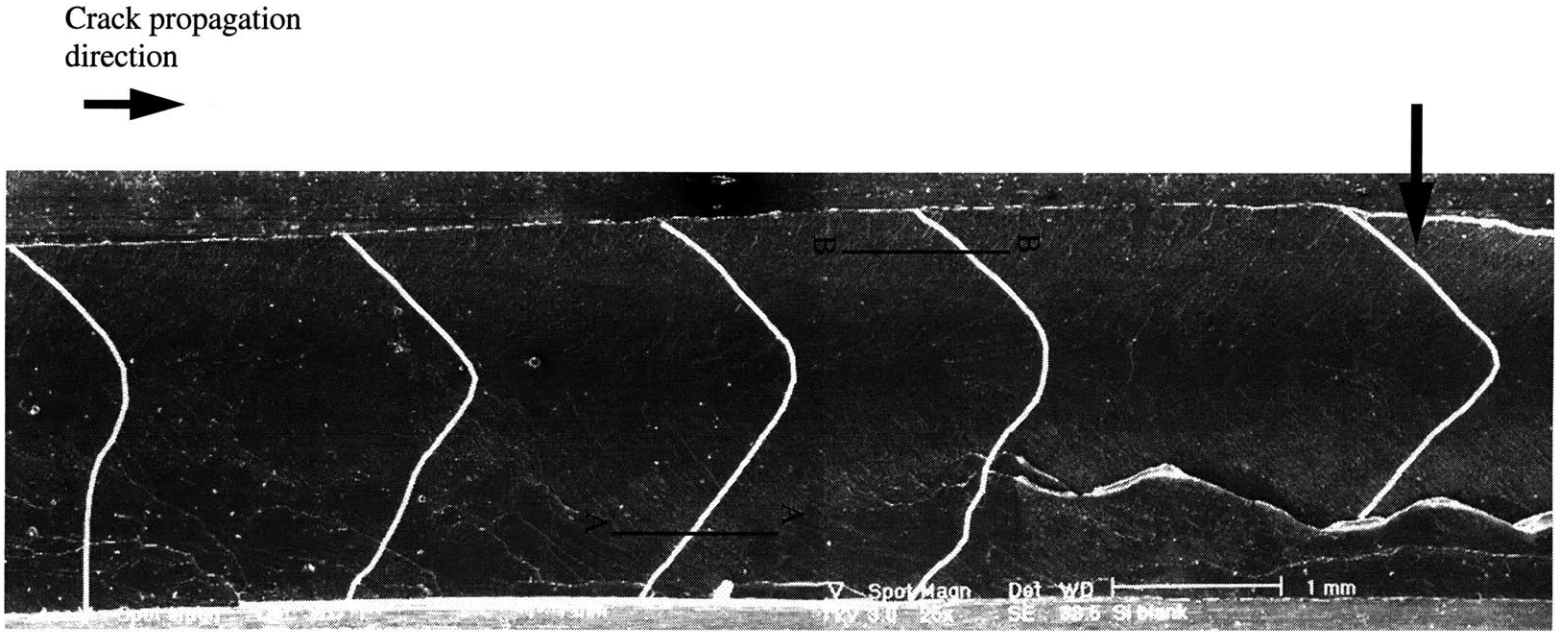

(b)

Fig.4-12 SEM photoes of (a) the thermally arrested crack front in sample 100g. The ductile dimples area was produced after the crack front had been arrested, and the cleavage surface at right hand side of the arrested front was produced after the experiment under liquid Nitrogen temperature; and (b) curved crack front during propagation in the same sample as (a).

4.6.2 Fractography

Fracture surfaces were observed through SEM and Zygo[1] microscope. Figure 4-11 shows one of the crack front stoppage regions after a jump corresponding to a load drop from P_i to Q_i depicted in Fig.4-5 in the brittle propagation regime before the crack was thermally arrested. It can be seen that, although some new river markings were produced, many old ones just continued to extend through the stoppage zone on the new fracture surface produced after this stop, indicating that the plastic behavior at the crack tip during these dynamic crack stops was negligible. The crack front kept propagating in jumps until it reached a region where the temperature was high enough for the fracture process to undergo a thermal brittle-to-ductile transition. The initiation of plastic events through some dislocation generation at the crack tip that increased the fracture resistance of the material sharply arrested the crack. Upon continued insertion of the wedge into the DCB specimen, further crack blunting would occur as well as slow growth of the part of the crack front close to the roots of side grooves, through a ductile dimple mode of fracture. After the experiment, the specimen was separated at liquid nitrogen temperature. During this process, new cleavage surface was produced at the arrested crack front, while pre-existing dislocation structure inside the single crystal would presumably not be changed. Figure 4-12a shows a thermally arrested crack front in sample 100f (see Table 4.1). Unlike the crack stop shown in Fig.4-11, here substantial evidence of plastic response is evident at the arrest zone. Additional

1. An Instrument that uses scanning white light interferometry to image and measure the micro structure and topography of surfaces in three dimensions (New View System 5000, produced by Zygo Corp. of Middlefield, Connecticut).

blunting and ductile dimple fracture in region "D" occurring subsequent to the arrest upon further wedge insertion is also shown clearly.

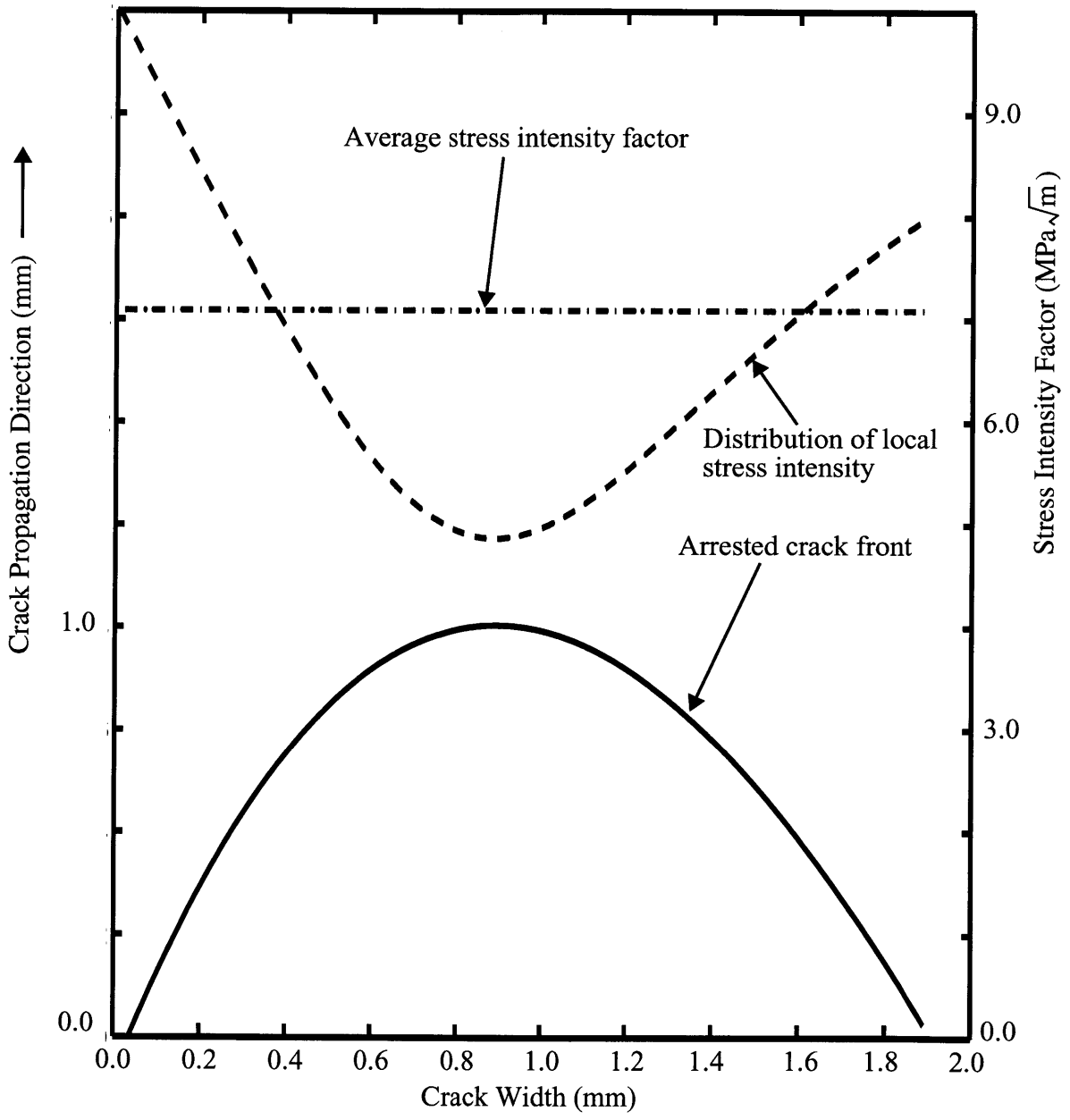

Fig. 4-13 Distribution of local stress intensity along the curved crack front indicated by the arrow in Fig.4-12b.

Figure 4-12b shows several propagating crack fronts drawn normal to directions of local river markings. Note that the shape of the propagating crack front is roughly self-similar during propagation and was "flatter" than the eventual thermally arrested front. This should be the result of the relatively large local fracture resistance at the root of side grooves due to effects of plane stress condition. In the pure elastic case, the local K_I is considered to be zero at a free surface as is discussed in Section 4.7 (Benthem, 1977, 1980; Nakamura and Parks, 1989), thus the crack front close to the surface lagged behind the portion at the central zone of the specimen, where plane strain conditions dominate. Another reason for the formation of curved crack front appears to be, due to the relatively high propagation speed during each jerky advance, the flat crack front becomes somewhat unstable resulting in a dynamic roughening near the free surface as we also discuss in Section 4.7. Therefore the local fracture resistance close to the two side surfaces of the front should be higher than that in the central zone of the specimen. Because of this, the part of the crack front close to the side-groove roots would be arrested first, while the central part of the crack front would continue to propagate further to a region of higher temperature until the whole crack front is arrested, producing a more convex arrested front.

An estimate of the distribution of local stress intensity based on the analysis of effective local fracture area along the arrested crack front is shown in Fig.4-13. The average value of the stress intensity along the whole arrested crack front was the measured overall critical value of $7.1\,\mathrm{MPa}\sqrt{\mathrm{m}}$, while the values of local stress intensity varied in the range from $4.8\,\mathrm{MPa}\sqrt{\mathrm{m}}$ at the central part of the specimen to $9.7\,\mathrm{MPa}\sqrt{\mathrm{m}}$ at the root of side groove. Note that the lowest value of local stress intensity factor at the central part of specimen was relatively close to the

$2.4\text{MPa}\sqrt{\text{m}}$ of K_{IC} corresponding to the surface free energy of the (100) plane of Fe-3%Si measured by Gilman (1960), compared with the value of $14.1\text{MPa}\sqrt{\text{m}}$ measured in bi-crystal samples (Chapter 2).

Figure 4-14 shows river markings at both sides of the sheared ligament shown in Fig.4-12a by the short black arrow. According to the river markings, the three parts of the crack front across the ligaments propagated independently. The curved main part of the crack front (at the bottom of Fig.4-14) produced considerable undercuttings below the strip, and at the same time the relatively straight upper parts of crack front propagated from left to right at a different height across the ligament. Since the bending deformation was very large, the ligament should not have been sheared apart when the crack front was thermally arrested. The final separation of the ligament occurred after the experiment was over when the specimen was forced apart to expose the fracture surfaces at liquid nitrogen temperature.

Figure 4-15 shows two profiles of the fracture surface in Fig.4-12b along lines A-A and B-B exploring the polarity of the cleavage steps. It can be seen that the height change associated with river markings was a mixture of somewhat random and ordered nature. The slopes of steps are all in the same direction, while the height differences between neighboring steps are quite arbitrary. The random change of height difference between steps is considered to be of the type modeled by Xu (1994) that can be used to explain the instability of the crack front close to the root of the side-grooves, increasing the local fracture resistance.

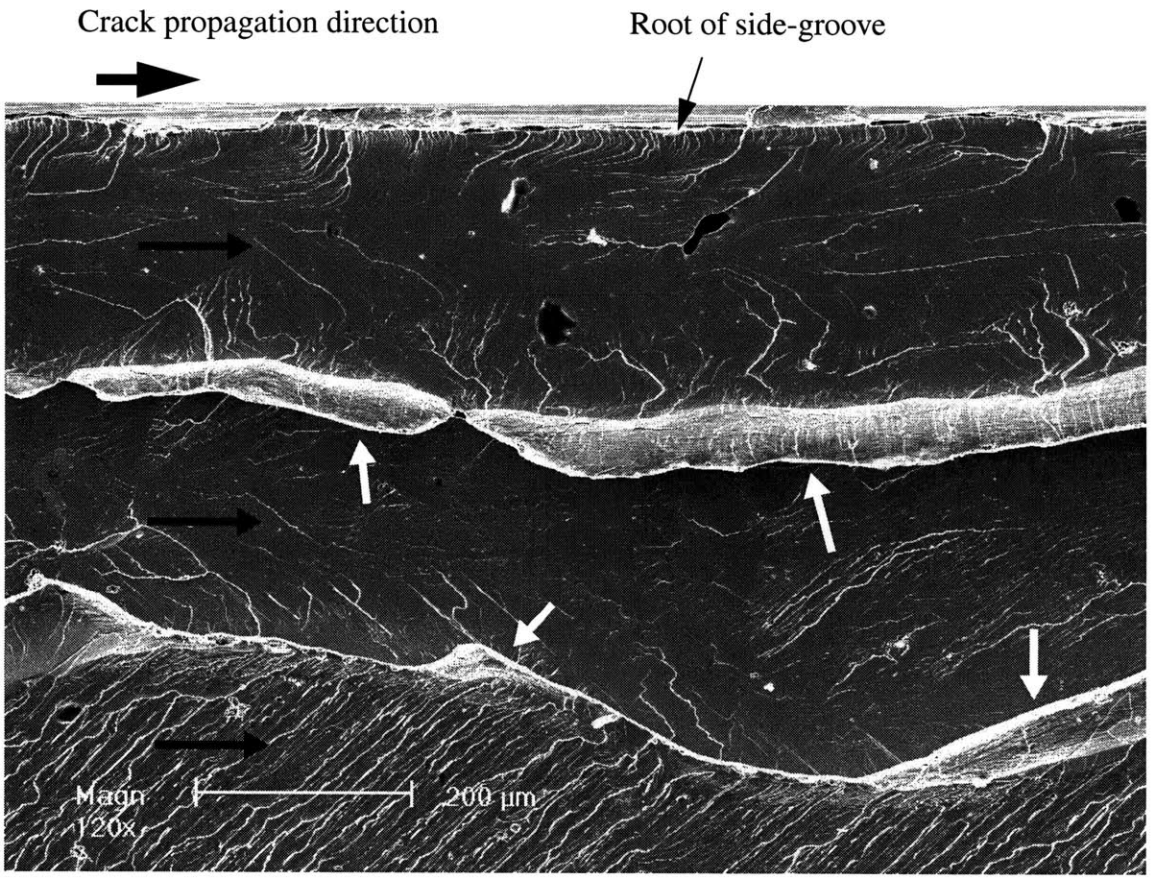

Fig.4-14 SEM fractography of the strip on fracture surface of sample 100g shown by the white arrow in Fig.4-12. It can be seen that crack front propagation processes at different heights (shown by black arrows) were independent, and the ligaments (shown by white arrows) were bent and sheared apart later.

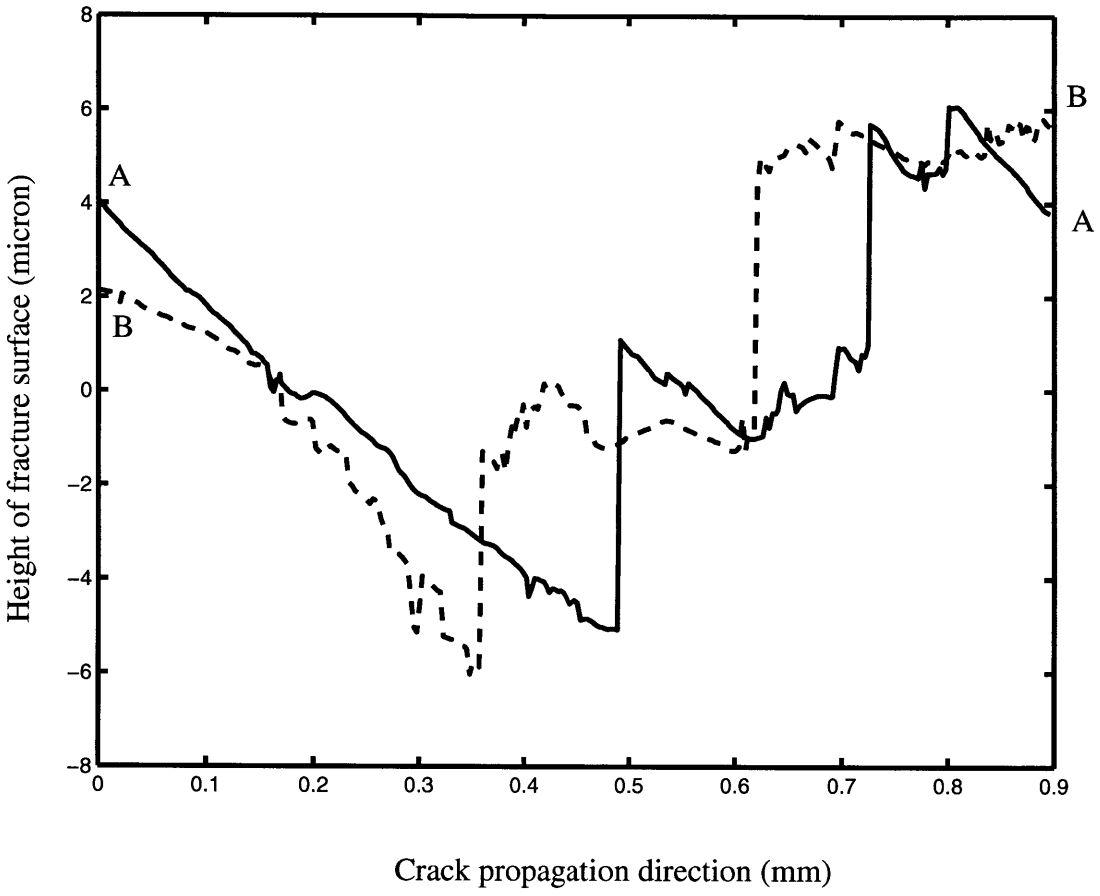

Fig.4-15 Two profiles along lines A-A and B-B respectively of the fracture surface shown in Fig.4-12b.

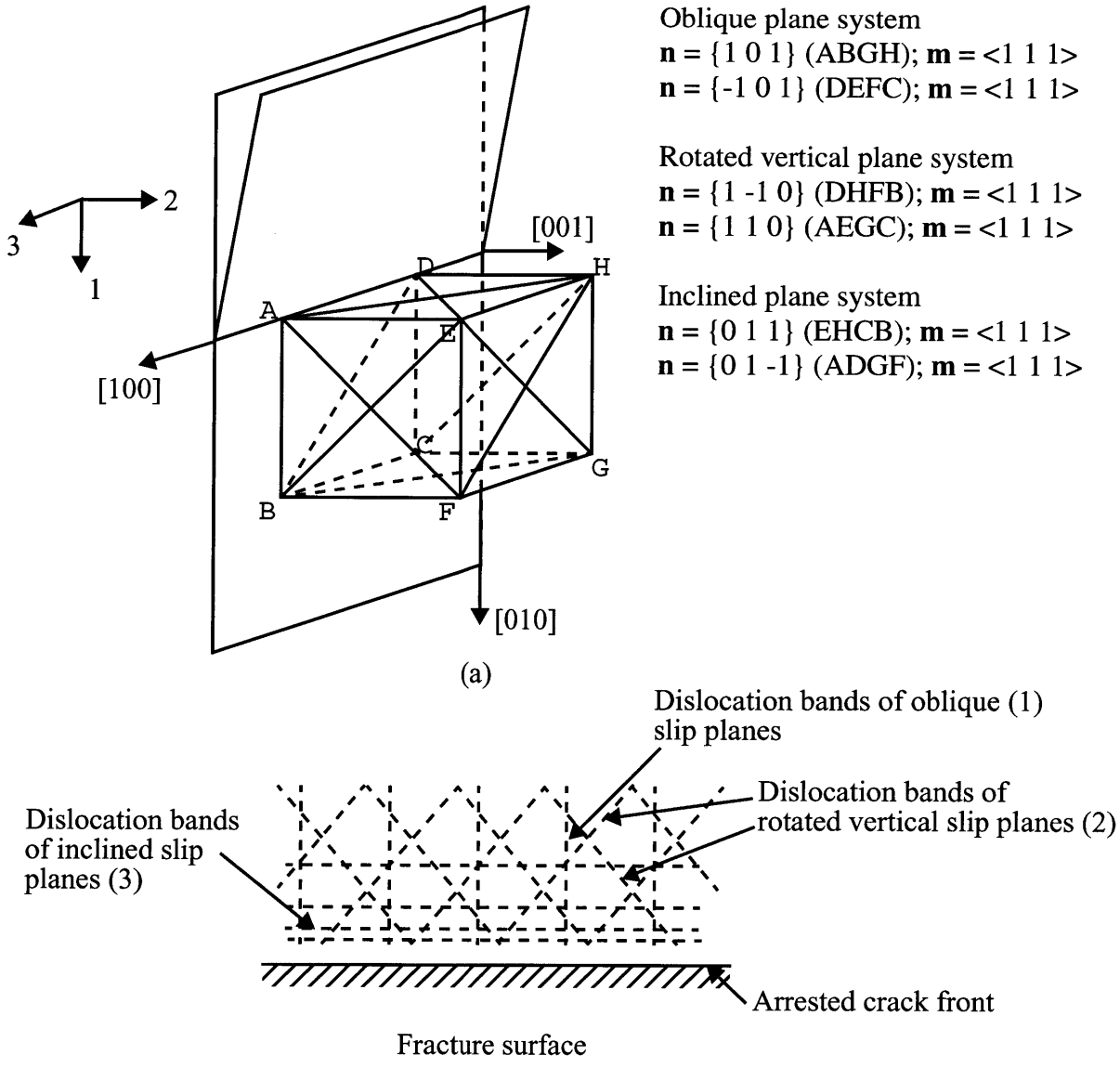

Fig.4-16 Slip systems at crack tip in group A specimens with [010] direction parallel to the desired crack propagation direction: (a) slip systems; (b) expected dislocation structure exposed on the fracture surface ABCD.

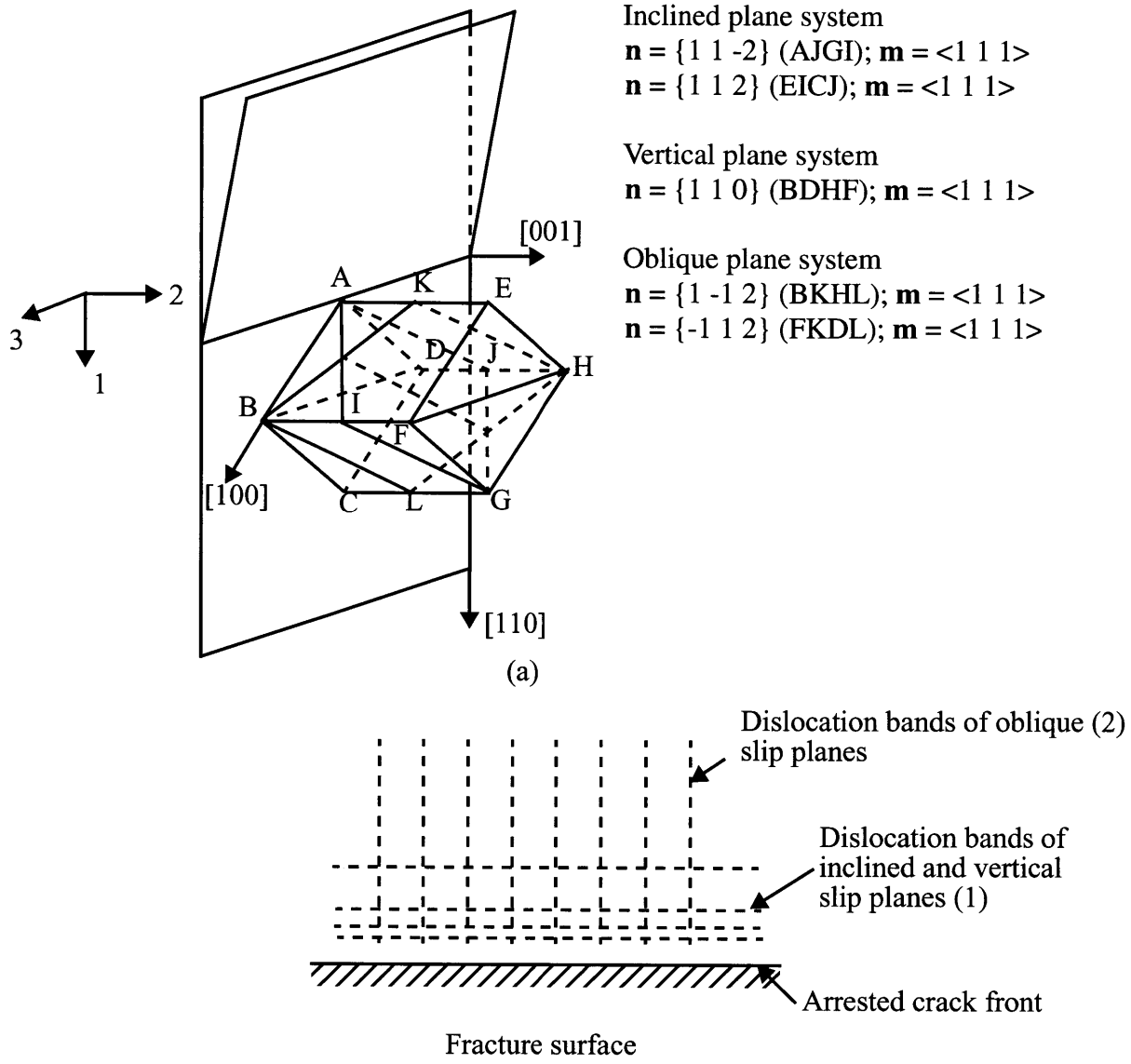

Fig.4-17 Slip systems at crack tip in group B specimens with [110] direction parallel to the desired crack propagation direction: (a) slip systems; (b) expected dislocation structure exposed on the fracture surface ABCD.

The average rms roughness of the fracture surface was measured to be 1.8 micron by means of the Zygo microscope. The typical spacing between two parallel river-markings was in the range from 5 microns to 60-70 microns, and the average value was about 15 microns. If the temperature was below the BDT temperature, the fracture surface was of mixed-cleavage nature. Most of the area of the fracture surface had undergone cleavage in nearly a plane, while evidences of plastic bending and ductile shearing of ligaments could be observed occasionally. These phenomena will be studied in detail in Chapter 5.

4.6.3 Berg-Barrett x-ray images

To determine potential dislocation activities associated with the thermal crack arrest so that the Berg-Barrett images can be better understood, levels of resolved shear stress on possible slip systems in group A (Fig.4-16) and group B (Fig.4-17) samples were calculated, and slip systems with largest peak resolved shear stresses were identified for the two groups, respectively. These slip systems, which are listed in Fig.4-16 and Fig.4-17, are considered to be responsible for the plastic behavior at crack tip during the thermal crack arrest process.

In Figs.4-16a and 4-17a, the crystallographic structures at the crack tip for both a group A sample and a group B sample are shown. The fracture surface always lies in (001) plane, and the crack propagates along the <010> axis in group A sample, and along a <110> direction in the group B sample, respectively. The stresses at a point P near the crack tip can be evaluated by using a crack tip solution of Hoenig (1982), which gives:

$$\sigma_{ij} = \frac{K_{\text{appl}}}{\sqrt{2\pi\tilde{r}}} Re\{f_{ij}(\tilde{\theta})\}, \tag{4-6}$$

where K_{appl} is the applied stress intensity factor; i, j =1, 2; $\tilde{r}$ is the distance from point P to the crack tip; $\tilde{\theta}$ is the cylindrical coordinate angle to the crack propagation direction (see Fig.4-18a); and the f_{ij} are functions of $\tilde{\theta}$, which were calculated through

$$f_{11} = \frac{\mu_2\mu_1^2}{(\mu_2-\mu_1)\sqrt{\cos\tilde{\theta}+\mu_1\sin\tilde{\theta}}} - \frac{\mu_1\mu_2^2}{(\mu_2-\mu_1)\sqrt{\cos\tilde{\theta}+\mu_2\sin\tilde{\theta}}} \tag{4-7}$$

$$f_{22} = \frac{\mu_2}{(\mu_2-\mu_1)\sqrt{\cos\tilde{\theta}+\mu_1\sin\tilde{\theta}}} - \frac{\mu_1}{(\mu_2-\mu_1)\sqrt{\cos\tilde{\theta}+\mu_2\sin\tilde{\theta}}} \tag{4-8}$$

$$f_{12} = \frac{\mu_2\mu_1}{(\mu_2-\mu_1)\sqrt{\cos\tilde{\theta}+\mu_1\sin\tilde{\theta}}} - \frac{\mu_1\mu_2}{(\mu_2-\mu_1)\sqrt{\cos\tilde{\theta}+\mu_2\sin\tilde{\theta}}} \tag{4-9}$$

where μ_k (k = 1, 2) are functions of the anisotropic elasticity constants of the crystal. They are complex roots of a polynomial equation with positive imaginary parts:

$$l_4(x) = s_{11}x^4 + (2s_{12}+s_{44})x^2 + s_{22} = 0 \tag{4-10}$$

where s_{ij} are compliance constants of the material. The coordinate axes are defined as shown in Fig.4-16a and Fig.4-17a, with the 1-axis being parallel to the crack propagation direction, 2-axis normal to the fracture surface, and 3-axis along the crack front. For single crystal of Fe with orientation shown in Fig.4-16a, the elastic stiffness constants are c_{11} = 237GPa, c_{12} = 141GPa, and c_{44} = 116GPa, through which the elastic compliances could be derived.

For plane strain conditions, there is an additional plane strain stress component

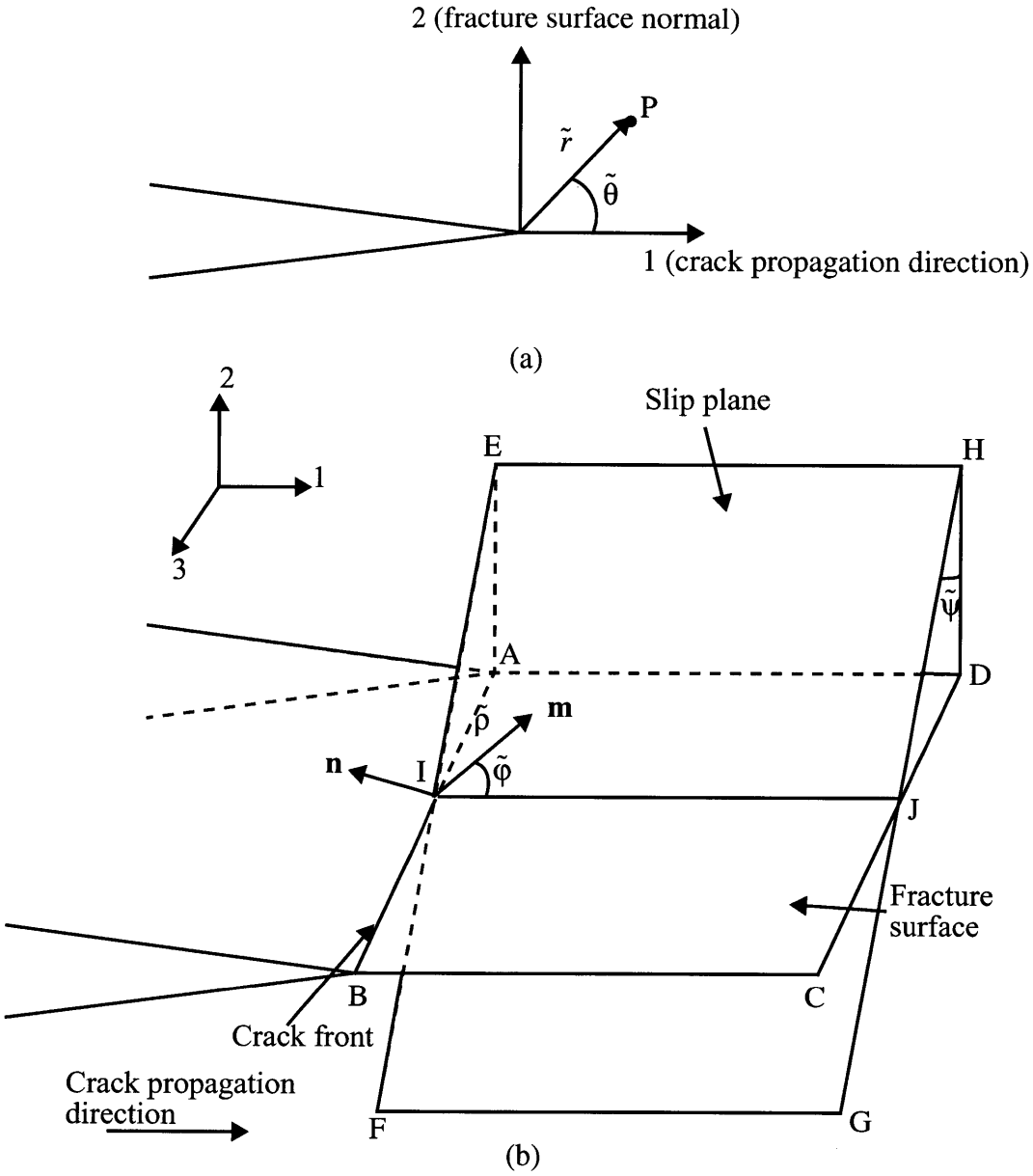

Fig.4-18 Schematic diagram of (a) stress field at crack tip; and (b) resolved shear stress of a slip system with the normal of slip plane of **n** and the slip direction of **m**. The fracture surface is ABCD; the slip plane is EFGH; $\tilde{\psi}$ is the angle between EADH and EFGH; $\tilde{\varphi}$ is the angle between IJ and **m**.

$$\sigma_{33} = -\frac{s_{12}}{s_{11}}(\sigma_{11} + \sigma_{22}) \tag{4-11}$$

Thus, the resolved shear stress along a slip system with the normal of slip plane **n** and slip direction **m** could be calculated by projecting all the stress components along the slip direction on the slip plane (see Fig.4-18b), which gives

$$\tau_{nm} = \frac{K_{\text{appl}}}{\sqrt{2\pi\tilde{\rho}}} g_{nm}(\tilde{\varphi}) \tag{4-11}$$

where $\tilde{\rho}$ and $\tilde{\varphi}$ are analogues to $\tilde{r}$ and $\tilde{\theta}$, but are now in the slip plane; $\tilde{\psi}$ is the angle between the slip plane and the virtual plane with the normal of the crack front; and g_{nm} was derived through the orientation of the slip system and the near-tip stress tensor. The numerical results for slips systems with the largest peak resolved shear stresses are shown in Figs.4-19 - 4-24.

According to the analysis of the crack-tip stress field, the slip systems with largest maximum resolved shear stress were identified. Through Figs.4-19 to 4-24, these are for group A the oblique plane system, the rotated vertical plane system, and the inclined plane system; for group B, they are the inclined plane system, the oblique plane system and the vertical plane system in descending order in the magnitude of resolved shear stress. The expected slip plane traces on the exposed fracture surfaces of Fe-3%Si alloy single crystal samples are shown in Fig.4-16b and Fig.4-17b, with the expected order of activity indicated in descending order by numbers (1)-(3). In Iron-Silicon alloy, the mobility of edge dislocations are much higher than that of screw dislocations, as for all BCC metals (Stein and Low, 1960; Saka and Imura, 1973). The movement of edge dislocations can be observed under stress levels much lower than the yield strength. The overall yielding of the material is triggered by the movement of screw dislocations. The nucleation of screw dislocations begins much earlier than their movement, associated with the

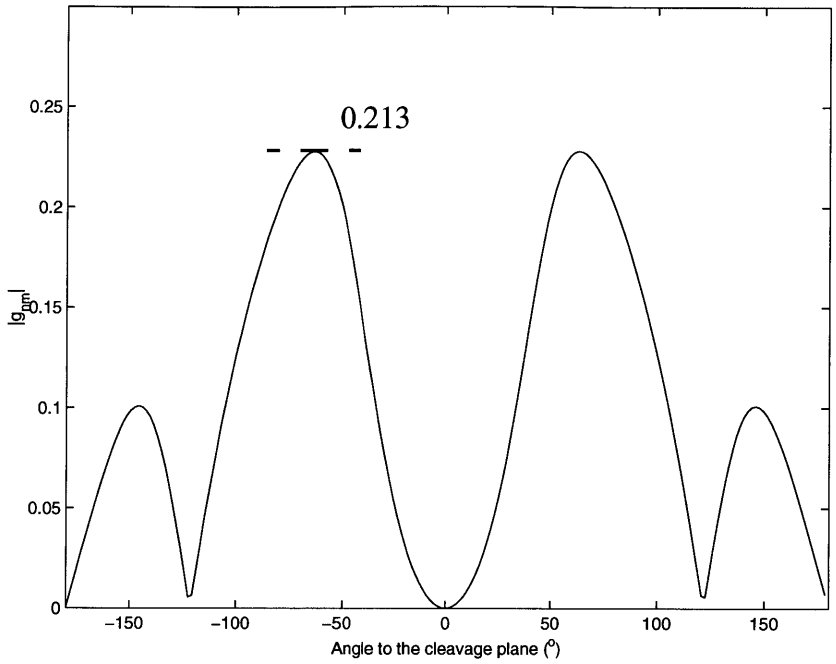

Fig. 4-19 Plot of absolute value of g_{nm} on the inclined slip plane system in group A sample with <100> axis parallel to the crack propagation direction (see Fig.4-16).

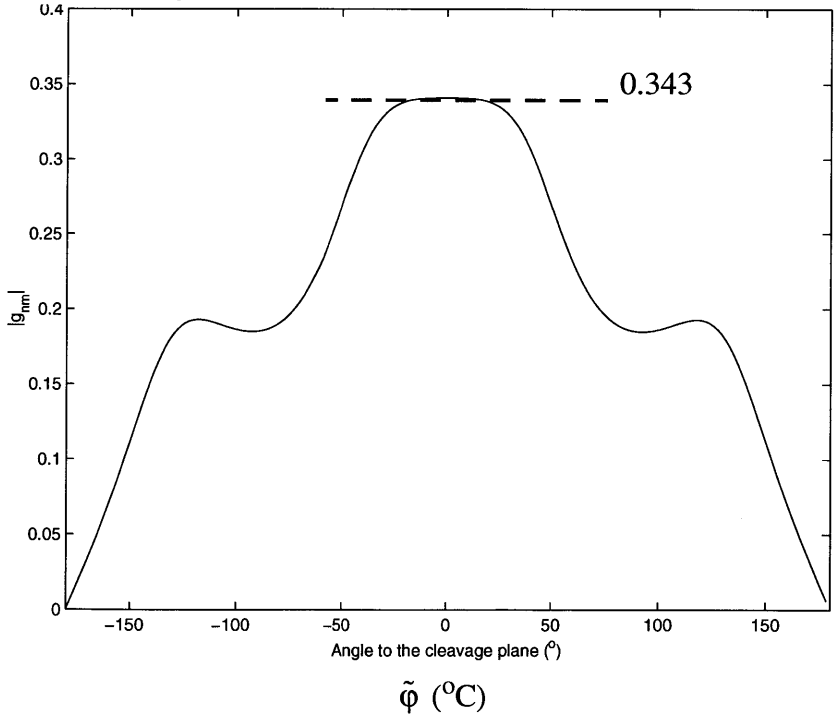

Fig. 4-20 Plot of absolute value of g_{nm} on the oblique slip plane system in group A sample with <100> axis parallel to the crack propagation direction (see Fig.4-13).

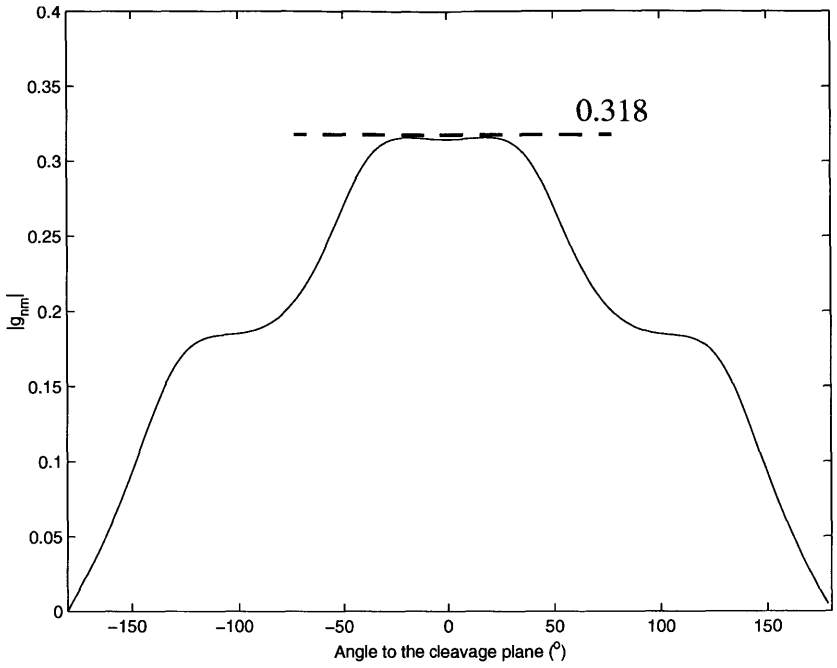

$\tilde{\varphi}$ (°C)

Fig. 4-21 Plot of absolute value of g_{nm} on the rotated vertical slip plane system in group A sample with <100> axis parallel to the crack propagation direction (see Fig.4-13).

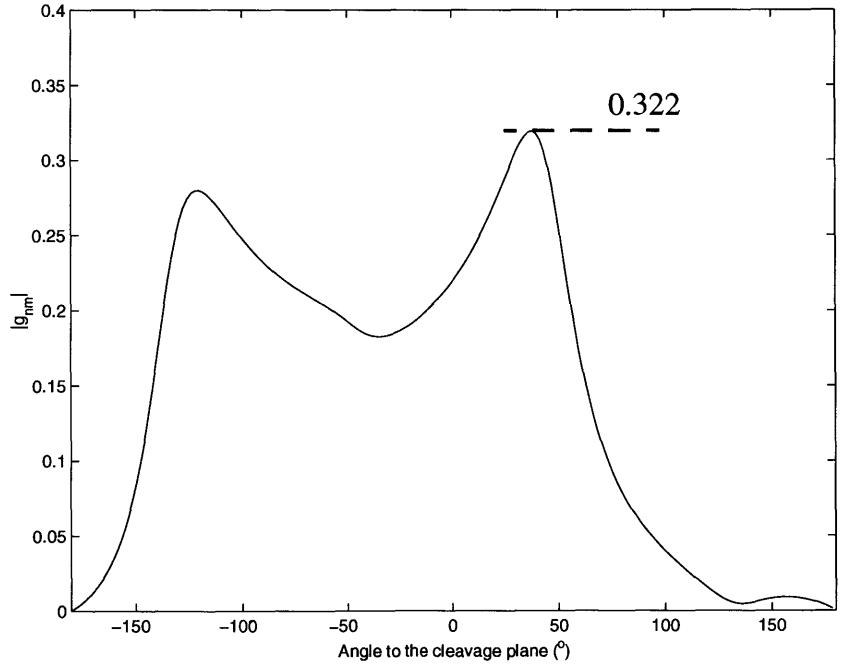

$\tilde{\varphi}$ (°C)

Fig. 4-22 Plot of absolute value of g_{nm} on the inclined slip plane system in group B sample with <110> axis parallel to the crack propagation direction (see Fig.4-14).

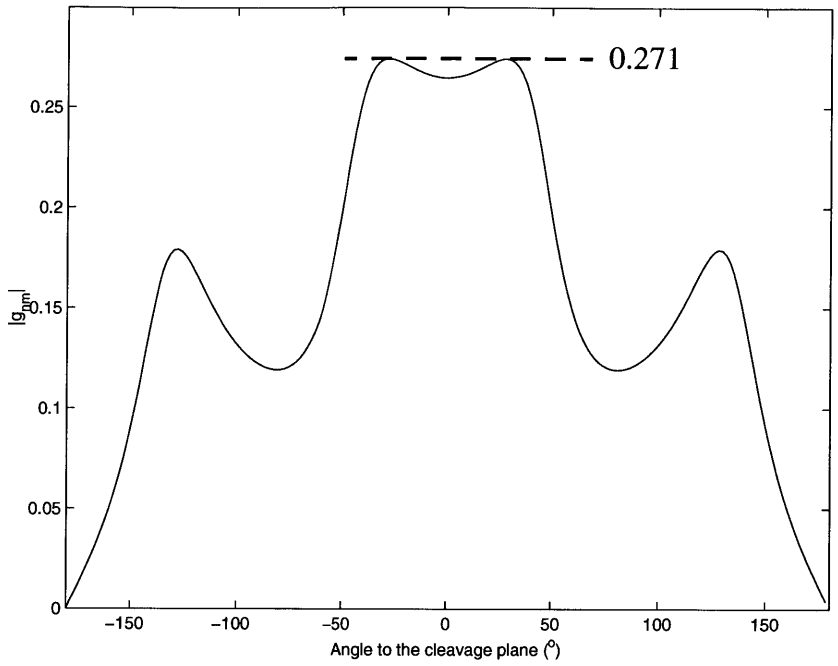

$\tilde{\varphi}$ (^{o}C)

Fig. 4-23 Plot of absolute value of g_{nm} on the oblique slip plane in group B sample with <110> axis parallel to the crack propagation direction (see Fig.4-14).

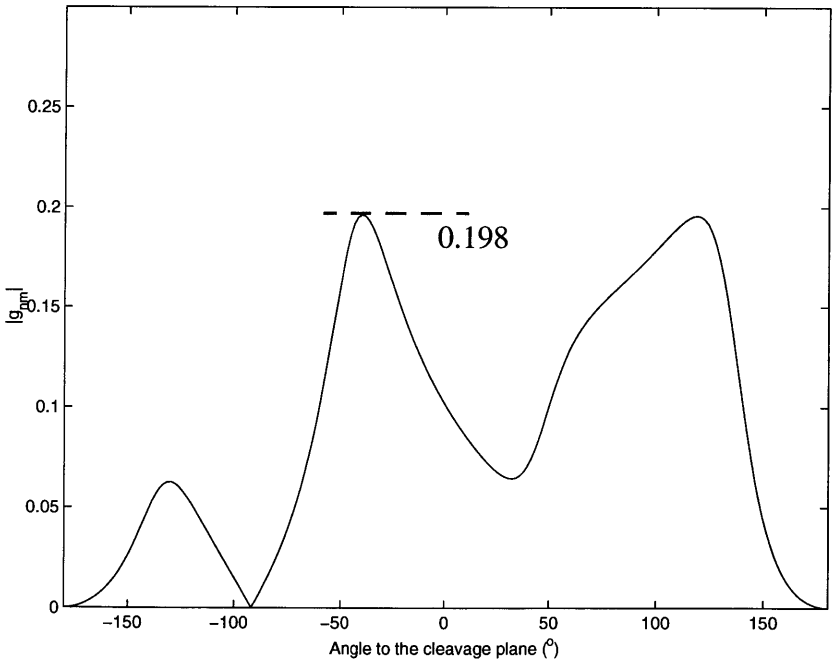

$\tilde{\varphi}$ (^{o}C)

Fig. 4-24 Plot of absolute value of g_{nm} on the vertical slip plane system in group B sample with <110> axis parallel to the crack propagation direction (see Fig.4-14).

movement of edge dislocations. Thus, in general case, the mobility of dislocations at the crack tip should dominate the brittle-to-ductile transition in Fe-Si alloy (Hirsch et al., 1988).

If the dislocation population were plentiful, during the brittle-to-ductile transition, dislocations should be activated first in the slip systems with largest peak resolved shear stress and glide along the corresponding slip directions. On cleavage surfaces fractured under liquid nitrogen temperature, dislocation bands in group A samples and group B samples should exist along directions shown in Fig.3-16b and Fig.3-17b, respectively. Similar dislocation bands have been observed in initially dislocation free silicon single crystals by Gally and Argon (2001).

Figure 4-25 shows a Berg-Barrett x-ray topographic image of the dislocation structure behind the thermally-arrested crack front in a group A sample shown in Fig.4-12. The long black arrows in Fig.4-12 and Fig.4-25 point to the same area. Due to the very patchy nature of the image, there is no clearly-delineated correspondence with any of the expected bands shown in Fig.4-16. Figure 4-26 shows another Berg-Barrett image for the area in front of the thermally-arrested crack front indicated by the white arrow in Fig.4-12a. Through this image of denser regions of enhanced contrast, there is some correspondence with the predicted orientation of dislocation bands, as shown in Fig.4-16b. Clearly, there is no satisfactory means of deciding whether or not the dislocation patterns shown in Fig.4-26 might be directly related to the triggering event of the thermal crack arrest process, since the central part of the crack front had propagated further after the part of crack front close to roots of side grooves had already been arrested.

Berg-Barrett x-ray images were also taken for the fracture surface in grain *A* of a bi-crystal specimen studied in Chapter 2. Figure 4-27 shows the SEM fractography, and Fig.4-28 shows the corresponding x-ray image. It can be seen that, at the root of ligaments under sigmoidal bending, there are black bands, an indication of a large amount of dislocation behavior. This result is consistent with our observation about the plastic bending and shearing of ligaments reported in Chapter 2 and Chapter 3. Note that the bottom part of fracture surface did not show up in Fig.4-28, indicating that the cleavage plane in this area deviated from the primary cleavage surface slightly, as shown in Fig.4-29 from which the main image was derived. However, due to the patchy nature of the x-ray image, it is difficult to conclude whether the dark lines and spots on the x-ray image reflect actual dislocation patterns or just the imperfect nature of the cleavage surface.

4.7 Discussion

Through the experimental data of fracture resistance around $7\text{MPa}\sqrt{\text{m}}$ in single crystals studied in this chapter, compared with the $14.1\text{MPa}\sqrt{\text{m}}$ of K_{IC} of grain *A* in bi-crystal fracture experiment discussed in Chapter 2, it can be seen that the fracture resistance of the single crystals was much lower, although the chemical compositions of the two materials were quite similar. The silicon contents were about 3wt% and the carbon contents were less than 0.01wt% after decarburization in both materials. An interesting observation was that the rms roughness of fracture surfaces in the single crystals was only about half of that in grain *A*, which can be attributed to the fact that the deformation twin density in grain *A* was much larger than that in the single crystals practically showing no pre-existing twins. Since when a crack front propagated

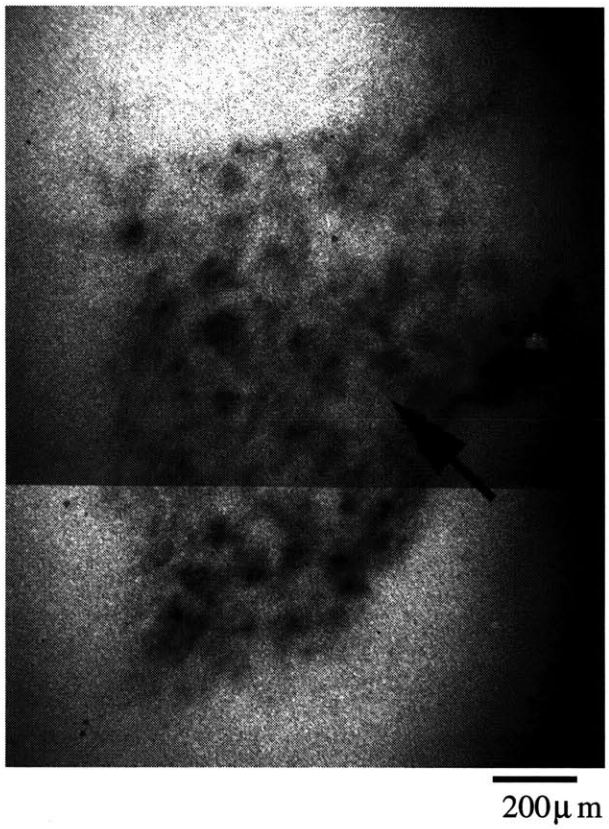

Fig. 4-25 Berg-Barrett x-ray image of fracture surface immediately behind the thermally arrested crack front shown in Fig.4-12. The dislocation pattern is very unclear due to the patchy nature of the cleavage surface and large Si content.

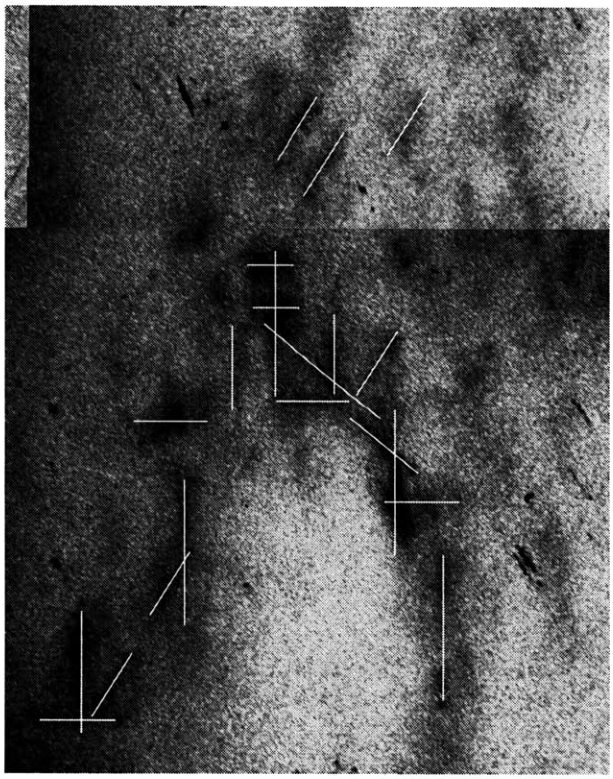

Fig.4-26 Berg-Barrett x-ray image of dislocation structure in front of an arrested crack front in a group A specimen indicated by the white arrow in Fig.4-12a. The dislocation pattern is very unclear because of the patchy nature of the cleavage surface and the relatively large Si content.

Fig. 4-27 SEM photo of grain *A* in one of bi-crystal specimens studied in Chapter 2.

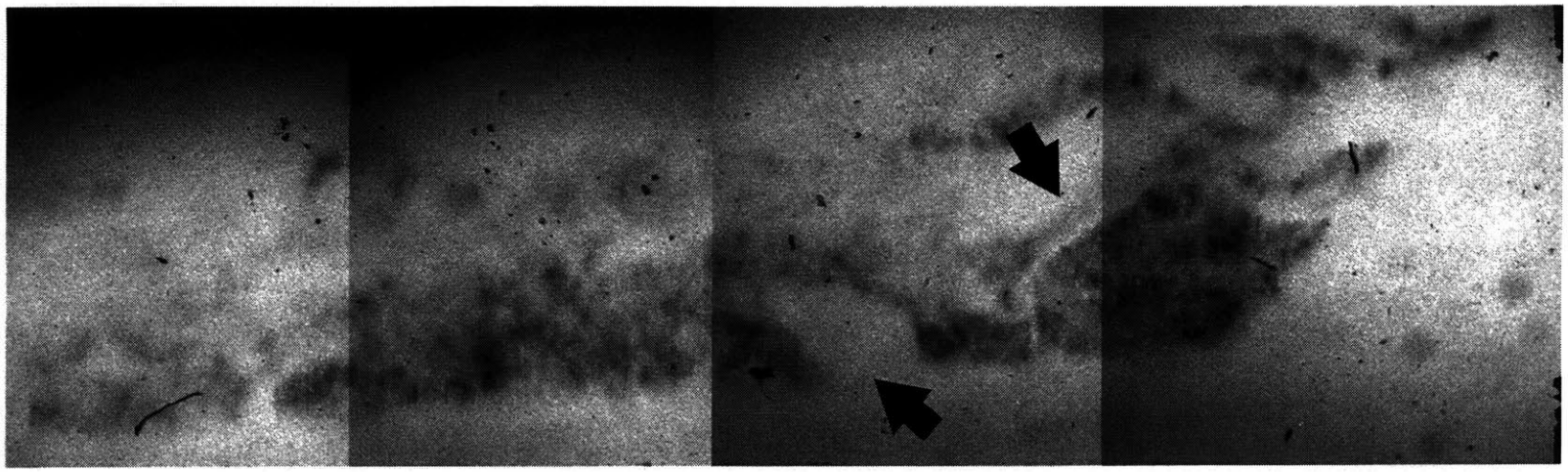

Fig.4-28 Berg-Barrett x-ray image of fracture surface of grain *A* shown in Fig.4-17.

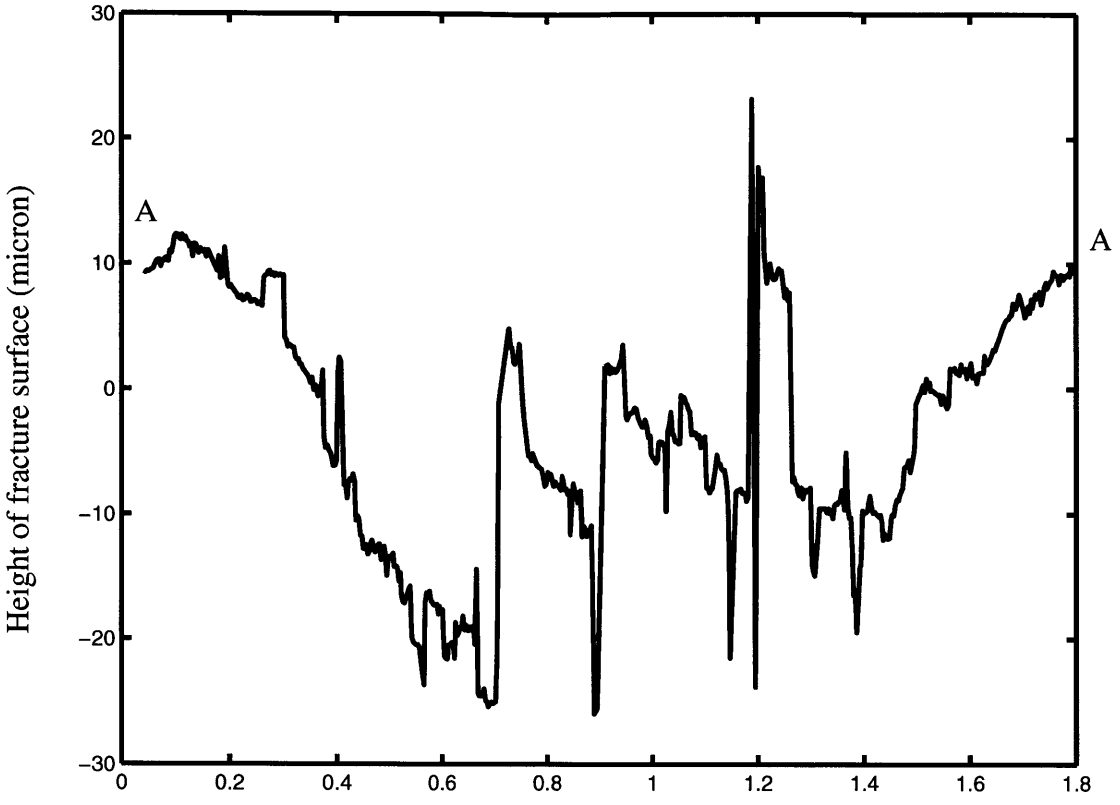

Fig.4-29 Profile of fracture surface along line A-A in Fig.4-26.

through a deformation twin, it disrupts the cleavage surfaces and results in placing the cleavage plane at different heights producing a large amount of undercuttings and separated strips. The roughness of the overall fracture surface would then be greatly increased. The fracture surface roughness could also be related to other factors such as dynamic effects due to high crack velocities. No matter what the cause of the difference of the fracture surface roughness of the two materials was, this difference, clearly resulted in different levels of fracture work to bend and shear apart ligaments to finish the final separation of adjoining crack flanks, and as a

consequence in the different overall fracture resistances that were measured. A detailed model for this phenomenon will be developed in Chapter 5.

According to the directions of river markings, the convex shape of the propagating crack front remains quite constant during crack advance. Because of the plane stress conditions at the free surface, in the pure elastic case it has been demonstrated that the local stress intensity factor is zero at the end of a crack front where the crack front tangent is normal to the free surface (Benthem, 1977, 1980; Nakamura and Parks, 1989), which, together with the fact that the roughness of fracture surface close to the roots of side grooves is higher than that in the central zone of the specimen, results in larger local fracture resistance at the two ends of crack front compared with the central part. Consequently, the central part of crack front protrudes ahead. The relatively high roughness of fracture surface close to the roots of side grooves could be caused by the instability of dynamic crack propagation discussed by Xu (1994). When the crack front reached the region where the temperature is high enough, the two ends of the crack front are arrested first at lower temperature while the central part propagates further to a higher temperature region where it is arrested, producing a more convex tongue-shaped arrested crack front.

The Berg-Barett x-ray topographic images, while on the whole of disappointing quality, nevertheless provided some evidence that our prediction of slip systems shown in Fig.4-16 and Fig.4-17 was quite reasonable, which was also confirmed by observations of slip lines on the fracture surface of sample 100g through a Nomaski light interference contrast microscope (see Fig.4-30). In the dislocation-mobility controlled brittle-to-ductile transition process, the slip

systems with highest maximum resolved shear stress are expected to be activated first, which produces various dislocation bands causing crack tip shielding. Although, due to the patchy nature of the x-ray images, it was impossible to see detailed dislocation structures in the material, there was, nevertheless, evidence that thermally initiated dislocation movements had been responsible for the observed sharp brittle-to-ductile transition. Berg-Barrett x-ray images also showed that on cleavage surfaces there was considerable dislocation activity at roots of ligaments being sigmoidally bent and plastically sheared, which causes considerable energy dissipation and raises the overall fracture work. This observation was compatible with features of ligaments on SEM fractography and the discussion above about the relationship between fracture surface roughness and fracture resistance. A detailed discussion will be performed in following chapters.

As already stated above that the quality of Berg-Barrett x-ray topographic images obtained from Fe-Si fracture surfaces was too indistinct to reach definitive conclusion on dislocation patterns. Actually, in Figs.4-25 and 4-26, the quality of the images is so poor that any correlation between dislocation patterns and fractography derived through these images becomes very unreliable. This makes discussion on dislocation activities associated with crack arrest impossible. A reason for this very disappointing result could be that in our experiment the active slip planes are not at all parallel to the reflected x-ray beam, making the image of dislocations on the film diffuse and less reinforced compared with what was obtained in the Berg-Barrett imaging for single crystals of silicon (Gally and Argon, 2001), consequently, the sharpness of Berg-Barrett images of Fe-Si alloy is much less. Another reason could be the relatively large content of silicon. The silicon content in the Fe-Si alloy was 3.6% by weight, indicating that the atomic concentration of silicon

was more than 10%. Such a large Si content would most likely result in local clustering of Si atoms at very fine length scale and cause substantial random lattice distortion of Fe. Figure 4-31 shows fractography of a single crystal of pure iron and its Berg-Barrett image. The carbon content of the material was 0.019wt%, the silicon content was 453ppm, and the contents of phosphorus, sulfur, manganese, and chromimum were all smaller than 99ppm. Without the large content of Si, the scattering pattern is considerably clearer, but still difficult to be related to river markings or sub-grain structures. This could be caused by the imperfect nature of the cleavage surface and orientation variation of the reflecting planes. Due to the very low ductile-to-brittle transition temperature of pure iron, even at liquid-nitrogen temperature and relatively high strain rate, there still existed a certain amount of plastic deformation associated with the cleavage crack advance, as well as splitting of cleavage planes into different levels. Thus, the crystallographic cleavage surfaces are no longer parallel and planar, and the outlines of the dark areas of the Berg-Barrett x-ray images are determined by the somewhat wavy structure of the fracture surface instead of dislocation patterns. Since slight deviation of a part of cleavage surface from the orientation defined by Bragg's law would greatly decrease the intensity of reflection and the corresponding region in Berg-Barrett x-ray image would become bright area, even through there could be rich dislocation structures inside this field, it would not register on film. The Berg-Barrett method is good at studying defect structures in nearly-perfect crystals. In our experiment, the unfavorable orientation of slip plane and the large content of silicon, which causes serious background scattering as discussed in Section 4.5.1 and distortion of Fe lattice as discussed above, together with the patchy nature of mixed-cleavage surfaces, make Berg-Barrett method far less definitive for the Fe-Si alloy.

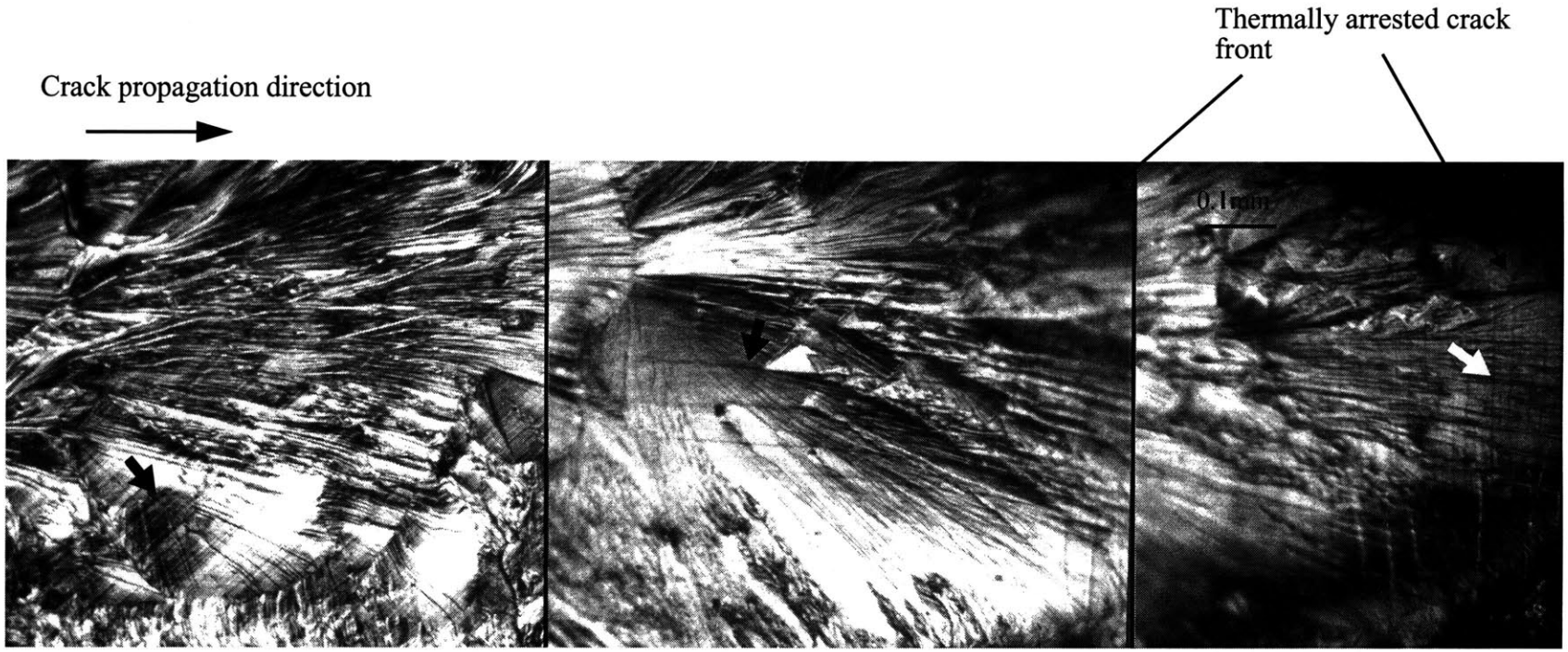

Fig. 4-30 Slip lines on the fracture surface of sample 100g shown in Fig.4-12, imaged with a Nomarski light interference contrast microscope: (a) slip lines tilted from the crack propagation direction by 45°, corresponding to the rotated-vertical-plane slip system; (b) slip lines parallel to the crack propagation direction, corresponding to the oblique-plane slip system; and (c) slip lines normal to the crack propagation direction, corresponding to the inclined-plane slip system (see Fig.4-16b).

(a)

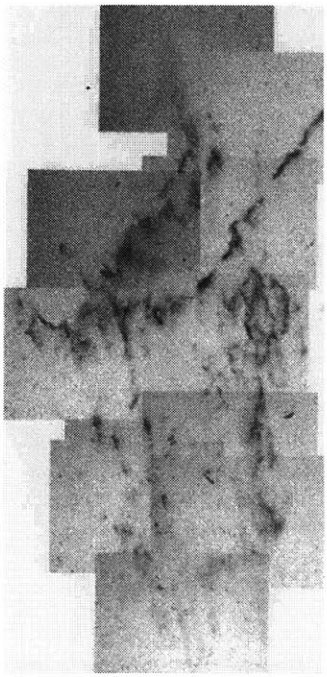

(b)

Fig.4-31 (a) Fractography of cleavage surface of a single crystal of pure iron; (b) corresponding Berg-Barrett image.

CHAPTER 5

PROCESS ZONE MODEL FOR CLEAVAGE CRACK PROPAGATION

As discussed in Chapter 2, the fracture toughness K_{ICA} of grain *A* of the bi-crystal pairs at -20C was found to be quite reproducible at an average level of 14.1 MPa$\sqrt{m}$, which converts to a very substantial work of fracture of G_{ICA} = 850J/m^2 that requires explanation (see Chapter 2). Examination of the fracture surfaces in Figs. 2-9a and 2-9b shows only characteristic cleavage markings, but also much evidence of strong interactions of cleavage cracks with deformation twin bands resulting in periodic arrests and reinititions of the cleavage cracking, and in the fragmentation of the cleavage plane into separate strips advancing at different levels, as already pointed out above. There was considerable additional evidence, as shown e.g. in area "*o*" of Fig. 2-9b, of repeated weaker crack arrest, and reinitiation events resulting in the production of sets of smaller cleavage strips, indicating a very jerky nature of crack advance, modulated by the twins and possibly by dislocation microstructure. The net effect of these crack-plane shunting processes has resulted in a tiered fracture surface with an rms roughness of 2.7 microns as reported above. We view this fragmentation of the crack plane as the source of the substantial critical crack opening displacement δ_c associated with the crack advance.

In conventional interpretations of linear elastic fracture mechanics, in a small scale yielding setting, these measurements would be interpreted as having resulted from a quasi-statically advancing crack tip possessing a plastic zone of a radius $r_p \approx \frac{1}{\pi}\left(\frac{K_{ICA}}{Y}\right)^2$ ahead of it, and a

critical crack opening displacement $\delta_c = r_p(Y/E)$, where Y would be the quasi-static tensile yield strength and E the Young's modulus. In the present case where the prevailing values are Y = 0.25GPa, and K_{ICA} = 14.1MPa$\sqrt{m}$, these expressions would give r_p = 1.0mm and δ_c = 1.15μm respectively. While these estimates are not too unreasonable, the critical plastic zone size is somewhat too large and the opening displacement too small in comparison with expectations based on the fundamentally cleavage nature of the fracture surface features. Moreover, the development suggests a very conventional response of a plastic dissipation process *proceeding* the cleavage cracking as is typical in "upper shelf" cracking response, where the final cleavage separation in the previously plastically deformed zone is assumed to make only a negligible contribution to the overall fracture work.

In the present case where the temperature at -20C is roughly 270C below the conventional brittle-to-ductile transition temperature (Fig. 3-3), and the fracture surface features give much evidence of a jerky advance of a fragmented cleavage crack, far removed from a quasi-static response, we view the events of crack advance in a different order. We start by noting that the *Fe*-3%*Si* alloy is an intrinsically brittle solid in the temperature range of our experiments, embrittled further by the high concentration of *Si* which is a potent-solid solution strengthening agent in *Fe*. When a "steady state" form of crack advance is established, with all its jerky features, as evidenced from the fracture surface markings of Figs. 2-9a and 2-9b, the average crack plane becomes fragmented, as discussed above, into a set of separate parallel cleavage strips. As depicted in Fig. 2-16, the separate cleavage strips of average width, w_c, are considered to penetrate into undeformed material at the tip of a process zone, (PZT), of extent Δ_c, without

any accompanying plastic dissipation. This is in conformity with expectations from an intrinsically brittle solid well below its transition temperature where conditions of crack tip cleavage are reached well before conditions of plastic flow. As the cleavage strips of the PZT advance on planes randomly separated over a range δ_c, the edges of the strips that are left behind are subsequently bridged by processes of secondary cleavage-like fracture with plastic rubbing and some fragmentation. The major element of dissipative work is then done in the process zone of extent Δ_c until the two flanks of the rough cleavage crack are separated by the distance δ_c and all contact is terminated at point (CT), the crack tip. Such a process in which the inelastic dissipation is *subsequent* to the advancement of the cracking front resembles those frequently encountered in brittle composites reinforced with discrete fibers of a given length (δ_c) (Argon, 2000). The mechanics of the advance of such a process zone in which a characteristic traction separation (TS) process, illustrated in Fig. 5-1 is present and "processes" unbroken solid into fully-separated crack flanks has been considered in detail by Andersson and Bergkvist (1970)(AB). We adapt our findings to their model. In that model, which approximates the descending portion of the TS process law by a straight line over the separation distance CCOD = δ_c, the critical process zone size Δ_c is given by

$$\Delta_c = \beta_c \frac{E}{\sigma_B}(CCOD) \tag{5-1}$$

where the constant $\beta_c = 0.43$ is obtained from a numerical solution, σ_B is the average cohesive strength required to advance the cleavage front forward, and the CCOD is taken as the rms roughness range, $\delta_c = 2.7 \times 10^{-6}\text{m}$, as measured here. With the prevailing parameters as given above, and taken σ_B as 1.0 GPa, the process zone size Δ_c is estimated to be $2.5 \times 10^{-4}\text{m}$.

Moreover, the AB model gives the essential work of fracture consisting of the inelastic dissipative processes along the process zone as

$$G_{\mathrm{ICA}} = \frac{\sigma_{\mathrm{B}}(CCOD)}{2} \tag{5-2}$$

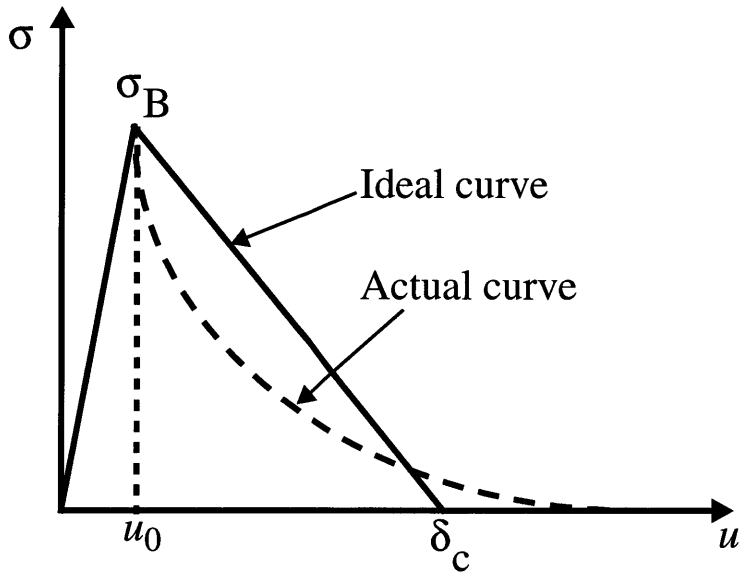

Fig. 5-1 An idealized traction separation TS profile demonstrating dissipative action in the process zone as proposed in the Andersson-Bergkvist model.

For the above-chosen parameters, G_{ICA} becomes 1,350 J/m^2, or somewhat larger than the measured value of 850 J/m^2, with the discrepancy being readily accountable by a most probable drooping shape of the TS law, as depicted in Fig. 5-1. Finally, from these developments the cleavage strip width w_{c} can be calculated, as:

$$w_{\mathrm{c}} = \frac{Y(CCOD)^2}{2\sqrt{3}G_{\mathrm{ICA}}} \approx 0.62 \times 10^{-6}\mathrm{m} \tag{5-3}$$

for a tensile flow stress of Y= 0.25GPa and a G_{ICA} = 850J/m^2, as measured experimentally. Where it is assumed that the inelastic dissipation occurs as plastic shearing.

While we prefer this interpretation of plastic dissipation *subsequent* to the initial cleavage penetration over the more conventional approach of cleavage *following* plastic dissipation, the actual behavior might be a combination of these two limiting responses.

CHAPTER 6

MODEL FOR FRACTURE RESISTANCE TO CLEAVAGE CRACKING OF BI-CRYSTAL GRAIN BOUNDARY

Referring to Fig. 2-10 representing the regular mode of penetration into the adjoining grain across the grain boundary and the schematic of Fig. 2-11, we view the sequence of processes of penetration of the cleavage crack up to the point of peak resistance as follows:

By a quasi-regular sampling process, the nature of which is not fully clear, the cleavage crack from grain A penetrates into grain B at points, on the average a distance w apart and spreads out on cleavage strips in grain B separated by distances $w\tan\varphi$, much like the early forms of penetration of brittle cracks between tough heterogeneities in a crack trapping model (Bower and Ortiz, 1991; Mower and Argon, 1995) with the as-yet-to-be sheared triangular grain boundary segments acting momentarily as the heterogeneities. Upon the penetration of the fragmented, terraced cleavage strips into grain B by increasing distances Δx, the opening displacements of the cleavage terraces begin to "force apart" the remaining triangular grain boundary islands to give way by a combination of plastic shear and shear cracking of the grain boundary over a relative shear displacement δ_B across the grain boundary faces that must depend on the distance of penetration Δx of the crack into grain B, i.e., $\delta_B = \beta\Delta x$. The remaining grain boundary islands finally give way completely when δ_B reaches a total displacement δ_{Bc}, at which time Δx reaches the critical level Δx_c where the maximum penetration resistance is reached.

The increase in the expended energy ΔU required for overcoming the boundary resistance is, thus, made up of two components: (1) an increase in exposed cleavage surfaces along the terraces of width $w/\cos\varphi$ and the bridging cleavage-like processes that connect the terraces, and; (2) the grain boundary shear work expanded when a relative displacement δ_{Bc} takes place across the grain boundary plane. This gives

$$\Delta U = G_{ICA}\Delta A + \Delta W_p \tag{6-1}$$

$$\Delta A = \Delta x \frac{w}{(\cos\psi)^2}[\sin\varphi + \cos\varphi] \tag{6-2}$$

is the increment of cleavage surface with increasing average penetration distance Δx of the crack into grain B and where the tilt angle ψ and twist angle φ account for the geometrical projection effects of the actual cleavage surface area on the mean crack advance plane at the extension of the cleavage plane of grain A. We assume that the actual specific work of separation across this cleavage area remains to be G_{ICA} as in grain A. The increment of work of separation of the grain boundary islands sheared by the penetrating crack in grain B can be stated as:

$$\Delta W_p = k\frac{\beta w^2 \Delta x}{4} \cdot \frac{\sin\varphi\cos\varphi}{\cos\psi} \tag{6-3}$$

where k is the effective shear strength of the grain boundary. At the point of maximum resistance of the boundary when Δx reaches Δx_c and δ_B reaches $\delta_{Bc} = \beta\,\Delta x_c$, the increment of expanded energy becomes

$$\Delta U = G_{ICA} w \Delta x_c \cdot \frac{1}{(\cos\psi)^2}(\sin\varphi + \cos\varphi) + k\frac{\beta w^2 \Delta x_c}{4} \cdot \frac{\sin\varphi\cos\varphi}{\cos\psi}, \tag{6-4}$$

and the overall grain boundary break-through resistance becomes

$$G_{\mathrm{ICGB}} = \frac{\Delta U}{w\Delta x_c} = G_{\mathrm{ICA}}\frac{1}{(\cos\psi)^2}(\sin\varphi + \cos\varphi) + \frac{k\beta w}{4}\cdot\frac{\sin\varphi\cos\varphi}{\cos\psi}, \tag{6-5}$$

giving the peak stress intensity to break-through of a grain boundary by pure cleavage

$$K_{\mathrm{ICGB}} = \sqrt{\frac{EG_{\mathrm{ICGB}}}{(1-\nu^2)}} \tag{6-6}$$

Finally, the differential cracking resistance of a grain boundary $\Delta K_{\mathrm{ICGB}} = K_{\mathrm{ICGB}} - K_{\mathrm{ICA}}$, normalized with K_{ICA} gives a relatively simple expression as:

$$\frac{\Delta K_{\mathrm{ICGB}}}{K_{\mathrm{ICA}}} = \sqrt{\frac{1}{(\cos\psi)^2}(\sin\varphi + \cos\varphi) + C\frac{\sin\varphi\cos\varphi}{\cos\psi}} - 1 \tag{6-7}$$

where the constant C

$$C = \frac{\beta k w}{4G_{\mathrm{ICA}}} \tag{6-8}$$

is a material constant collecting together both some well-known and some ill-defined factors, such as the coefficient β. The rest of Eqn. (6-7) is of a purely geometrical nature. We note that when both ψ and φ go to zero Eqn. (6-7) goes to zero, as it should.

We consider the parameter C as adjustable to obtain the best fit between the model and the experimental measurements for the 17 different bi-crystal experiments by using experiment 13 with a contribution of substantial tilt and twist to fix C at 0.25. With this single fitting constant we have calculated the predictions of Eqn. (6-7) for all 17 cases and compared the model predictions with the experimental measurements. The results given as a ratio $(\Delta K_{\mathrm{ICGB}})_{\mathrm{E}}/(\Delta K_{\mathrm{ICGB}})_{\mathrm{C}}$ of the experimental measurements to the computed values are

presented in Table 2.2. While there is some scatter, with the largest departure from unity being about 13%, the overall average ratio was found to be:

$$(\Delta K_{ICGB})_E/(\Delta K_{ICGB})_C = 1.00 \pm 0.05 \qquad (6\text{-}9)$$

which we consider to be quite good.

Using the most probable value of 2.5×10^{-6}m for w, $k = Y/\sqrt{3} = 0.144$ GPa, and G_{ICA} = 850 J/m^2, we estimate β to be 2.0, which is quite acceptable.

Pursuing the model further, we consider Eqn. (6-7) also as a framework to calculate the boundary penetration resistance above the change to mixed-cleavage transition where considerable additional dissipative work is being done in the sigmoidal plastic bending of the ligaments connecting the individual cleavage strips in grain *B*. We consider this work formally associated with the grain boundary shear work, ΔW_p, of Eqns. (6-1) and (6-3). This is possible by a reinterpretation of the non-dimensional constant C in Eqns. (6-7) and (6-8). A new choice of C at a level of 1.70 also successfully takes account of the considerably larger higher-temperature break-through toughnesses for the two orientations "C" and "D" represented in Table 2.3.

Based on observations in bi-crystal experiments, the model discussed in this chapter demonstrates that the break-through of cleavage cracks across high-angle grain boundaries is a topologically relatively simple process in the range well below the usual ductile-to-brittle fracture transition. In *Fe-2%Si* the latter transition in polycrystalline samples occurs for the usual compact experiment geometry at a temperature around 250C. Thus, at -20C where most of our

bi-crystal experiments were performed the alloy under consideration is very brittle, and the specific role of grain boundaries becomes relatively easily understandable. In our experiments we have found that the work of fracture (critical energy release rate) G_{ICA} of the well-aligned starter grain A was in the range of 850J/m^2, which is quite substantial. This high value of dissipated fracture work was explained by the presence of a longer-range traction/separation relation arising from the fragmentation of the cleavage crack plane into parallel strips at different levels advancing separately requiring additional plastic flow due to bridging inside a process zone advancing with the crack (Chapter 5). Clearly, these fitting exercises demonstrate only a proper framework for considering the relative ordering of the measured parameters and does not constitute a fully definitive model.

CHAPTER 7

MODELS FOR CLEAVAGE CRACK PROPAGATING ACROSS A FIELD OF GRAINS

7.1 Topological features of fracture surfaces in polycrystalline specimens

A subject of primary interest in the present study was the topology of the forms of percolation of a cleavage fracture front through a field of grains and the overall fracture resistance that arises from this process. For this purpose, a number of Fe-2%Si compact fracture mechanics samples were prepared and were fractured in the manner of ASTM standard E339. While the very coarse-grained nature of this material resulted in considerable scatter in the determination of fracture toughness, as we indicated in Chapter 3, this was particularly convenient for the detailed study of the percolation of the cleavage front among grains. Such compact fracture experiments were performed at –30C, 0C and 21C. Here we will follow only the features of the percolation of the crack front in the experiment carried out in the pure cleavage realm of –30C. During the experiment the crack opening load and the crack opening displacement were recorded. As in other such experiments, it was noted that the crack advanced in a jerky manner, involving, on the average, 3 jumps before full unstable separation of the entire specimen occurred. While plastic dissipation at the arrest fronts was slight, for each jerky advance it was relatively easy to identify the fronts of crack arrest through inspection of the field of cleaved grains after the experiment was over, and from the increased compliance of the compact fracture specimen.

Identification of the actual mode of advance of the cleavage front among grains was readily possible, by studying the patterns of cleavage river markings inside grains. While this process could not identify the position of the crack front at given times, it did identify the actual percolation features of the local crack advance from grain to grain. Several detailed features of this advance proved to be interesting and amenable to some detailed modeling as we present in Section 7.3 below.

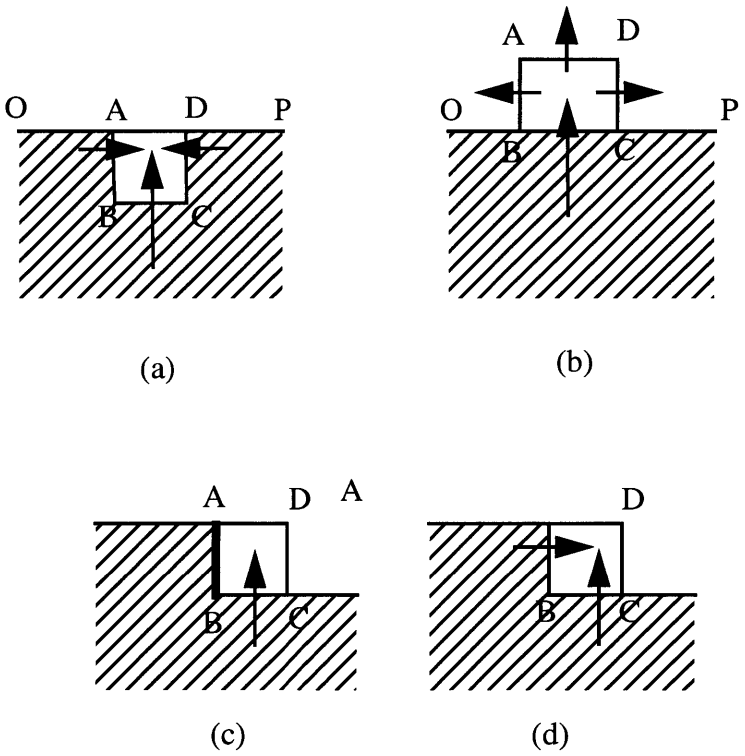

Fig.7-1 Various modes of entry of a cleavage front into individual grains: a) penetration into an exposed grain; b) penetration into a grain through a particularly weak boundary; c) and d) cracks entering into grains with an exposed corner.

On the basis of the earlier bi-crystal study discussed in Chapter 2 and Chapter 6, where it was established that the primary resistance to crack advance is the resistance of boundaries to the passage of cleavage cracks across them, it was assumed in the present study also that once a cleavage

Fig.7-2 Macrograph of a fracture surface of a compact fracture specimen of very coarse grained Fe-2%Si alloy (-30°C).

crack penetrated into a grain it would traverse through it nearly instantaneously in comparison to the time spent in overcoming the grain boundaries. In a jerky advance step the crack front traverses across a significant number of grains in very close succession, making inertial effects likely to be important in this process. Nevertheless, in our considerations we ignore these and treat the crack advance as quasi-static. In this idealization, at any stage the further advance of the crack will depend on the local distribution of the momentary quasi-static crack tip stress intensity K_I. As a further step in the idealization, we note that because of the random misorientation of cracked grains immediately behind the crack front, the cracked cleavage planes will be misoriented in relation to the average plane of cracking, making the "driving forces" at the crack front to be of mixed mode. In our consideration, however, we also ignore this mixed mode nature of advance and consider only the distribution of the local crack tip mode I stress intensity, K_I, as if the cracked portion of material immediately behind the crack front was flat and in the average plane of the advancing crack. Clearly, these simplifications compromise the accuracy of the model that we present in Section 7.3, with the consequences becoming observable in comparison between model results and actual observations. Finally, the advance of the crack front at any particular grain boundary along the front will depend both on the driving forces and the fracture resistance of the specific boundary. Noting these provisos, a number of important observations are still possible on the topology of the crack advance. These we enumerate below.

We consider a generic square-shaped grain ABCD in the path of the crack front as shown in the cases depicted in Fig.7-1, where the shaded region represents the cracked portions immediately behind the crack front. In the case of Fig.7-1a the crack front encounters and exposes a grain that

will be subjected to a significant concentration of local stress intensity K_I, it then enters the grain from the exposed boundaries AB, BC, and CD simultaneously, or in quick succession. In the case of Fig.7-1b the crack front encounters a particularly weak grain boundary BC and penetrates through it. While the stress intensity along boundaries BA, AD and DC will be significantly lower because of the re-entrant nature of the initial penetration, the front may still penetrate theses boundaries and fan-out from there toward the front and the sides of the grain if the strength of these boundaries are lower than the adjoining boundaries OB and CP along the crack front. When the generic grain occupies a corner position along the crack front as shown in Figs.7-1c and 7-1d, the corner will again be subjected to a significant excess of the driving force. In this case several possibilities were found to occur. If boundary AB is tougher than the average, the crack will, as depicted by Fig.7-1c, penetrate the grain through the boundary BC first and shear boundary AB later which would then be subjected to a significant mode III driving force. In most cases, however, if the toughness of boundaries AB and BC are close together the crack front can penetrate the grain through these boundaries in quick succession as depicted in Fig.7-1d. Other more complex penetrations were also observed occasionally. Whenever the generic grain is penetrated from more than one side more complex river markings are produced in the grain, making a unique determination of sequences of penetration difficult. While all these modes of cracking of grains were observed, the dominant process was the entry of the main crack into a particular grain across only one boundary as we discuss in Section 7.2 below.

In some instances, as already mentioned above, a particular grain boundary may be too tough to be penetrated by the main crack front. Then the front will surround the grain and the "recalcitrant" grain boundary, and leave it behind to be subjected to high levels of combined mode II and mode

Table 7.1. The tilt and twist misorientations of principal cleavage facets of 78 individual grains in the compact fracture sample of Fig.7-4 referred to external axes.

Grain Number	1	2	3	4	5	6	7	8	9	10	11	12	13	14
φ_0 (°)	-8	-10	11	27	0	-1	-4	8	-15	-4	-6	41	16	17
ψ_0 (°)	12	43	32	-2	-1	-1	-21	-11	-10	-7	-4	9	-22	-32
Grain Number	15	16	17	18	19	20	21	22	23	24	25	26	27	28
φ_0 (°)	12	7	10	4	-20	-18	-15	12	-27	-4	8	6	22	25
ψ_0 (°)	18	-41	14	2	-4	-9	28	44	17	-33	-16	-44	-40	-38
Grain Number	29	30	31	32	33	34	35	36	37	38	39	40	41	42
φ_0 (°)	-5	-8	-10	-4	13	3	-15	7	16	38	23	32	25	-8
ψ_0 (°)	-5	45	45	36	-15	-18	-24	-20	-2	3	-16	-4	28	-2
Grain Number	43	44	45	46	47	48	49	50	51	52	53	54	55	56
φ_0 (°)	-11	6	10	18	-26	-3	-8	5	-11	7	-5	-4	-28	5
ψ_0 (°)	9	3	1	-6	-2	30	11	28	-22	-26	0	0	33	10
Grain Number	57	58	59	60	61	62	63	64	65	66	67	68	69	70
φ_0 (°)	3	-37	-21	4	5	27	-11	13	14	11	-7	1	7	-5
ψ_0 (°)	-2	-8	11	15	13	40	-28	-26	-1	-12	-14	5	-15	-4
Grain Number	71	72	73	74	75	76	77	78						
φ_0 (°)	5	8	3	3	-1	7	16	7						
ψ_0 (°)	-1	31	6	4	8	-19	-16	-4						

III, resulting in eventual overcoming of the boundary by a combination of shear deformation and fracture. Our estimates indicate that the contribution to the overall work of fracture of such tough grain boundaries is significant, and that roughly a fraction of 10%-15% of grain boundary line length exposed by the penetrating crack front is of this type.

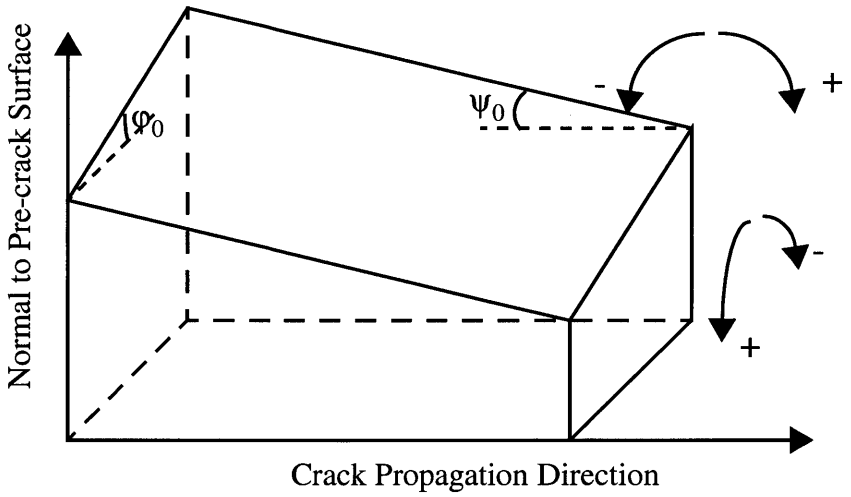

Fig.7-3 Orientation relationship of cleavage facets in individual grains, relative to external specimen axes.

7.2 A detailed history of percolation of a cleavage front through a field of grains

We now consider in some detail the percolation of a specific cleavage front through a field of very coarse grains in a standard compact sample fractured at –30C. Figure 7-2 shows a macrograph of the fracture surface in this sample (DC01) of Fe-2%Si alloy. River markings in some grains are discernible in the figure but were very clearly observable in all cases under a magnification of about 50. In this particular sample 78 individual grains were identified between the initial crack tip of the compact fracture sample, along the left border, and a final region close to the other bor-

der of the sample. Some grains in the upper and lower right side of the field were not identified as well as some grains at the far right edge. In these regions the crack had been growing already unstably where further details were not of interest. The individual tilt and twist angles of the principal cleavage plane of each grain relative to the external borders of the sample were measured with the special modified stereo microscope illustrated in Fig.3-1. These angles, in degrees, are listed in Table 7.1 for all the 78 grains that were identified. Figure 7-3 depicts how the orientational relations of these tilt and twist angles, ψ_0 and φ_0, relative to the normal of the median plane to the crack and the crack growth direction were obtained.

Figure 7-4 shows a cleavage front percolation map of the crack penetrations into each grain in this sample. The left border of the figure is the initial macro crack tip cut into the compact fracture sample. The solid arrows, based on a detailed study of the river markings fanning-out from grain boundaries, indicate the direction from which the individual grain was penetrated. While this penetration was in many instances from only one direction, there was a number of grains that showed multiplicities of river markings, indicating simultaneous, or nearly simultaneous, penetration of the grain from more than one direction. The arrow map shows the spatially complex form of the percolation process. Two specific fronts, A-A and B-B, have been identified by heavy zig-zag lines. These are two fronts of arrest of the jerkily advancing crack, as best as they could be related to the externally monitored crack opening force/displacement information. The final propagation of the crack front beyond the B-B line was in one unstable step.

As explained in more detail in the crack front advance model in Section 7.3, it was of interest to glean some insight into the further advance of the crack front from lines A-A and B-B. For this

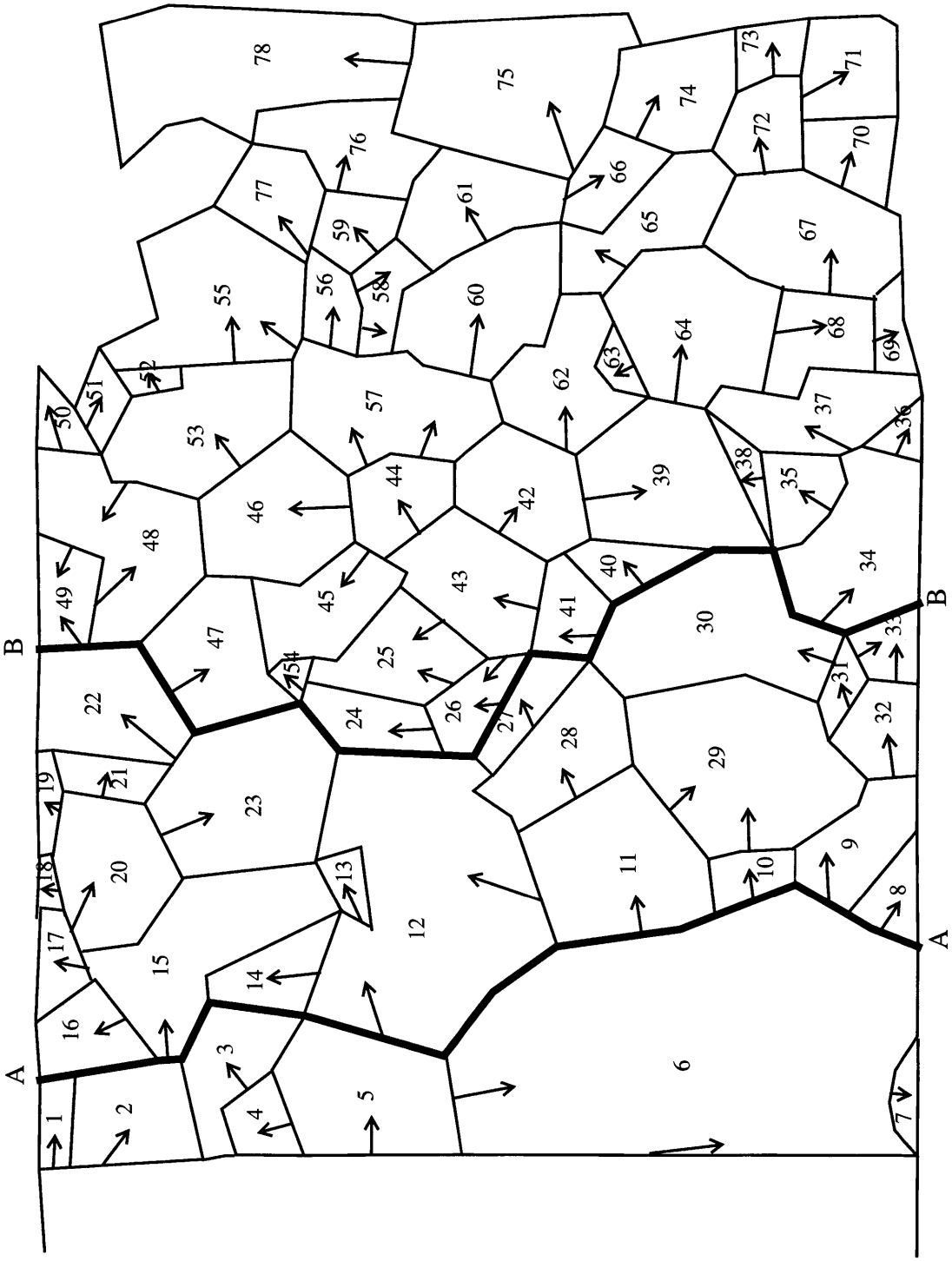

Fig.7-4 The cleavage fracture percolation map through the grains of the sample shown in Fig.7-2, showing also two crack arrest fronts A-A and B-B.

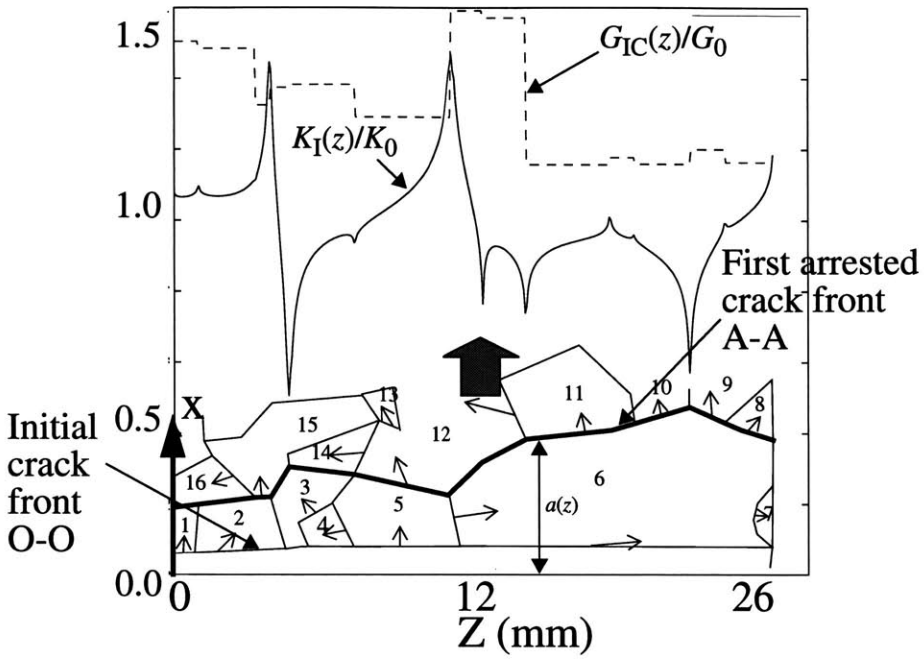

(a) Crack front A-A

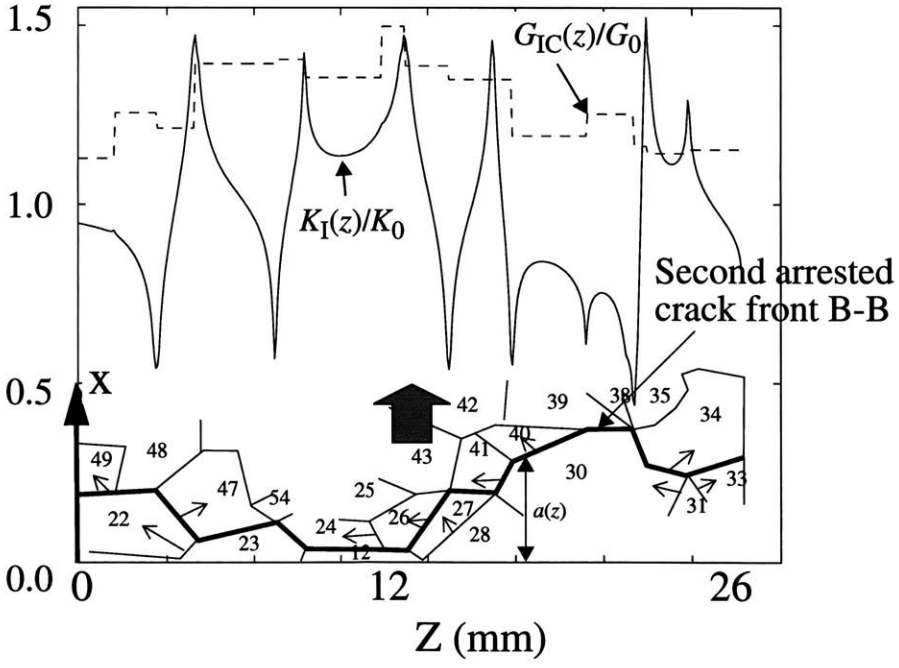

(b) Crack front B-B

Fig.7-5 The calculated distribution of local stress intensity factors K_I along the fracture fronts A-A and B-B.

purpose the local mode I crack driving force, K_I, was calculated along the jagged arrested crack front using Rice's (1985) variational method according to the relation

$$K(z) = K_0[z;a(z)] + \frac{1}{2\pi}\int \frac{K_0[z';a(z)] \cdot [a(z') - a(z)]}{(z' - z)^2} dz' \qquad (7\text{-}1)$$

where $a(z)$ is the crack length at location z along the direction parallel to the sample thickness and roughly parallel to the arrested crack front, $K_0[z; a(z)]$ is the local mode I stress intensity factor at location z in relation to a virtual reference straight crack-front-segment at $a(z)$ under the same remote load. In the evaluation of the integral the principal value was taken, and the upper and lower integration limits were taken as 0 and h, respectively, where h is the specimen thickness.The result of such an evaluation is shown in Figs.7-5a and 7-5b for the crack fronts A-A and B-B respectively. The cuspy contours indicate the distribution of the local $K_I(z)/K_0$ normalized with the overall stress intensity factor based on the increased specimen compliance. It is seen that the local crack driving forces for further crack advance are highest at the exposed corners while re-entrant corners are protected, as can be expected. The actual local choice for further penetration of the crack front depends also on the fracture resistance of the individual grain boundaries along the front. Nevertheless, there is a satisfactory correspondence between the level of the driving force and the direction of the further crack advance. The dotted stepped contour across each grain boundary represents the actual local normalized energy release rate (or work of fracture) for a virtual extension of the crack across the specific grain boundaries determinable from the character of the grain boundary.

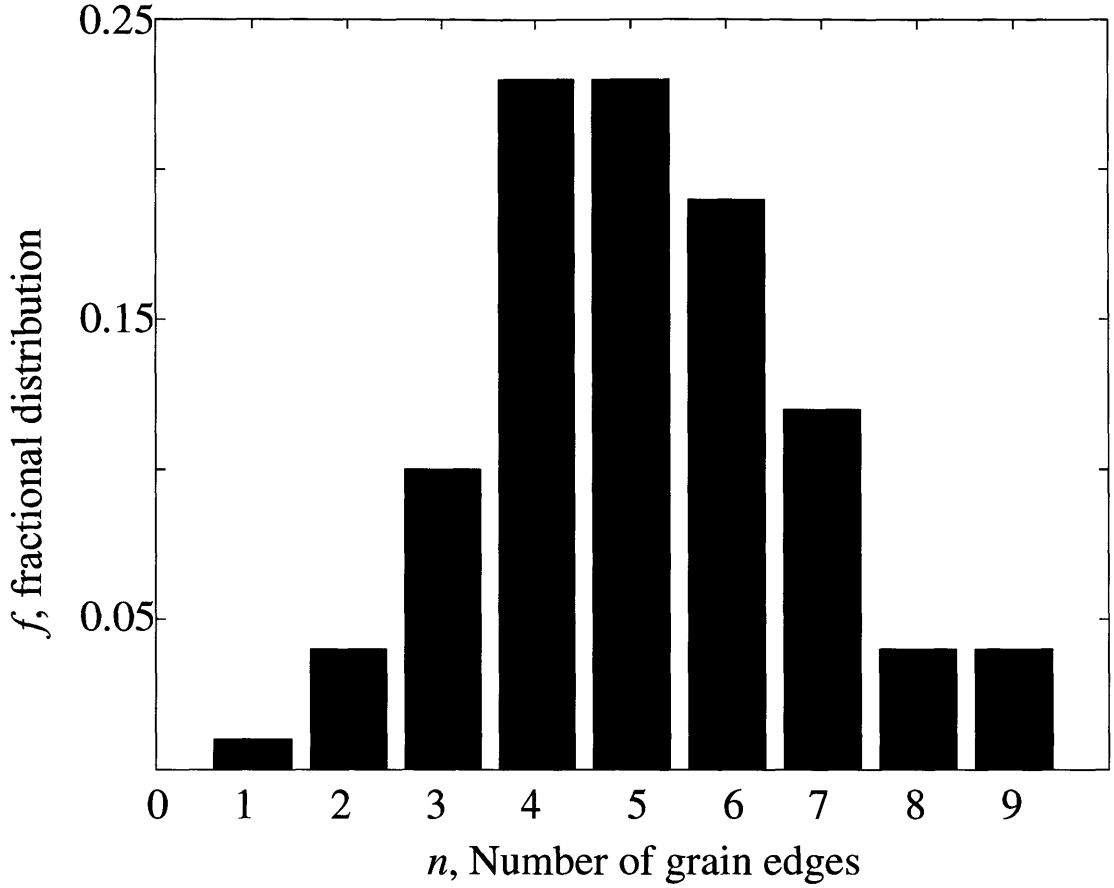

Fig.7-6 Histogram showing the distribution of numbers of grain edges in the fracture field of Fig.7-4, not counting grain edges bounded by free surfaces.

A number of statistical observations related to the percolation map of Fig.7-4 are of interest. Many of the projected grain boundary lines are kinky and some of them have substantial curvature indicating that the grain boundary energy was far from isotropic. Not counting the edges of grains that were free surfaces, the 78 grains possessed 397 edges indicating that the average number of edges of a typical grain was 5.09 rather than 6.0. The frequency distribution of numbers of edges of grains is given in Fig.7-6. The arrow map of Fig.7-4 indicates that of the 78 grains, 67 were penetrated only through one grain boundary, while 11 were penetrated from 2 grain boundaries.

This indicates that only 89 grain boundary penetrations governed the form of percolation of the cleavage front across the grains in the particular field. Since each of the 397 boundaries are shared by two grains, only a fraction of 0.45 of the boundaries had played a role in the percolation map and the remaining fraction of 0.55 of boundaries separate already-cracked grains, and must be separated by a mixture of modes II and III involving a combination of plastic shear and shear fracture. Clearly, of the relatively small number of grains that take part in the percolation process, fully 8% of grain edges in the field represented free borders. This makes the statistical information not quite representative of a large fracture surface in a small-grained polycrystalline sample. Nevertheless, this information will be useful in reaching some overall conclusions, which we will develop in Section 7.4.

7.3 Modeling the percolation of cleavage fracture fronts through a field of grains

A special program was developed to model the percolation of a cleavage front in polycrystalline material. The principal assumptions of the model were outlined in Section 7.1 above. The specific grain structure used in the model was that of the compact fracture specimen DC01 of the Fe-2%Si alloy fractured at -30C and described in detail in Section 7.2 above. The size and shape of each grain was taken from the macrograph of Fig.7-2 and the graphical depiction of it in Fig.7-4. The required misorientation angles of the most appropriate cleavage planes of each grain were those listed in Table 7.1.

The initial straight crack front is given by the left border of the grain field map of Fig.7-4. The plane of the pre-crack was considered to be in the median plane of the compact specimen. At the

beginning of each propagation step, the effective local crack driving force K_i and the local fracture resistance $G_{IC}^{(i)}$ of each individual grain boundary i (i = 1, 2...) at the crack front were calculated. The effective crack driving force K_i was taken to be the line average of the local stress intensity factor $K(z)$ along the part of the crack front at the grain boundary of interest. The first-order variation method developed by Rice (1985) was used to calculate $K(z)$, according to the expression of Eqn.(7-1) given in Section 7.2 above. In the numerical integration along the whole crack front, Romberg algorithm was used (Dahlquist and Bjorck, 1974), which is an application of Richardson's extrapolation to obtain an accurate numerical solution by combining several less accurate solutions of trapezoidal rule with different step lengths.

The local fracture resistance G_{ICB} of an individual grain boundary used in the model was calculated according to a relationship developed for bi-crystal grain boundaries in a previous study for a Fe-3%Si alloy (Chapter 6) given by:

$$\frac{G_{ICGB}}{G_{IC}} = \frac{1}{(\cos\psi)^2}(\sin\varphi + \cos\varphi) + C \cdot \frac{\sin\varphi\cos\varphi}{\cos\psi} \qquad (7\text{-}2)$$

where G_{IC} is the average work of cleavage fracture inside individual grains and C is a material constant combining some geometrical features of the topography of the cleavage surface of a grain interior with the shear resistance of the boundary, leading to an estimated value of $C = 0.25$ according to a best fit to experimental measurements for a wide range of tilt and twist angles of cleavage planes across a grain boundary. The angles ψ and φ are tilt and twist angles of cleavage planes of the adjoining grains across the shared grain boundary and the orientation of

the cleavage surface in the grain to be penetrated by the crack front, respectively. These angles are obtained from the external angles φ_0 and ψ_0 reported in Table II by expressions:

$$\tan\psi = \frac{l_1\cot\varphi_0 + l_2\cot\psi_0 + l_3}{n_1\cot\varphi_0 + n_2\cot\psi_0 + n_3} \tag{7-3a}$$

$$\tan\varphi = \frac{m_1\cot\varphi_0 + m_2\cot\psi_0 + m_3}{n_1\cot\varphi_0 + n_2\cot\psi_0 + n_3} \tag{7-3b}$$

where

$$l_1 = \cos\psi_1\cos\alpha - \cos\varphi_1\sin\psi_1\sin\alpha \tag{7-4a}$$

$$l_2 = -\cos\psi_1\sin\alpha - \cos\varphi_1\sin\psi_1\cos\alpha \tag{7-4b}$$

$$l_3 = \sin\varphi_1\sin\psi_1 \tag{7-4c}$$

$$m_1 = \sin\psi_1\cos\alpha + \cos\varphi_1\cos\psi_1\sin\alpha \tag{7-4d}$$

$$m_2 = -\sin\psi_1\sin\alpha + \cos\varphi_1\cos\psi_1\cos\alpha \tag{7-4e}$$

$$m_3 = -\sin\varphi_1\sin\psi_1 \tag{7-4f}$$

$$n_1 = \sin\varphi_1\sin\alpha,\ n_2 = \sin\varphi_1\cos\alpha,\ n_3 = \cos\varphi_1 \tag{7-4g}$$

with α being the angle between the grain boundary line on the fracture plane and the z-axis, and φ_1 and ψ_1 being the twist and tilt angles of the cracked grain immediately behind the crack front.

The ratio of $K_i/K_{IC}^{(i)}$ (where $K_{IC}^{(i)} = \sqrt{\frac{EG_{IC}^{(i)}}{(1-\nu^2)}}$) of each grain boundary along the crack front was considered and the grain boundary with the largest value of the ratio was taken as the one to be penetrated through first by the propagating crack. A factor Q was determined which makes this largest value unity, and was then used to determine the overall applied stress intensity factor K_I on

the global sample to advance the crack front through the grain. The propagation of the cleavage crack inside the grain was assumed to be instantaneous, advancing the crack front in the grain of interest. After the grain under consideration was cracked, a new crack front was formed by replacing locally the penetrated grain boundary by the boundaries of the same grain that were not at the initial crack front. Then, the K_i's and $K_{IC}^{(i)}$'s along the new crack front were calculated and the similar procedure was repeated until all the grains in the specimen were cracked. This procedure established the chronology of percolation of the crack front through the collection of grains under the provisos of ignoring inertial effects and possible modes II and III as stated above. Based on this procedure, a fracture map was produced and is indicated by the arrows in Fig.7-7 for each grain. When compared with the experimental arrow map of Fig.7-4, it is clear that for the first several columns of grains, the model results matched quite well the experimental results. About 70% of the arrows were predicted correctly. However, with continued propagation of the crack, accumulating errors and the increasing complexity of the crack front shape made the model results increasingly less accurate relative to the experimental observations. In the last several columns of grains, only less than 10% of arrows were predicted correctly. This eventual lack of agreement is attributed primarily to the fact that the local crack driving force at grain boundaries is in reality of mixed mode and not merely of the mode I type, and secondarily to the fact that in this terminal sweep of the cleavage front quasi-static conditions will no longer prevail. Since the crack growth becomes unstable beyond the B-B front this eventual lack of agreement is not of importance.

7.4 Model of total work of cleavage through a field of grains

In Section 7.3 we considered only a model of the chronology of the percolation of the cleavage process through the field of grains for comparison with the observed percolation-arrow-map of Fig.7-4. In this section we develop a model to account for the entire work of cleavage fracture in the pure-cleavage (PC) domain at very low temperature where additional plastic dissipation is minimal, but shear fractures along bridging grain boundaries become important. We then project this model to the range of mixed-cleavage (MC) above the pure-cleavage to mixed-cleavage (PC/ MC) fracture transition.

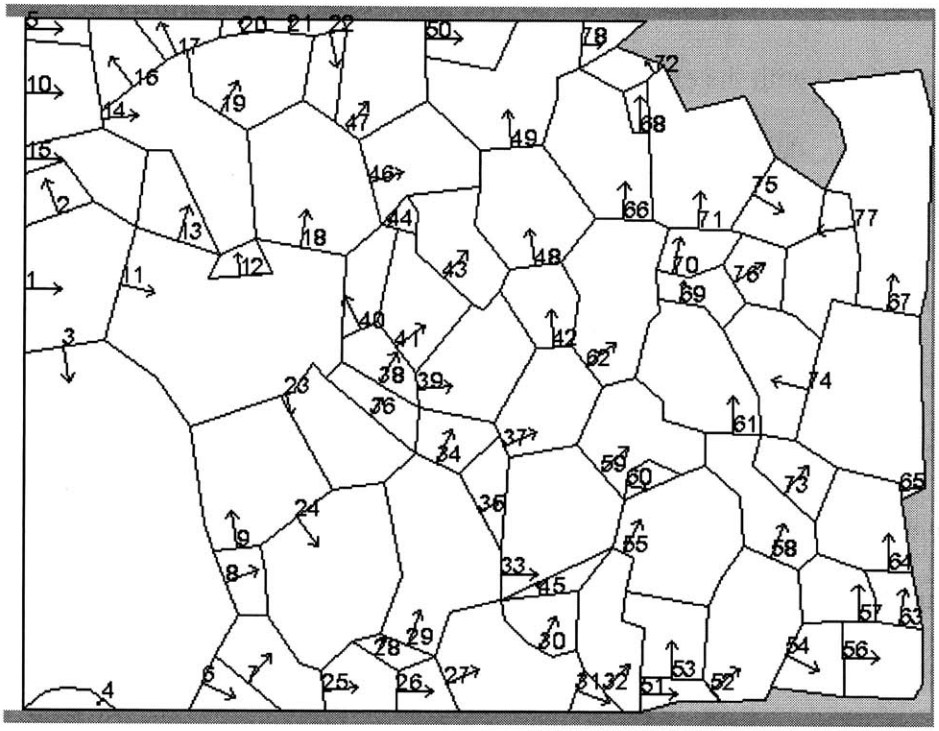

Fig.7-7 Computed cleavage fracture percolation map using information on grain boundary resistance determined by Eqn.(7-2).

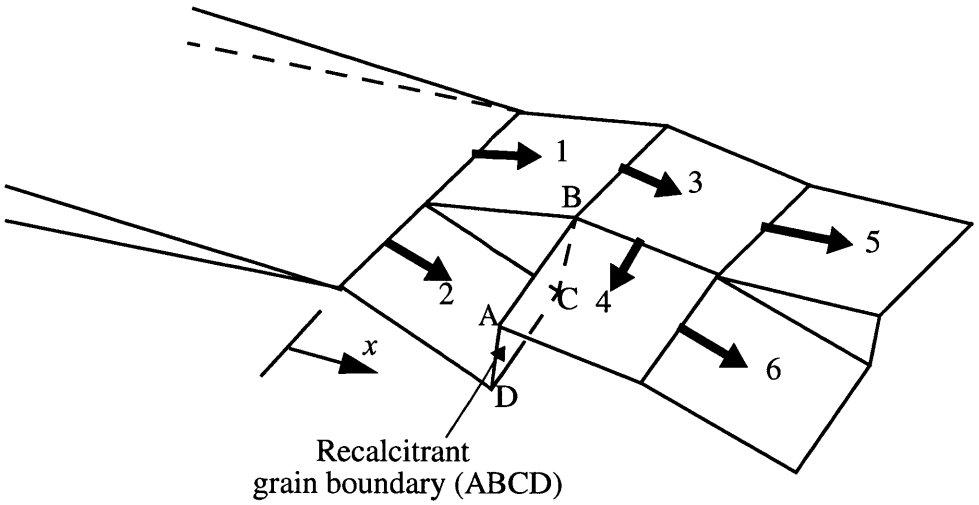

(a)

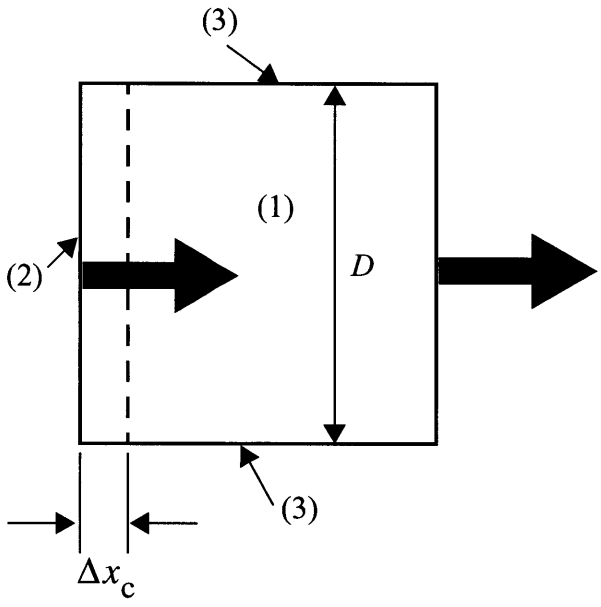

(b)

Fig.7-8 a) A schematic view of the types of boundaries overcome by the cleavage front. Boundaries with emanating arrows are those that govern the form of penetration of the fracture front from grain to grain. Boundaries between 1-2, 5-6, and 2-4, in various measure, require extensive fracture work to bridge primary cleavage facets; b) simplified field in a generic square grain: (1) cleavage work inside grain; (2) work of fracture for going through the principal boundary controlling the percolation process; (3) boundaries requiring large amount of bridging fracture work by plastic shear and cleavage-like separation.

We base our model on the basic observations described in Section 7.2 which indicated that in the majority of cases (86% of the time) the cleavage front enters a specific grain from only one neighboring grain. Figure 7-8a shows a basic set of processes necessary to account for the overall work of cleavage where we idealize outlines of individual grains as square shaped. The arrows show a scheme of spreading of the cleavage front and the boundaries from which the arrows emanate. The spreading requires a special scenario of penetration of a cleavage front across a boundary separating two grains with a combination of tilt and twist misorientation of the cleavage planes across the boundary plane. This specific scenario and the associated resistance of the boundary to the penetration of the cleavage front across it was discussed in detail by us earlier (Chapter 6).

We identify three separate and distinct contributions to the overall cleavage work per unit area of the projected median macro crack plane, that we view as the extension of the plane of the cleavage crack depicted in Fig.7-8a. The first contribution is the cleavage work across the faces of the grains 1-6 in the figure, where each cleavage plane (j) has a specific tilt, ψ_0^j, and twist φ_0^j misorientation angle with respect to the median macro crack plane. These angles are listed in Table II for the specific cases of grains shown in Fig.7-4, that we will study. The second contribution is the fracture work across the primary boundaries of percolation of the cleavage front, i.e. those from which the arrows emanate in Fig.7-8a. This work of break-through of the primary boundaries was discussed in detail in a previous study referred to earlier (Chapter 6). The third contribution is the subsequent work of separation by a combination of some plastic shear and shear fracture along the boundaries between adjacent grains that have already been cleaved apart, such as the boundaries between grains 1-2, 5-6, and 2-4 depicted in Fig.7-8a. Of

these, the boundary between 2-4 might be a tougher-than-average recalcitrant boundary that gives way after it is fully surrounded by cleaved grains. For ease of accounting we depict these three contributions for a generic square grain in Fig.7-8b, where the three contributions to the cleavage fracture work are associated with the corresponding numbers.

The fracture work across grain faces is taken as

$$W_1 = \frac{G_{IC}}{\cos\psi_0^j \cos\varphi_0^j}(C_s D^2) \tag{7-5}$$

where G_{IC} is the specific cleavage work of fracture in a reference grain with cleavage plane exactly parallel to the median macro-cleavage plane, and the angles $\psi_0{}^j$ of tilt and $\varphi_0{}^j$ of twist of the specific grain (*j*) are given relative to the reference axes of Fig.7-3, with $C_s D^2$ being the projected area of the cleavage plane (*j*) of the grain facet on the median plane. In Eqn.(7-5) D is taken as the length of the grain boundary in the reference square grain, and C_s is a constant determined by grain shape, which is unity for square grains and $\frac{2}{\sqrt{3}}$ for hexagonal grains.

The work of fracture associated with the break-through of a grain boundary is taken as

$$W_2 = G_{IC}\left[\frac{1}{(\cos\psi_i)^2}(\sin\varphi_i + \cos\varphi_i) + C \cdot \frac{\sin\varphi_i \cos\varphi_i}{\cos\psi_i}\right] \cdot D\Delta x_c \tag{7-6}$$

where the angles ψ_i and φ_i are the tilt and twist misorientation angles of the cleavage planes across the boundary (*i*) as considered in Eqs.(7-3a) and (7-3b), the dimensionless constant C made up of details of shear displacement along the boundary, *cleavage-like* shear fracture resistance of the boundary, microstructural features of the cleavage river markings inside grains

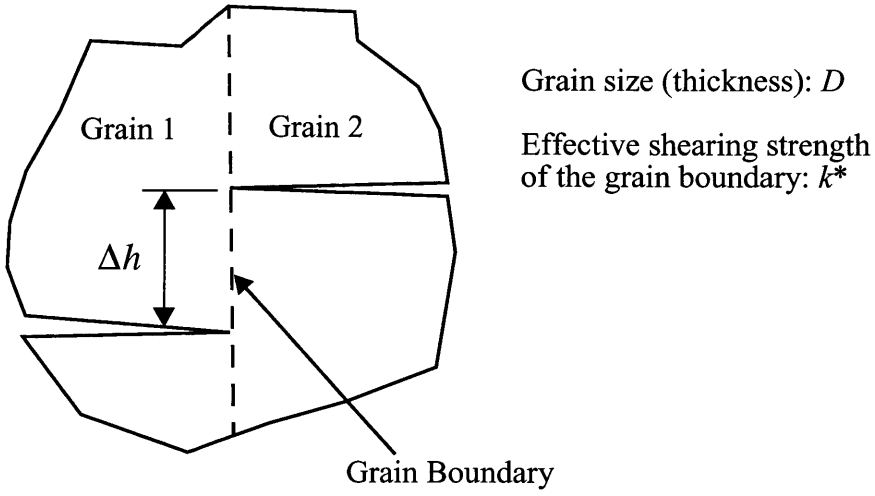

(a)

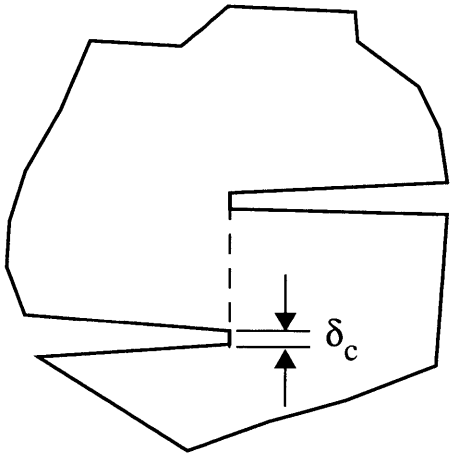

(b)

Fig7-9 Stages of bridging fracture work: a) initial outline of grain boundary bridging primary cleavage facets; b) preparatory plastic crack tip displacement triggering subsequent "cleavage-like" separation.

and some related coefficients, all defined in the previous study of break-through-resistance of bi-crystal boundaries (Chapter 6). It is taken as $C = 0.25$ on the basis of a single principal fit between experimental measurements and the model of that study, in the range of pure cleavage behavior. The distance Δx_c, as depicted in Fig.7-8b, is the critical average distance of penetration of a reference cleavage front across a grain boundary where the boundary break-through resistance reaches its peak value. This model-sensitive distance is considered to scale with the grain size D for small grain sizes but is expected to be constant for very large grains. It will be assigned a specific magnitude in our model as we discuss below.

Finally, the work of separation of the boundaries left behind by the penetrating cleavage front is taken as:

$$W_3 = Dk^*\delta_c\Delta h \tag{7-7}$$

where δ_c is a critical "preparatory" opening displacement of cleavage planes at the grain boundary plane as depicted in Fig.7-9b where the boundary separation acquires a "cleavage-like" shear fracture along the average distance Δh between the cleavage planes of the already cleaved adjoining grains, and k^* is the "cleavage-like" shear fracture resistance of the boundary. The boundary length to be shared by the grains is taken as D rather than $2D$, since each lateral grain boundary of a grain to be sheared is shared by two adjoining grains. Clearly, this process of boundary separation involves a mixture of modes II and III of the "cleavage-like" shear fracture and must also depend on the angle of inclination of the boundary with the median macro crack plane. The micrograph of Fig.7-10 shows the appearance of such a boundary separated by a combination of shear (the major portion with clearly shown shear markings) and a complex

fracture process (identified with the arrow). McClintock (1997) has developed a more detailed model of this bridging shear fracture based on earlier slip line field analysis (McClintock and Clerico, 1980) which results in very similar observations but using a considerably different scenario of separation involving only plastic "shearing off". None of these details which can be expected to be quite model-sensitive and variable from boundary to boundary will be developed further. Rather, as had been done in the previous study of cracking across bi-crystal boundaries, referred to above, we introduce a dimensionless parameter B that normalizes this work of separation with the principal specific cleavage work G_{IC} as

$$B = \frac{k^* \delta_c \xi}{G_{IC}} \tag{7-8}$$

where

$$\xi = \frac{\Delta h}{D} \tag{7-9}$$

is the ratio of the average vertical separation Δh between the cleavage planes of the adjacent grains to the mean (square-shaped) grain size. This latter ratio can be expected to depend on the angles of misorientation between the cleavage planes of the adjoining grains. Moreover, as depicted more realistically in Fig.7-8a, the distance Δh locally should depend on the distance Δx of penetration of the cleavage front across the two adjoining grains and the separation should have a mixed mode character of II and III of fracture as noted above, since none of this detail is realistically amenable to analysis for every boundary, as must be clear, the choice of a single average fitting parameter B becomes very attractive. Thus, combining these three contributions into a single specific cleavage work, G_{ICPC}, of the *polycrystal* median fracture plane, in units of the basic work of cleavage, G_{IC}, of a reference grain of no misorientation gives

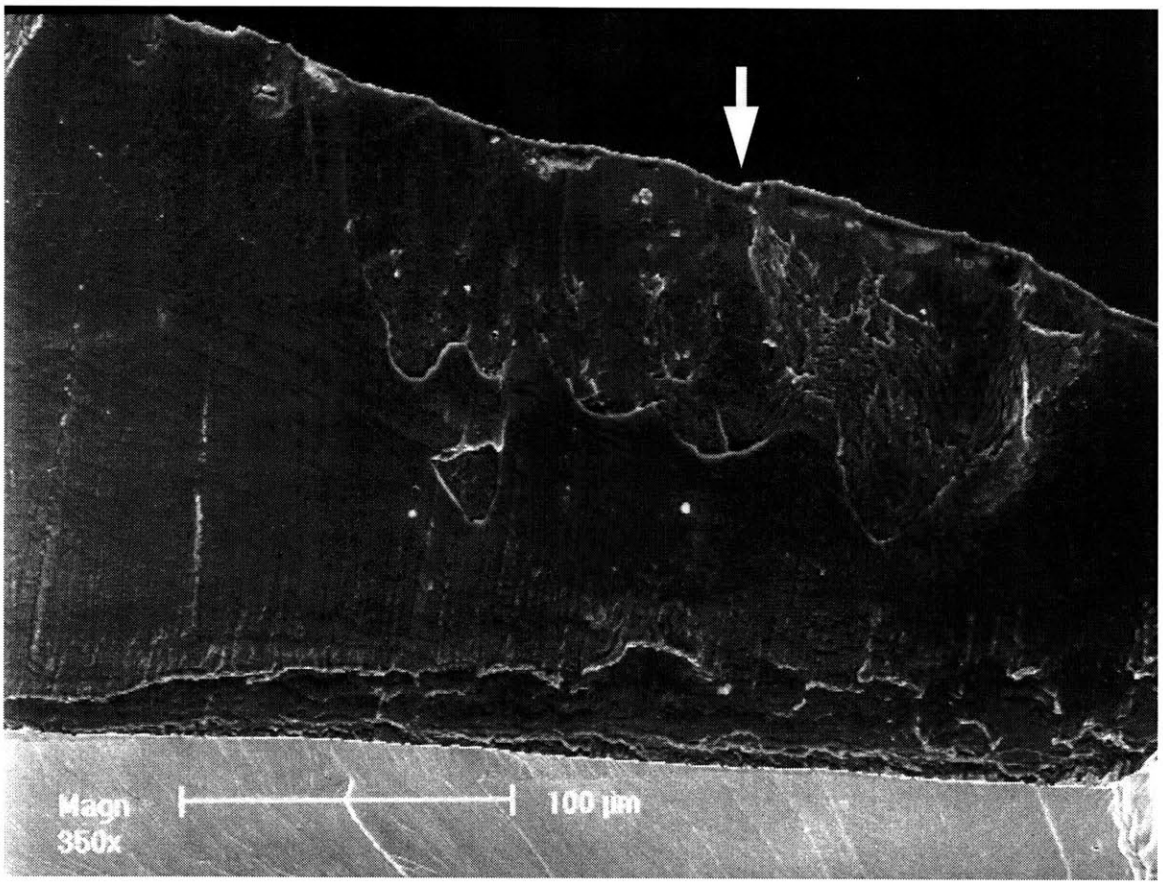

Fig.7-10 SEM micrograph of the surface of separation by shear in a typical boundary connecting two cleaved facets in adjacent grains. Most of the surface shows signs of plastic shearing. Portion identified by an arrow shows a fracture type separation.

$$\frac{G_{ICPC}}{G_{IC}} = \frac{C_s}{\langle \cos\psi_0^j \cos\varphi_0^j \rangle} + \left(\frac{\Delta x_c}{D}\right)\left\langle \left[\frac{1}{(\cos\psi_i)^2}(\sin\varphi_i + \cos\varphi_i) + C \cdot \frac{\sin\varphi_i \cos\varphi_i}{\cos\psi_i}\right]\right\rangle + B \tag{7-10}$$

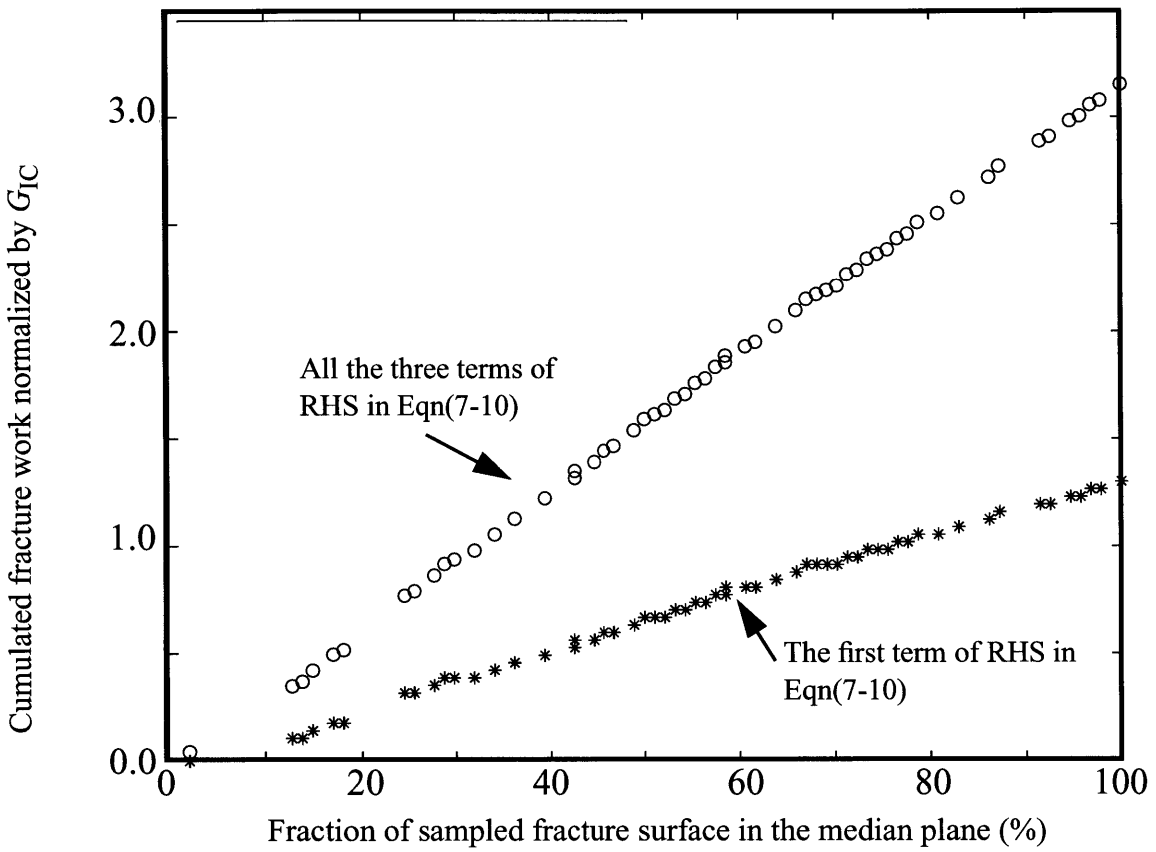

Fig.7-11 Result of computer simulation of overall fracture work for an advancing crack front through the family of grains shown in Fig.15. Stars indicate accumulated fracture work due to cleavage of grain interiors, open circles indicate cumulative fracture work contributed by the severance of the bridging grain boundaries.

where the brackets across the first and second terms on the RHS of Eqn.(7-10) indicate an orientation average of all possible cases of sampling of grains of random orientation. Rather than develop this expression as given, we consider a model of the above ratio for each grain in the specific case of the polycrystal field considered in Fig.7-4 and obtain the cumulative work of

fracture for the quasi-statically advancing cleavage front according to the modeled percolation map of Fig.18. The result of this model, following along the same set of steps developed in Section 7.3 for the determination of the percolation arrow map of Fig.7-7, is shown in Fig.7-11. In the model, the critical penetration depth Δx_c for break-through of a grain boundary was taken as $10\mu m$ for the very coarse-grained material modeled here. Since in the present case the average grain sizes were in the range of 4mm the ratio $\Delta x_c/D$ becomes roughly 0.0025, making the contribution of the second term in Eqn.(7-10) negligible for such large grain size material. As stated above, for very fine grain material, we assume that Δx_c should become proportional to the grain size, where the second term in the RHS of Eqn.(7-10) will make a non-negligible contribution. In the present context if B is chosen as 1.86, the model results would produce a perfect fit to the experimental results. Thus, the experimentally measured $K_{ICPC} \cong 13MPa\sqrt{m}$ of the polycrystal at -30C as indicated in Fig.3-3, while $K_{ICSC} \cong 7.3MPa\sqrt{m}$, as measured in connection with crack arrest experiments in Fe-3%Si alloy (Qiao and Argon, 2002), gives

$$G_{ICPC}/G_{ICSC} = (K_{ICPC}/K_{ICSC})^2 = 3.17 \qquad (7\text{-}11)$$

On the other hand the model results indicate that $(W_1/G_{IC}) = 1.31$, in Eqn.(7-10), and since the contribution of the second term is negligible in the present context, to obtain $(G_{ICPC}/G_{ICSC}) = 3.17$, $W_3/G_{IC} = B$ must be chosen as 1.86. In this connection it is worth noting that the contribution of the cleavage work of the grain interiors is 31% higher than G_{ICSC}, the work of planar fracture, due to the random misorientation of the principal cleavage planes in grains, along the entire fracture surface.

Parenthetically, we note that the choice of the magnitude of the constant B as 1.86, and taking $\delta_c \approx \Delta x_c = 10\mu m$, $\Delta h/D \approx 0.5$ and G_{IC} (= G_{ICSC}) = 230J/m^2, derived from the average fracture toughness of $7.3 MPa\sqrt{m}$, measured in a thermal crack-arrest experiment in single crystals of Fe-3%Si alloy (Chapter 4), would give for the "cleavage-like" shear resistance k^* a value of about 86MPa. This value of k^* is considerably lower than the plastic shear resistance of the alloy at -30C which is estimated to be in the range of 200MPa. This indicates that under the present considerations the shear fracture process along the bridging grain boundaries could have only a minor plastic shear contribution, unlike in the model considered by McClintock and Clerico (1980). However, since there is considerable flexibility in the above estimates and Fig.7-10 shows clear evidence of plastic shear along bridging grain boundaries, a firm conclusion is not possible on which mode of shear is most likely.

7.5 Contribution of grain boundaries to the cleavage resistance

Based on the detailed considerations of the percolation of cleavage fracture across a field of grains in the coarse-grained Fe-2%Si alloy discussed in Section 7.2 and the models of the percolation map and work of fracture developed in Sections 7.3 and 7.4, it becomes possible to state a general expression for the contribution of grain boundaries to the overall work of fracture of a polycrystal in the extreme lower shelf region of fracture, labelled by us as pure cleavage (PC) fracture regime. The expression we propose is a generalization of Eqn.(7-10), benefiting from the numerical model of Section 7.4. For this purpose we re-state Eqn.(7-10) in its final form below as:

$$\frac{G_{ICPC}}{G_{IC}} = \langle \frac{C_s}{\cos\psi_0^j \cos\varphi_0^j} \rangle + \alpha\beta\left(\frac{\Delta x_c}{D}\right)\langle \frac{1}{(\cos\psi_i)^2}(\sin\varphi_i + \cos\varphi_i) + C \cdot \frac{\sin\varphi_i \cos\varphi_i}{\cos\psi_i} \rangle + B$$

(7-12)

In Eqn.(7-12) in the first term on the RHS $C_s = 2/\sqrt{3}$ is a factor correcting for hexagonal-shaped grain facets over the square-shaped grain facets considered in the preliminary rough model; the orientation average of the projection product in brackets is readily evaluated as 1.26 using the data of Table II. In the second term $\alpha = \sqrt{3}$ is the ratio of the average grain diameter to the grain edge length of a hexagonal grain and the factor $\beta = 1.14$ accounts for the fact that in 14% of cases in the simulation a cleavage crack enters a grain through two faces nearly simultaneously; the orientation average of the term in brackets can be taken as 1.61, as the average value of this factor determined in a previous study of cleavage cracking resistance of bi-crystal boundaries (Chapter 6). The ratio $\Delta x_c/D$ in this term remains somewhat elusive since the effective penetration distance Δx_c across a boundary where the peak resistance is encountered can only be conjectured. We have arbitrarily considered this dimension to be around $10\mu m$ for very large grains with $D >> \Delta x_c$. As stated above, however, we consider the ratio $\Delta x_c/D$ to remain a constant for $D \leq 10\ \mu m$. In any event we note that the second term is the only one with a grain size dependence, which becomes negligible for very large grain sizes and becomes grain size independent for medium to small grain size material. Finally, as discussed in Section 7.4 above, we have chosen the magnitude of B as 1.86 based on the model of the rate of increase of cleavage fracture work across a field of coarse grains as given in Fig.7-11. This gives the final form of the cleavage resistance of the polycrystals as:

$$\frac{G_{ICPC}}{G_{IC}} = 1.45 + 3.03(\Delta x_c/D) + 1.86(3.0) \qquad (7\text{-}13a)$$

$$= 3.31+3.03(\Delta x_c/D) \qquad (7\text{-}13b)$$

where G_{IC} is equal to G_{ICSC} of single crystals[1].

We have written Eqn.(7-13a) deliberately in an expanded form to indicate that the contribution to the overall cleavage work of the cleavage of individual grain interiors is substantial and represents roughly 44% of the total work of fracture, as should be clear from Fig.7-11. The second term on the RHS of Eqns.(7-12) and (7-13a) makes a negligible contribution to the total work of fracture for the large grain material that we have considered specifically even though it is this term that governs the selection of the sites for cleavage break-through across grain boundaries. However, because of the tiered nature of the cleavage break-through across grain boundaries described in the earlier bi-crystal study (Chapter 2 and Chapter 6), where the majority of break-throughs had been noted to follow a regular mode of penetration, only a relatively small overall change of fracture area results as the cleavage front crosses a typical grain boundary. The somewhat more substantial contribution (roughly 56%) to the overall work of fracture results from the process of *cleavage-like* shear separation along grain boundaries (Fig.7-9) between primary cleavage cracking facets in adjoining grains, as had already been concluded by McClintock (1997).

---

1. Our analysis above gives $W_1/G_{IC} = 1.45$, while the simulation model gave this ratio as 1.31 as shown in Fig.22. We attribute the discrepancy to the factor C_s which apparently is smaller than $2/\sqrt{3}$, in keeping with the observation in Section 7.2 which gave the average grains to be closer to 5 sided.

Finally, we return to the exploration of a grain size dependence of the cleavage fracture work. While no important grain size dependence is evident in our model beyond the weak and unimportant grain size dependence represented in the second term of the RHS of Eqns.(7-12) and (7-13a, b), we have examined the specific effect experimentally. This dependence was probed through fracture toughness determinations at -20C in the pure cleavage range in 8 coarse-grained samples, in which the average grain size varied between 1.5mm and 6.0mm. The result is given in Fig.7-12. It shows very substantial scatter among the measurements, with no discernible grain size dependence in this narrow range of grain sizes, which is consistent with our model in which the only grain size dependent contribution might conceivably arise for grain sizes in the range of 50-100 microns but should be negligible in the coarse grain size range of 1-10mm, and disappear for very small grain size material if the ratio $\Delta x_c/D$ reaches a constant value asymptotically, as was assumed might be the case.

We note that in our model a certain grain size dependence is still possible on a different interpretation of W_3 in Eqn.(7-7), of the work of separation of the boundaries left behind by the primary cleavage penetrations. In that model the parameter δ_c represented a critical shear displacement along the step height of Δh connecting the cleavage planes. This distance was taken to be a constant, independent of grain size, on the interpretation of it being a preparatory step which initiates an abrupt "cleavage-like" separation, terminating all contact between adjacent faces. If on the other hand the separation were entirely by a plastic shearing-off process along the step height Δh, the parameter δ_c should have been $\Delta h/2$ and grain size dependent. This would make the factor $B = k^*\xi^2 D/2G_{IC}$ defined in Eqn.(7-8), and would introduce a

direct grain size dependence into the last term of Eqn.(7-10). Such a dependence would be in-keeping with the well known direct dependence of the work of separation of ductile fracture, and still have the correct dependence for asymptotic behavior of a monotone decrease in grain size. However, we have insufficient evidence for such pure plastic behavior and prefer the "cleavage-like" separation mode.

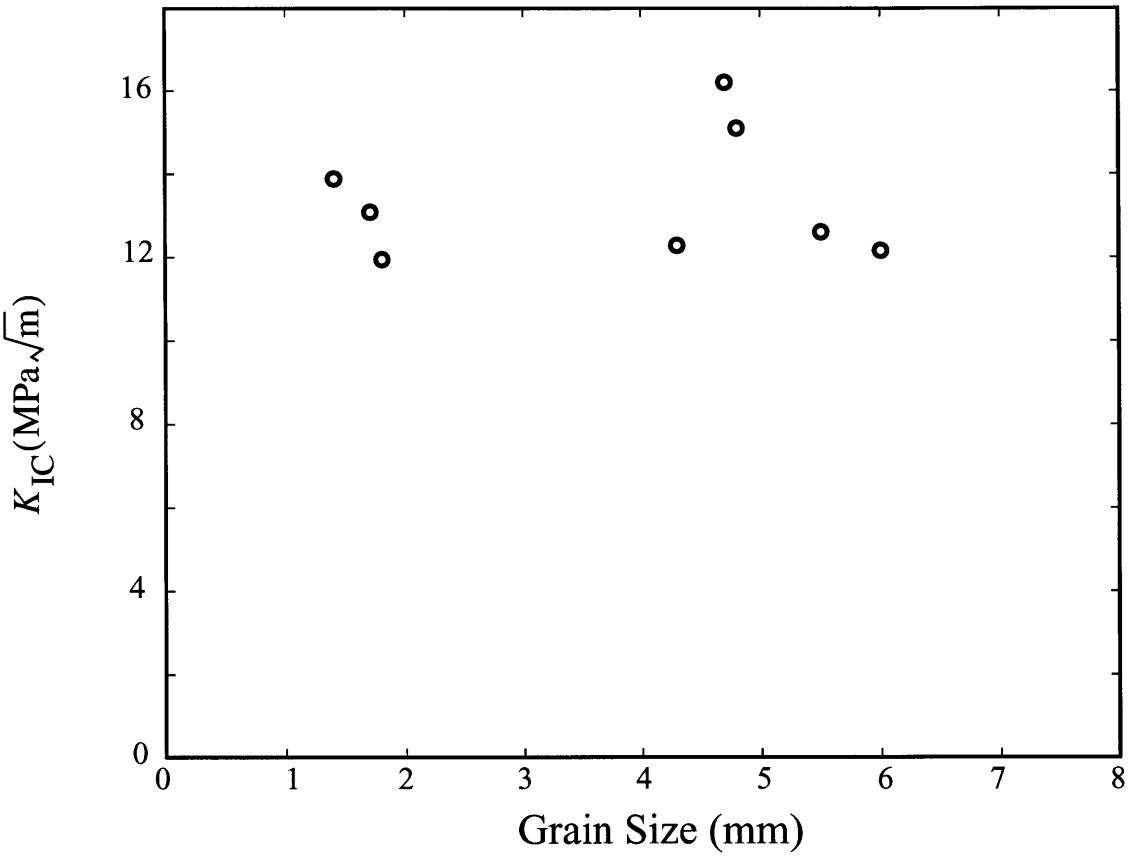

Fig.7-12 Grain size dependence of critical stress intensity of fracture at -20C in Fe-2%Si alloy.

7.6 General Observations

The role of grain boundaries and grain size effects in the plastic resistance of polycrystalline metals, particularly steel, has been well appreciated for many decades and has been modeled by Hall (1951) and Petch (1953) among others. Similarly, the effect of grain size on fracture and the beneficial consequence of grain refinement in increasing the brittle strength of steels is also well known (Petch, 1954). Furthermore, the triggering effects of fracturing grain boundary carbides in initiating brittle behavior in fracture transitions have also been studied to some extent (McMahon and Cohen, 1965; Ritchie, et al., 1973; Lin et al., 1986; Petch, 1986), as we had already noted in Chapter 1. Outside of these general considerations of grain size effects and phenomena related to triggering of brittle behavior in fracture transitions, specific considerations of the influence of grain boundaries on the cleavage cracking resistance have been few. Of these studies the most noteworthy have been those of Gell and Smith (1966), Anderson et al. (1994) and McClintock (1997). In the work of Anderson et al. (1994), the mode of cleavage fracture across hexagonal grains was considered in some detail to develop realistic cumulative probability distributions of fracture resistance in the context of "weakest link" models of such behavior. Gell and Smith (1966) have made one of the earliest observations on the cracking resistance of individual grain boundaries with known tilt and twist components, in hydrogen charged polycrystalline Fe-3%Si alloy and demonstrated that the major contribution to the cracking resistance of a grain boundary comes from its twist misorientation across the boundary rather than the tilt misorientation. This basic observation, also conjectured by McClintock (1997), was demonstrated directly by us in our earlier bi-crystal study (Chapters2, 5 and 6). The most detailed study of the cleavage cracking resistance of polycrystals, with which we will compare our findings is that of McClintock (1997), who has modeled the form of percolation of a cleavage cracking front across an array of randomly misoriented cubic grains. In his study McClintock makes a series of

assumptions that have actually been observed, in part, in the present experimental study. These included the following: that a) grains crack by a cleavage crack entering them from a neighboring grain rather than when the local resolved normal stress across the best available cleave plane reaches a critical value, b) a tilt misorientation across a boundary is far less of an obstacle for penetration of a boundary than a twist misorientation; c) normal expectations apply that cracking in re-entrant channels formed by cleaved adjacent grains do not readily extend while exposed corners on crack fronts are favored for cleavage propagation, and d) certain difficult-to-shear boundaries connecting facets of already cleaved grains (recalcitrant grain boundaries) effectively hold back the propagating cleavage front. While some conclusions of the McClintock model such as an excessive tendency of cracking fronts to advance parallel to the front by laterally propagating cleavage "kinks" along the front, was not found in our observations (the distribution of angles of grain boundary entrance is quite uniform from -90^{o} to 90^{o} with respect to the overall crack propagation direction), many other features were quite similar. The single major departure, however, between the predictions of McClintock and our model has been that the fracture toughness in his model exhibits a square-root type of grain size dependence (linear grain size dependence of work of fracture) while no such grain size dependence resulted from our model. This difference results primarily from McClintock's consideration that the cleavage work of fracture of grain interiors is negligible in comparison with the plastic bridging shear work along boundaries connecting primary cleavage facets, and that the latter process is indeed a plastic shearing-off process. In our model the cleavage work of grain interiors makes up fully one third of the overall fracture work and the bridging shear processes are viewed more as a *cleavage-like* shear fracture in which the traction drops abruptly to zero after a preparatory constant shear displacement emanating from the cleavage facets as

depicted partly in Fig.7-9 rather than a continuous linear drop characteristic of a pure plastic shearing-off process. Nevertheless, since there are significant uncertainties in both our model and that of McClintock, the exact nature of grain size dependence of the cleavage resistance remains unanswered. In any event it is clear that in the very large grain size limit there is no observable dependence which is in support of our model.

7.7 The decarburized 1010 steel

The experimental excursion into the behavior of the decarburized 1010 steel was made for the purpose of demonstrating that the findings on the Fe-2%Si alloy could be used in applications to low carbon steels. We note that our findings on the role of grain boundaries on the cleavage fracture resistance of the Fe-2%Si alloy are primarily of a geometrical nature exhibited by the strongly solid solution strengthened single-phase bcc material. Thus, the potential applicability of these findings to low carbon steel is appealing. In our experiments with the decarburized 1010 steel, where a potentially complicating pearlite component was removed, a full demonstration of a parallel behavior to the Fe-2%Si alloy was not quite possible because of the much-reduced level of plastic resistance of the former (shown in Fig.3-2) that resulted in all fracture measurements on the 1010 steel to be effectively on the upper shelf, even at the lowest test temperature of -150C. This was evident from the large distortions of the DECP specimens (see Fig. 7-13) at fracture and relegates the fracture work measurements of J_C to being of plane stress type. Nevertheless, much can be concluded from the cleavage fracture surface features shown in Figs.3-11a-11c, albeit all being in the nature of terminal cleavage occurring after very substantial amounts of expanded plastic work in the ligament between the two edge cracks. The fracture

surface of Fig.3-11a at -125C shows a field of cleaved grain facets of a distinctly brittle appearance with only weakly delineated river markings which we would have expected to be quite similar to those observable in the pure cleavage realm at the lower shelf below the ductile-to-brittle (DB) transition temperature. However, in the present case, because of the reduced level of the plastic resistance of the material due to decarburization, and on the basis of our estimation of the brittle strength of the 1010 steel, we expect that the BD transition will be in the liquid nitrogen temperature range. Nevertheless, the fracture appearance in Fig.3-11b at -70C, now well above the DB transition, still shows a field of cleaved grains, but with well-delineated cleavage river markings, giving clear evidence of accompanying plastic distortions resulting from the bridging deformations between grains.

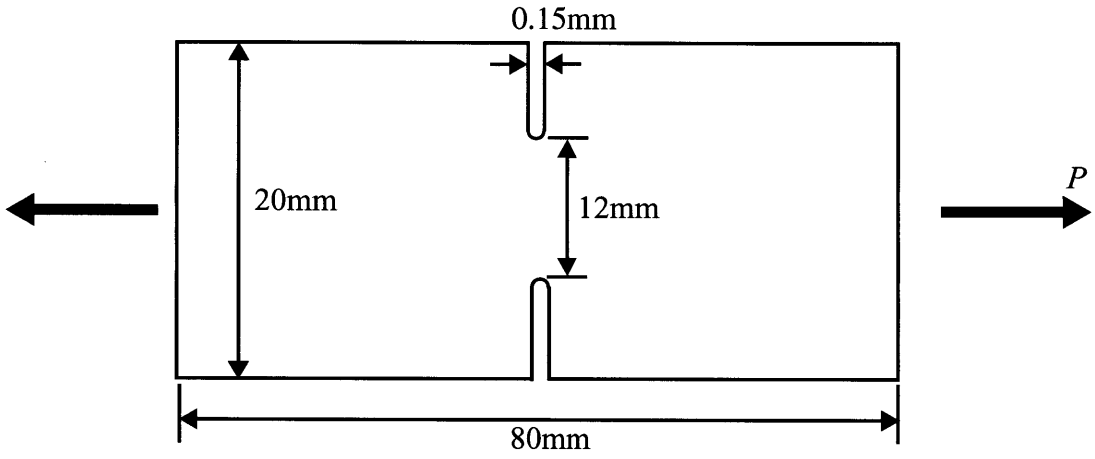

Fig. 7-13 A schematic diagram of a DECP specimen of decarburized 1010 steel. The specimen thickness is about 4mm.

The most profound observation derivable from the comparison of the behavior of the Fe-2%Si alloy and the decarburized 1010 steel is the dramatic reduction in the conventional ductile to brittle transition temperature by about 400C, from 250C (for the Fe-2%Si) to -150C (for the decarburized 1010 steel) when all hardening agents are removed from the Fe. We note that this

effect is far larger than what might be expected from inspection of Fig.3-2 and the shift of the temperature dependent plastic resistance curves. This further accentuation of the difference between the DB transitions results from the fact that the J_C measurements for the 1010 steel are of a plane stress type in the DECP specimen of quite inadequate size and shape while the results for the Fe-2%Si alloy were derived from *bona-fide* plane strain test configurations.

7.8. Conclusions

In the lower shelf in Fe-2%Si and in low carbon steels cleavage cracks percolate through grains by selectively going through the most exposed grain boundaries with the lowest penetration resistance and subjected to the largest local crack driving forces. While these grain boundaries govern the overall chronology of cleavage crack percolation they contribute little to the overall fracture resistance.

The overall fracture resistance is derived roughly in one part by the cleavage resistance of individual misoriented cleavage facets in grains and in two parts by the work of fracture along nearly vertical boundaries bridging the primary cleavage facets of adjoining grains by a combination of plastic shear and a "cleavage-like" shear separation.

Both experiments and modeling of crack percolation mechanisms suggest that the overall cleavage fracture resistance due to the tesselation of the cleavage fracture process by the grain boundaries is largely grain size independent, but increases the fracture resistance (G_{ICPC}) in comparison with a flat untesselated cleavage process (G_{ICSC}) by a factor of close to 3.0.

CHAPTER 8

DISCUSSION AND SUMMARY

Through the experiments and the models introduced in previous chapters, the role of grain boundaries in cleavage cracking in low-carbon Fe-Si alloy and decarburized 1010 steel was studied. The crack-arrest experiment in bi-crystal Fe-3%Si alloy specimens shed light on deeper understanding of fracture resistance of individual high-angle grain boundaries, and has led to quantitative models to predict the influence of crystal misorientation.

According to the observations of the penetration modes of a cleavage crack across a grain boundary, when the fracture resistance of the grain boundary was overcome, the crack front broke through the grain boundary simultaneously or near-simultaneously at a number of break-through points. The distance between break-through points was in the range from less than 1 micron to around 50 microns, and followed a lognormal distribution. SEM fractographs showed radiating cleavage markings around each break-through point, indicating that, after the crack shifted its fracture surface from (100) plane of grain *A* to that of grain *B*, the crack front bowed into grain *B* deeper and deeper stably with the increasing of overall crack-tip stress intensity. The final break-through occurred when the crack front started to propagate unstably associated with the shear separation of grain boundary islands between break-through points that had bridged the two fracture surfaces together. During this process, additional fracture work was required to produce primary and secondary fracture facets in grain *B*, as well as to shear apart grain boundary pieces. Experimental data showed that the influence of twist misorientation was larger than that of tilt misorientation.

It was observed through our experiments that the fracture resistance to cleavage cracking of single crystal of our material was higher than surface free energy by almost an order of magnitude. Since the experiments were performed at temperatures more than 200 degrees lower than the brittle-to-ductile transition temperature, under which the activity of dislocation at crack tip should be very limited, this very high value of K_{ICA} could not be explained well by conventional plastic zone theory describing upper-shelf behavior of the material, in which the crack propagates by cleavage after extended development of crack-tip plastic zone associated with large amount of energy dissipation resulting in a fracture work much larger than the surface free energy.

Through SEM, it was observed that there existed evidence of plastic shearing and bending of isolated ligaments dispersed across the whole fracture surface in grain *A*. Based on this observation, a process-zone model was developed to explain the difference between measured K_{ICA} and the value estimated based on surface free energy. Throughout the whole propagation process of the crack across grain *A*, there existed a process zone ahead of crack tip where undercuttings and cleavage fracture propagating at different height produced many separated ligaments. To finish the final separation of the two fracture surfaces, between ligaments had to be sheared apart, during which elastic/plastic bending and ductile shear fracture dissipated a certain amount of fracture work, resulting in the relatively high value of measured K_{ICA}. Compared with the conventional plastic zone model, the important difference of the process zone model is that most of fracture work is dissipated *after* the crack starts to propagate. Another difference is that, in the process zone model, there is no need for the assumption of large extent of dislocation activity ahead of crack tip, which is a characteristic behavior of fracture at temperature higher than BDTT, there-

fore this model can be applied to explain the relatively high values of K_{ICA} measured in our low-temperature experiments.

Further analysis of measured fracture resistance of bi-crystal grain boundaries at different temperatures revealed a fracture work transition around 0C. This fracture work transition was very different from the conventional brittle-to-ductile transition in the sense of both transition temperature and extent of transition. The conventional BDTT of Fe-2%Si alloy used in our experiments was observed to be about 250C. The fracture work measured at this very low transition temperature was only 20%-30% higher than that below this transition temperature, while in the conventional BDT, the change of fracture work could be several times of the lower-shelf value. Below this transition temperature, not much evidence of plastic behavior could be observed at the fracture surface through SEM. The fracture was in a pure cleavage mode. Above this transition temperature, although most of the fracture surface was still made up of well formed cleavage facets, and that was no difference in appearance from pure cleavage if examined by naked eyes, through SEM, plastic bending of strips in grain *B* and ductile dimples on many separated grain boundary pieces could be observed. The fracture was actually in a mixed-cleavage mode. Therefore, this transition was identified as a pure cleavage to mixed cleavage (PC/MC) transition. The mechanism of energy dissipation was quite similar to that in the process zone model introduced above, except that, here, the plastic deformation occurred at the bi-crystal grain boundary and strips close to it. The amount of dissipated energy associated with the plastic behavior, which was negligible below the PC/MC transition temperature became significant the above PC/MC transition temperature, resulting in the fracture work transition. The reason that PC/MC transition temperature was much lower than BD transition temperature could be that, to separate grain boundary pieces and strips,

the separation usually occurred along planes almost vertical to the primary fracture surface. The difficulty to develop this mixture of mode-II and mode-III cleavage fracture greatly lowered the fracture work transition temperature.

To apply our findings for fracture behavior of individual grain boundary to polycrystalline materials, we performed fracture experiments in both coarse-grained polycrystalline Fe-2%Si specimens and fine-grained decarburized 1010 steel specimens. In the fracture experiments in Fe-2%Si specimens, due to the large grain size, it was possible to track in great detail the penetration process of the crack front across each grain boundary in the whole sample. It was found that not every grain boundary would be penetrated through when the crack front encountered it. Only those grain boundaries with low fracture resistance and high local stress intensity would be broken through. Other grain boundaries would serve as pieces of reinforcement and had to be sheared apart later. A computer simulation confirmed this findings by reproducing quite well the percolation map of one of specimens studied in our experiments, at least at the beginning where the basic assumption under only model I driving force and quasi-static conditions were applicable.

Based on this observation, a simple model was developed to predict the fracture resistance of polycrystalline materials to cleavage cracking. The total fracture resistance contains three parts, taking account for the fracture work W_1 required to produce cleavage facets in grains, the fracture work W_2 required to break through those "weak" grain boundaries, and the fracture work W_3 required to shear apart the remaining grain boundaries, respectively. Interestingly, the contribution of the second term W_2 was calculated to be negligible for the very large grain size range. The con-

tribution of W_1 was about one third of the total fracture work, while W_3 was about two thirds of the total fracture work.

According to this model, when the grain size is very small or very large, the grain-size dependence of fracture resistance of polycrystalline materials should vanish, and this was verified by fracture experiments on Fe-2%Si specimens with different grain sizes distributing in a narrow range. All these discussions were found to be relevant for fine-grained decarburized 1010 steel, which means that these conclusions drawn from coarse-grained fracture experiments can be applied to general low-carbon steels.

An interesting finding in this thesis is that, unlike what was assumed by some researchers before, the break-through process of a cleavage crack across a high-angle grain boundary does not involve crack stoppage in grain *A* and reinitiation of cleavage in grain *B*. The crack front can topologically quite easily penetrate through the grain boundary at break-through points and bow into grain *B*, leaving cleavage radiation markings behind at each entry point. The role of a grain boundary is more like a row of reinforcement particles which first arrested the crack front by crack-trapping, then bridges the two fracture surfaces behind the probing curved crack front. Like the distribution of the density of reinforcement particles, the spacing between neighbor break-through points, *w*, is very essential in determining the fracture resistance of the grain boundary. However, the mechanism of formation of the break-through point is still unclear; therefore the factors influencing *w* are still unknown. Through experimental measurement, *w* followed a log-normal distribution quite well. Its value varied in the range from less than one micron to about 50 microns, and the peak was around 2-3 microns. This observation raised an interesting question of

what would happen if the grain size is smaller than 1-2 microns. To answer this it is necessary to understand the mechanisms of the formation of break-through windows first, which is also related to the question about factors dominating *w*. Because the grain boundary studied in our experiments was free from carbides or other inclusions, it is very likely that the answer to these questions lie in lattice structure of the grain boundary and its interaction with a sharp crack tip.

In the experiments in polycrystalline materials, we observed three kinds of behavior of grain boundaries. The first two types are grain boundaries encountered by the propagating crack front. If the local fracture resistance of the grain boundary is low and/or the local stress intensity is large, the grain boundary tends to be penetrated through, otherwise the grain boundary will trap the part of crack front contacting it and be sheared apart later as isolated bridging pieces, when the rest of crack front penetrates through neighboring grains and goes a round-about way to leave this recalcitrant grain boundary behind. The third type of grain boundaries are neighbors of grain boundaries encountered by the crack front, but do not lie in the crack front. These grain boundaries separate neighboring grains apart along the crack front, and serve as "fire breaks" by interrupting break-through process from one grain to another, making the break-through process in each grain independent. Sooner or later, with the growth of the crack, these grain boundaries will be encountered by the propagating crack front directly and its behavior will be described by either of the first two types.

In addition to the study on grain boundary behavior, thermal crack arrest experiments were performed in Fe-3%Si single crystal specimens to study the brittle-to-ductile transition. The crack propagated through a temperature gradient, and when the crack front advanced to the position

where the temperature was high enough such that brittle-to-ductile transition occurred, the crack would be thermally arrested. This brittle-to-ductile transition was purely caused by thermal process of dislocations production at crack tip. Berg-Barrett x-ray images were taken to verify our expectation for the activated slip systems that caused the BD transition but the results were inconclusive.

Appendix A

DEFINITION OF RELEVANT MISORIENTATION ANGLES

The crystallographic reference axes should be those of grain *A* as shown in Fig. 2-2. By design of the experiment, axis **k** is parallel to the DCB load axis *P* and axis **j** is parallel to the wedge insertions axis, **x**. For the purpose of assessing the grain boundary resistance we consider a grain boundary that is nearly normal to the **x** axis, but actually its line of intersection with the cleavage plane of grain *A* makes an angle β with respect to the axis **i**. The boundary may also make an angle α relative to the axis **k**. For the purpose of the cleavage crack traversing from grain *A* to grain *B* the angle α is of much less importance. The crack growth resistance across the real boundary, making angles α and β should be almost indistinguishable from a reference plane perpendicular to the (001) plane that makes an angle β relative to axes **i** or **j**, i.e. a rotation about axis **k**. The tilt and twist angles ψ and φ of grain *B* should then be defined in relation to this virtual reference plane perpendicular to the (001) plane.

Grain *B* is misoriented relative to grain *A*. Its crystallographic axis **i'**, **j'**, and **k'** are defined by a set of direction cosines relative to the **i**, **j**, **k** axes of grain *A*. We make no distinction regarding the crack growth resistance in a cleavage plan, and treat the principal cleavage plane of grain *B* simply by its unit normal vector $\mathbf{n_B}$. We define the principal cleavage plane of grain *B* to be the one for which the unit normal vector $\mathbf{n_B}$ makes the smallest angle relative to the axis **k** of grain *A*. Therefore, $\mathbf{n_B}$ is parallel to axis **k'** of grain *B*. Thus,

$$\mathbf{n_B} = n_{B1}\mathbf{i} + n_{B2}\mathbf{j} + n_{B3}\mathbf{k}, \tag{A-1}$$

referred to the principal axis of grain *A*. However, since $\mathbf{n_B}$ is parallel to **k'**

$$\begin{aligned} n_{B1} &= \alpha_{31} \\ n_{B2} &= \alpha_{32} \\ n_{B3} &= \alpha_{33} \end{aligned} \tag{A-2}$$

where α_{31}, α_{32}, and α_{33} are the direction cosines of axis **k'** relative to the axis of grain *A*. Consider now the virtual grain boundary plane, the line of intersection of which makes an angle

β relative to axis **i**. The plane is defined by a unit normal vector **b** which is given vectorially as:

$$\mathbf{b} = b_1\mathbf{i} + b_2\mathbf{j} \text{ (with } b_3 = 0) \tag{A-3}$$

where $b_2 = \cos\beta$, $b_1 = \sin\beta$. (A-4)

in reality if the inclination α is also considered, then $b_3 = \cos\alpha$ where α is the angle of rotation about the line of intersection of the virtual plane with the (001) plane, in the direction of axis **k'**. We ignore this inclination for defining the principal tilt and twist angles of grain *B* relative to the plane of the virtual boundary.

Then, the principal tilt angles ψ and twist angle φ redefined as follows.

$$\psi = \frac{\pi}{2} - \text{acos}(\mathbf{n_B}\ \mathbf{b}) \tag{A-5}$$

$$\varphi = \frac{\pi}{2} - \text{acos}(\mathbf{n_B}\ \mathbf{d}) \tag{A-6}$$

where **d** is the vector in the cleavage plane of grain *A* making an angle β with the **i** axis.

Then finally,

$$\psi = \frac{\pi}{2} - \text{acos}(\alpha_{31}\sin\beta + \alpha_{32}\cos\beta) \tag{A-7}$$

$$\varphi = \frac{\pi}{2} - \text{acos}(\alpha_{31}\cos\beta - \alpha_{32}\sin\beta) \tag{A-8}$$

if the boundary were perpendicular to axis **j** i.e., $\beta = 0$,

$$\psi = \frac{\pi}{2} - \text{acos}(\alpha_{32}) \tag{A-7a}$$

$$\varphi = \frac{\pi}{2} - \text{acos}(\alpha_{31}) \tag{A-8a}$$

REFERENCES

Alexander, H., (1986), in "Dislocation in Solids", edited by Nabarro, F. R. N., Elsevier, Amsterdam, vol.7, p.115.

Alexander, H. and Haasen, P., (1968), in "Solid State Physics", edited by Seitz, F. and Turnbull, D., Academic Press, NY, vol.22, p.28.

Anderson, T. L., Stienstra, D., Dodds, Jr., R. H., (1994), in "Fracture Mechanics: Twenty-fourth Volume", edited by Landes, J. D., McCabe, D. E. and Boulet, J. A. M., ASTM STP-1207, ASTM: Philadelphia, PA. p.186.

Andersson, H. and Bergkvist, H., (1970), *J. Mech. Phys. Solids*, **18**, 1.

Argon, A.S., (1987), *Acta Metall*, **35**, 185.

Argon, A. S., (2000), in "Comprehensive Composite Materials", edited by Kelly, A. and Zweben, C., vol. 1 (edited by Chou, T.-W.), Pergamon/Elsevier, Amsterdam, p.763.

Argon, A. S. and Gally, B. J., (2001), *Scripta Mater.*, **45**, 1287.

Argon, A. S. and Qiao, Y., (2002), *Phil. Mag.*, to be published.

Armstrong, R. W., (1966), *Mater. Sci. Eng.*, **1**, 251.

ASTM Symposium, (1994), "Fracture Mechanics: Twenty-fourth Volume", edited by Landes, J. D., McCabe, D. E., and Boulet, J. A. M., ASTM, Philadelphia, PA.

Benthem, J. P., (1977), *Int. J. Sol. Struct.*, **13**, 479.

Benthem, J. P., (1980), *Int. J. Sol. Struct.*, **16**, 119.

Birks, N., (1969), "Decarburization", The Iron and Steel Inst., London.

Bowen, P., Druce S.G., and Knott, J.F., (1987), *Acta Metall*, **35**, 1735-1746.

Brown, S. B., Kim, K. H., and Anand, K., (1989), *Internat. J. Plasticity*, **5**, 95.

Bower, A. F. and Ortiz, M., (1991), *J. Mech. Phys. Solids*, **39**, 815.

Brede, M. and Haasen, P., (1988), *Acta Metall.*, **36**, 2003.

Brede, M., Hsia, K. J., and Argon, A. S., (1991), *J. Appl. Phys.*, **70**, 661.

Bulatov, V. V., Yip, S., and Argon, A. S., (1995), *Phil. Mag.*, **72**, 452.

Chaudhari, P., and Matthew, J. W., (1972), *Grain boundaries and interfaces*, North Holland, Amsterdam.

Cheung, K.S. and Yip, S., (1991), *Phys. Rev. Lett.*, **65**, 2804.

Chiao, Y.-H. and Clarke, D. R., (1989), *Acta Metall.*, **47**, 203.

Crocker, A., Smith, G., Flewitt, P. and Moskovic, R., (1996), in "Proceedings of the 11th European Conference on Fracture (ECF11)", Eng. Mater. Advis. Serv., Warley, UK, vol.1, p.233.

Dahlquist, G. and Bjorck, A., *Numerical Methods*, Englewood Cliffs, NJ, Prentice-Hall, 1974.

Erickson, J. S., (1962), *J. Appl. Phys.*, **31**, 362.

Gally, B. J., (1999), *Experimental investigation of the brittle to ductile transition in fracture of single crystal silicon*, Ph.D. Thesis, Dept. of Mater. Sci. Eng., M.I.T., Cambridge, MA.

Gally, B. J. and Argon, A. S., (2001), *Phil. Mag.*, **81**, 699.

Gell, M. and Smith, E., (1967), *Acta Metall.*, **15**, 253.

Gemperlova, M., Polcarova, J., and Bradler, J., (1991), *J. Appl. Cryst.*, **24**, 331.

George, A., and Michot, G., (1993), in "International series on the strength and fracture of materials and structures 2", Pregamon Press, NY, USA, p.1187-1192.

Gilman, J. J., (1960), *J. Appl. Phys.*, **31**, 2208.

Hahn, G. T., Averbach, B. L., Owen, W. S. and Cohen, M., (1959), in "Fracture", edited by Averbach, B. L., Felbeck, D. K., Hahn, G. T. and Thomas, D. A., MIT Press, Cambridge, MA, p.91.

Hall, E. O., (1951), *Proc. Phys. Soc.*, **B64**, 747.

Hirsch, P. B., Roberts, S. G., and Samuels, J., (1988), *Rev. Phys. Appl.*, **23**, 409.

Hirsch, P. B., Roberts, S. G., Samuels, J., and Warren, P. D., (1989), in "Advances in Fracture Research", edited by Salama, K., et al, Pergamon Press, Oxford, vol.1, p.139.

Hirsch, P. B. and Roberts, S. G., (1997), in "Cleavage Fracture: Geoge R. Irwin Symposium", edited by Chan, K. S., TMS, Warrendale, PA, p.137.

Hoenig, A., (1982), *Eng. Fract. Mech.*, **16**, 393.

Hondros, E. D. and Stuart, L. E., (1967), *Phil. Mag.*, **17**, 711.

Hsia, K. J. and Argon, A. S., (1991), *Mech. Mater.*, **11**, 19.

Hsia, K. J. and Argon, A. S., (1994), *Mater. Sci. Eng.*, **A176**, 111.

Hull, D., (1960), *Acta Metall.*, **8**, 11.

Hull, D., (1997), in "Cleavage Fracture: George R. Irwin Symposium Proceedings", edited by Chan, K. S., TMS: Warrendale, PA, p.59.

Irwin, G. R., (1948), in "Fracturing of Metals", ASM, Cleveland, OH, p.147.

Kanninen, M. F., (1973), *Intern. J. Fracture*, **9**, 83.

Kelly, A., Tyson, W.R., and Cottrell, A.H., (1967), *Phil. Mag.*, **15**, 567.

Khanta, M., Pope, D. P., and Vitek, V., (1994a), *Phys. Rev. Letters*, **73**, 684.

Khanta, M., Pope, D. P., and Vitek, V., (1994b), *Scripta Metall. Mater., 31*, 1349.

Knott, J. F. (1997), in "Cleavage Fracture: George R. Irwin Symposium Proceedings", edited by Chan, K. S., TMS, Warrendale, PA, p.171.

Knott, J. F. and Cottrell, A. H., (1963), *J. Iron Steel Inst.*, **201**, 249.

Kumar, V., German, M. D. and Shih, C. F., (1981), *EPRI Report NP-1931*, Palo Alto, CA, Electric Power Research Institute.

Lin, T., Evans, A. G., and Ritchie, R. O., (1986), *J. Mech. Phys. Solids*, **34**, 477.

Low, J.R., (1963), in "Fracture of Solids", edited by Crucker, D.C. and Gilman J.J., Interscience, New York, p.197.

Mahajan, S. and Williams, D. F., (1973), *Int. Met. Rev.*, **18**, 43.

McClintock, F. A. and Argon, A. S., (1966), *Mechanical behavior of materials*, Addison Wesley, Reading, MA.

McMahon, C. L. and Cohen, M. (1965), *Acta Metall.*, **13**, 591.

McClintock. F. A., (1997), in "Cleavage Fracture: George R. Irwin Symposium Proceedings", edited by Chan, K. S., TMS: Warrendale, PA, p.81.

McClintock, F.A. and Irwin, G.R., (1965), in "Symposium fracture toughness testing and its application", Special Technical Publication No.S81, American Society of Testing and Materials, p.84-113.

McClintock, F. A. and Clerico, M., (1980), *J. Mech. Phys. Solids*, **28**, 1.

Moon, D. W. and Vreeland, T., (1968), *J. Appl. Phys.*, **39**, 1766.

Mower, T. M. and Argon, A. S., (1995), *Mechanics of Materials*, **19**, 343.

Murr, L. E., (1975), *Interfacial phenomena in metals and alloys*, Addison Wesley, Reading, MA.

Nakamura, I. and Parks, D. M., (1989), *Int. J. Sol. Struct.*, **25**, 1411.

Newkirk, J. B., (1959), *Tran. Met. Soc. AIME*, **215**, 483.

Orowan, E., (1949), in "Reports on progress in physics", vol.12, p.185.

Ortiz, M., (1996), *Comput. Mech.*, **18**, 321.

Owen, W. S. and Hull, D., (1963), in "Refractory metals and alloys II", edited by Semchyshen, M. and Perlmutter, L., Interscience, NY.

Parker, E. R., (1957), *Brittle behavior of engineering structures*, J. Wiley & Sons, NY.

Petch, N. J., (1953), *J. Iron Steel Inst.*, **174**, 25.

Petch, N. J., (1954), in "Progress in Metal Physics", edited by Chalmers, B. and King, R., Pergamon Press, London, vol.5, p.1.

Petch, N. J., (1986), *Acta Metall.*, **34**, 1387.

Qiao, Y. and Argon, A. S., (2002), *Mech. Mater.*, in the press.

Rice, J. R., (1985), *J. Appl. Mechanics*, **52**, 571.

Rice, J. R., (1992), *J. Mech. Phys. Solids*, **40**, 235.

Rice, J. R. and Beltz, G. E., (1994), *J. Mech. Phys. Solids*, **42**, 333.

Rice, J.R., Beltz, G.E., and Sun, Y., (1992), in "Topics in Fracture and Fatigue", edited by Argon, A. S., Springer, NY, p.1-58.

Rice, J.R., and Thomson R., (1974), *Phil. Mag.*, **29**, 73-97.

Riedel, H. and Rice, J. R., (1980), in "Fracture mechanics: Twelfth conference", edited by Paris, P. C., ASTM-STP 700, ASTM, Philadelphia, PA, p.112.

Ritchie, R. O., Knott, J. F. and Rice, J. R., (1973), *J. Mech. Phys. Solids*, **21**, 395.

Rosenfield, A. R. and Shetty, D. K., (1983), *Eng. Fract. Mech.*, **17**, 461.

Saka, H. and Imura, T., (1972), *J. Phys. Soc. Japan*, **32**, 702.

Saka, H. and Imura, T., (1973), *Phys. Stat. Sol.*, **A19**, 653.

Schock, G., and Puschl, W., (1991), *Phil. Mag.*, **A64**, 931-949.

Schwartz, D., Bristowe, P. D., and Vitek, V., (1987), *Acta Metall.*, **36**, 675.

Shank, M. E., (1954), *A critical survey of brittle fracture in carbon plate steel structures other than ships*, Welding Res. Council Bulletion Series, No.17, Welding Soc., NY.

Smith, E., (1966), *Acta Metall.*, **14**, 985.

St John, C., (1975), *Phil. Mag.*, **32**, 1193.

Stein, D. F. and Low, J. R., (1960), *J. Appl. Phys.*, **31**, 362.

Stroh, A.N., (1954), *Proc. Roy. Soc.*, **A223**, 404.

Stroh, A. N. (1955), *Proc. Roy. Soc.*, **A232**, 548.

Thelning, K. E., (1984), *Steel and Its Heat Treatment*, Butterworth, London.

Turner, A. P. L., Vreeland, T. and Pope, D. P., (1968), *Acta Cryst.*, **A24**, 452.

Tweed, J. H. and Knott, J. F., (1987), *Acta Metall. Mater.*, **35**, 1401.

Xia, L. and Shih. C. F., (1996), *J. Mech. Phys. Solids*, **44**, 603.

Xu, G. and Ortiz, M., (1993), *Int. J. Numer. Methods Eng.*, **36**, 3675.

Xu, G., (1994), *Three dimensional elastic analysis of crack growth and toughening mechanism of brittle matrix composites*, Ph.D. Thesis, Division of Eng., Brown Univ., Providence, RI.

Xu, G., Argon, A. S., and Ortiz, M., (1995), *Phil. Mag.*, **72**, 415.

Xu, G., Argon, A. S., and Ortiz, M., (1997), *Phil. Mag.*, **75**, 341.

Zener, C. (1979), in "Fracturing of Metals", ASM, Metals Park, OH, p.3.

Zhou, S. J. and Thomson, R., (1991), *J. Mater. Res.*, **6**, 639.

Zikry, M.A. and Kao, M., (1994), *Comput. Mater. Model.*, **294**, 71.